Thesis

Nonequilibrium phenomena and dynamical controls in strongly correlated quantum systems driven by AC and DC electric fields

Kazuaki Takasan

Department of Physics, Kyoto University

January, 2019

Abstract

In recent years, various interesting nonequilibrium phenomena are observed in solids and gathering great attention. For example, it has been reported that applying strong laser fields induces transient superconductivity above the equilibrium critical temperature [1]. Topological states of matter can also be changed with laser light. This has been theoretically proposed [2] and already experimentally observed [3–5]. It has been revealed that not only the laser light (AC field), but also the DC-field induces quite interesting phenomena recently. For instance, it has been reported that DC electric field induces a finite current in Mott insulators, giving rise to very strong diamagnetism in the nonequilibrium steady states [6]. Furthermore, based on the study of these nonequilibrium phenomena, the possibility of controlling states of matter with nonequilibrium phenomena has also been investigated. It is expected that some important controls which are impossible or difficult in equilibrium become available in nonequilibrium. In fact, a control using periodic driving with external fields is called "Floquet engineering" and this has been established as one of the useful experimental techniques to realize desired quantum states in the field of cold atomic systems [7]. As shown above, nonequilibrium phenomena and controls with them in condensed matter systems are forming a rapidly growing research field in recent years.

On the other hand, theoretical understanding of these nonequilibrium phenomena still has been a challenging problem. In particular, nonequilibrium phenomena in strongly correlated systems are difficult to treat theoretically and proposing nonequilibrium control in strongly correlated systems is more tough problem because we have to treat the effect of interaction and nonequilibrium dynamics at the same time. However, various interesting and exotic phases of matter (e.g. unconventional superconductivity and quantum spin liquid) mostly appear in strongly correlated materials and thus it is an important task to investigate strongly correlated systems.

Motivated by this situation, we have studied the nonequilibrium phenomena in strongly correlated systems and proposed possible schemes to control the states of matter using nonequilibrium phenomena. In this thesis, we present our recent studies in this direction. Brief summaries of these studies are shown below.

1. *Laser-induced topological superconductivity in d-wave superconductors* (Chap. 2)

   Topological superconductivity (TSC) has attracted much attention because it can host Majorana fermions that are expected to be applied to quantum computation. However, the experimental realization of TSC have been very limited and highly desired. In this study, we proposed a possible scheme to realize TSC in laser-irradiated d-wave superconductors such as cuprate superconductors. Our calculation based on Floquet theory revealed that the laser-induced effective Zeeman-field plays an important role in realizing TSC.

2. *Control of quantum phases in heavy fermion systems with laser light* (Chap. 3)

   In heavy fermion systems, interplay between Kondo effect and RKKY interaction plays an important role and realizes various quantum phase transitions. In this study, we investigated how this interplay is affected by the application of laser fields and how we can control the quantum phase transitions. We found that either enhancement or suppression of Kondo effect occurs depending on crystalline structures and systematically studied the effect on the phases of matter including topological phases (e.g. topological Kondo insulators).

3. *Control of insulating magnets with DC electric fields or terahertz laser fields* (Chap. 4)

   In this study, we considered the application of DC electric fields or slow AC fields (such as terahertz fields) to insulating magnets and investigated how the exchange interaction is modified with electric fields. We found that the coupling in the direction of electric fields is enhanced and this is very useful to control the anisotropy of magnetic interactions. Based on this idea, we proposed exotic phases of matter induced by electric fields, e.g. electric-field-induced quantum spin liquids and electric-field-induced topological phases.

Contents

List of publications

Papers related to the thesis

1. Kazuaki Takasan, Akito Daido, Norio Kawakami and Youichi Yanase
   Laser-induced topological superconductivity in cuprate thin films
   Physical Review B **95**, 134508 (2017)

2. Kazuaki Takasan, Masaya Nakagawa and Norio Kawakami
   Laser-irradiated Kondo insulators: Controlling the Kondo effect and topological phases
   Physical Review B **96**, 115120 (2017)

3. Kazuaki Takasan, Masaya Nakagawa and Norio Kawakami
   Laser-induced phase transitions of topological Kondo insulators
   Physics Procedia **75**, 447-454 (2015)

4. Kazuaki Takasan and Masahiro Sato
   Control of Magnetic and Topological Orders with a DC Electric Field
   arXiv:1802.04311 (submitted)

Papers not includied in the thesis

1. Kaoru Mizuta, Kazuaki Takasan, Masaya Nakagawa and Norio Kawakami
   Spatial-Translation-Induced Discrete Time Crystals
   Physical Review Letters **121**, 093001 (2018)

2. Zongping Gong, Yuto Ashida, Kohei Kawabata, Kazuaki Takasan, Sho Higashikawa and Masahito Ueda
   Topological phases of non-Hermitian systems
   Physical Review X **8**, 031079 (2018)

Chapter 1

Introduction

In this thesis, we present our theoretical results related to nonequilibrium phenomena and dynamical controls in strongly correlated systems under AC and DC electric fields. Before going into the detail, we first explain the meaning of "nonequilibrium phenomena" and "dynamical controls" in this thesis. In other words, we clarify the phenomena which we are interested in. For this purpose, we explain what we call nonequilibrium phenomena in condensed matter systems and give some typical examples of them in Sec. 1.1, and then explain the idea and the examples of dynamical controls using electric fields in Sec. 1.2. In these sections, we mention the recent experiments closely related to our studies. In contrast, we focus on the theoretical aspect in Sec. 1.3. We explain the recent developments of theoretical tools for studying the nonequilibrium phenomena. After that, we explain our motivation of studies in this thesis in Sec. 1.4. Finally, we give an overview of this thesis in Sec. 1.5.

1.1 Nonequilibrium phenomena in condensed matter physics

In the last decades, condensed matter theory has been developed mainly based on quantum mechanics [1] and statistical mechanics [2]. To understand phenomena emerging in solids, most theorists have constructed microscopic models and analyzed it. However, it is difficult to directly solve the models since it includes so many degrees of freedom. To overcome this point, theorists have applied the techniques established in statistical mechanics to their models, and then obtained the results which are able to be compared with experiments. To obtain the thermodynamic properties, this works well, but we need the information out of equilibrium to know the transport or optical properties. Fortunately, linear response theory, which enables us to understand nonequilibrium phenomena occurring near equilibrium states from the information of *fluctuation* already existing in equilibrium, was established by R. Kubo more than sixty years ago [8] and has been applied to a wide range of systems successfully.

Based on this strategy, condensed matter physics has provided many results explaining various macroscopic behaviors of solids and established the position as a fundamental theory for modern engineering and technologies. For example, band theory based on Bloch's theorem [9] succeeded in explaining the physics of semiconductors and then engineering of semiconductors is one of the most important fundamental technologies supporting the devices which we are using

[1] Strictly speaking, condensed matter physics includes the research subjects where quantum mechanics is not so important (e.g. soft condensed matter), but in this thesis we focus on solid state physics where the quantum mechanical description plays an important role.

[2] We remark that classical physics (e.g. classical mechanics, electromagnetism, and thermodynamics) has played an important role in condensed matter physics.

in the daily life (e.g. electronics). The other example is a high temperature superconductivity. This was discovered almost thirty years ago by G. Bednorz and K. A. Müller [10]. At that time, the reason why the critical temperature is so high is unclear, but the rapid developments of many-body theories in condensed matter physics have resolved the many problems and clarified the most part of its mechanism. Based on this development, high-temperature superconductors have many different applications nowadays, ranging from levitating trains to ultra-efficient power lines.

However, phenomena which cannot be explained within the conventional theoretical tools have been reported and gathering great attention in recent years. Here, we mean the conventional tools as quantum mechanics, statistical mechanics, and linear response theory. We call the phenomena that cannot be explained by them "nonequilibrium phenomena" in this thesis. Especially, we consider nonequilibrium phenomena which happen under laser light (AC electric fields [3]) or DC electric fields in this thesis. Electric fields couple to the electrons in solids and strong fields can drive their motion and make the system go out of equilibrium states. We remark that we are not mainly interested in the states of matter driven by weak electric fields which can be captured only with the linear response theory. The interesting point of the nonequilibrium phenomena is that applying electric fields can change quantum states of matter and then it induces various phenomena and realizes diverse phases of matter uniquely existing out of equilibrium. The scope of nonequilibrium phenomena widely spreads in the research areas of modern condensed matter physics, e.g. superconductivity, magnetism, transport phenomena and topological phenomena. The phenomena that cannot happen in equilibrium can occur out of equilibrium. For example, nontrivial states which are unstable in equilibrium can be meta-stable out of equilibrium. Therefore, the research field of nonequilibrium phenomena can be regarded as a frontier for exploring new phenomena and exotic phases of matter that cannot be realized in equilibrium.

We want to emphasize that the on-going growth of this research field is supported by recent developments of experimental technologies. In other words, the studies of the nonequilibrium phenomena had to wait for these developments. Thus, we think that this kind of studies are just beginning and there are plenty of room to investigate. In this paragraph, we briefly explain the developments of experimental techniques. From the experimental point of view, we need very strong electric fields to induce nonequilibrium phenomena because weak electric fields just give very weak perturbation to the states of matter and only work as a probe for states of matter. Fortunately, the technologies of laser light sources are rapidly developed and sufficiently strong laser fields are going to be realized. For example, 1-10 MV/cm electric fields are already realized in many laboratories. In addition, most of nonequilibrium phenomena appear in an ultrafast time scale, such as femtosecond (fs) or picosecond (ps) order, and then we need sophisticated time-resolved measurements achieving a high resolution. They are also realized thanks to the invention of very short light pulse and various spectroscopies. For example, we can see the real-time dynamics of electrons in a momentum space via time- and angle-resolved photo emission spectroscopy (Tr-ARPES).

In the rest of this section, we present typical examples of the nonequilibrium phenomena induced with AC and DC electric fields and clarify its physics in solids below. Before explaining the detail, we briefly mention several other interesting classes of nonequilibrium phenomena which are intensively studied very recently but we do not treat in this thesis. One of the important classes is the phenomena in the systems periodically driven with something other

[3] Of course, laser light has also the magnetic field component. However, it is much smaller than the electric field component and thus we do not consider the effect of the magnetic field in this thesis. However, the recent development of plasmonic devices realizes the enhancement of the magnetic field [11, 12] and this stimulates the interesting theoretical study [13].

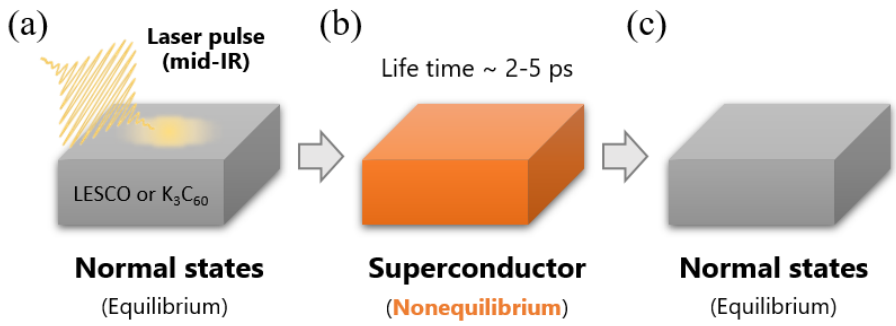

Figure 1.1: Schematic picture of light-induced superconductivity.

than the laser light. For example, it is possible to switch the different static Hamiltonians in various artificial quantum systems such as nitrogen–vacancy centres in diamonds [14], trapped ions [15], and nuclear spins [16, 17]. Utilizing this scheme, the states of matter only existing out of equilibrium, such as discrete time crystals [14–17] , are realized. Another class is the phenomena in the systems including the effect of dissipation (e.g. particle loss and measurement), i.e. open quantum systems. In cold atomic systems, it became possible recently to introduce dissipation in a controlled and coherent way and its effect on many-body quantum systems was already observed in experiments [18]. In such systems, it is known that dissipation makes the Hamiltonian effectively *non-Hermitian* and then it is gathering great attention to investigate the effect of non-Herminicity in condensed matter physics very recently [19–21]. Nonequilibrium phenomena in these two classes are very interesting and gathering attention and we wrote the papers related to these topics [21, 22]. Since this thesis focuses on nonequilibrium phenomena in solids, we do not treat these classes below and please refer to the original papers cited above.

To clarify what happens under AC- and DC-electric fields, we give concrete examples respectively. As an example of AC-field-induced phenomena, we present light-induced superconductivity below. After that, we explain dielectric breakdown as an example of DC-field-induced phenomena.

Light-induced superconductivity

Light-induced superconductivity is very interesting and a recent hot topic [1, 23]. This is a transient phenomenon observed in solids under strong laser fields. Applying laser fields to solids originally being normal states (Fig. 1.1(a)), they show the optical response same as superconducting states transiently (Fig. 1.1(b)). After a while, the system goes back to normal states (Fig. 1.1(c)). The transient appearance of this superconducting-like state is called "light-induced superconductivity". In such a state, we can observe characteristic features in the optical conductivity $\sigma(\omega)$ as the gap-opening near $\omega = 0$ in $\mathrm{Re}[\sigma(\omega)]$ and the divergence of $\mathrm{Im}[\sigma(\omega \to 0)]$.

These signatures are observed in two materials. One is a stripe-ordered cuprate LESCO [4] [1]. In this material, application of middle infrared (mid-IR) laser pulse makes a meta-stable state, whose life time is longer than 100 ps. In this meta-stable state, the superconducting-like state is realized for first 5 ps. The other material is a metallic K_3C_{60} [23]. In this case, the mid-IR laser pulse realizes the transient superconducting-like state for 2 ps. Surprisingly,

[4]The chemical copmposition is $La_{0.1675}Eu_{0.2}Sr_{0.125}CuO_4$.

the light-induced superconducting state appears even above 100 K which is much larger than the critical temperature in equilibrium $T_c(= 20$ K). This suggests that the light-induced superconductivity can opens a way to realize room temperature superconductivity. In contrast, the mechanisms of these phenomena are still under debate and it seems that the mechanisms are different between these two materials because their mechanisms of superconductivity in equilibrium are also considered to be different.

However, it is true that this phenomenon cannot be understood only within the conventional tools in condensed matter physics because we cannot apply standard statistical mechanics to phenomena in such an ultrafast time scale. This is the reason why we call them nonequilibrium phenomena. To understand this phenomenon, we tackle a time-dependent problem in quantum many-body systems and there are several theoretical calculations trying to explain these experiments [24–31] but their discussions are still not conclusive.

In this thesis, we present our theoretical proposals related to AC-field-induced phenomena in Chap. 2 and 3. In particular, we discuss the light-induced "topological" superconductivity in Chap. 2. Our proposals are related to strongly correlated systems and thus we also treat time-dependent quantum many-body problems. We solve them with help of Floquet theory, which enables us to map time-dependent problems to time-independent problems effectively. We explain this technique in Sec. 1.3.

Dielectric breakdown

A typical example of DC-field-induced nonequilibrium phenomena is "dielectric breakdown". We consider the application of a DC electric field to the insulators (Fig. 1.2(a)). A small electric field makes almost nothing to the insulators, but applying a sufficiently strong electric field induces a finite current and make the insulators conductive. This is called dielectric breakdown. The characteristic features of this phenomenon are a threshold behavior and a nonlinear I-V characteristic (Fig. 1.2(b)). This behavior is quite different from the linear response behavior in metallic states and thus it is expected that it cannot be described within conventional theoretical tools. It is the reason why we regard this phenomenon as one of the typical nonequilibrium phenomena. Studies of dielectric breakdown start from C. Zener's work [32] in 1932 [5]. In this work, the author used the theory of non-adiabatic tunneling and discussed the breakdown of band insulators. In recent years, breakdown phenomena in strongly correlated insulators (e.g. Mott insulators) have also been investigated both experimentally [33, 34] and theoretically [35–38] [6].

Although the interesting and important points of light-induced superconductivity was clear for most readers, we consider that those of dielectric breakdown may be more difficult to understand. To clarify them, we explain what are of importance and interest. They are summarized as four points below.

(i) *Fundamental process of nonequilibrium phenomena.*
There appears a charge carrier at the threshold field and the system is driven to a nonequilibrium state. Thus, it is important to study this phenomenon for understanding of initial process of nonequilibrium phenomena in solids.

[5] Surprisingly, it is much older than the proposal of linear response theory although the dielectric breakdown is a nonlinear transport phenomenon.

[6] We note that one of the experiments of Mott breakdown cited here is done with terahertz (THz) laser fields [34]. Because THz electric fields are slower than the typical time scale of electrons' motion, it is expected that the similar effects as DC-field-induced effects are observed.

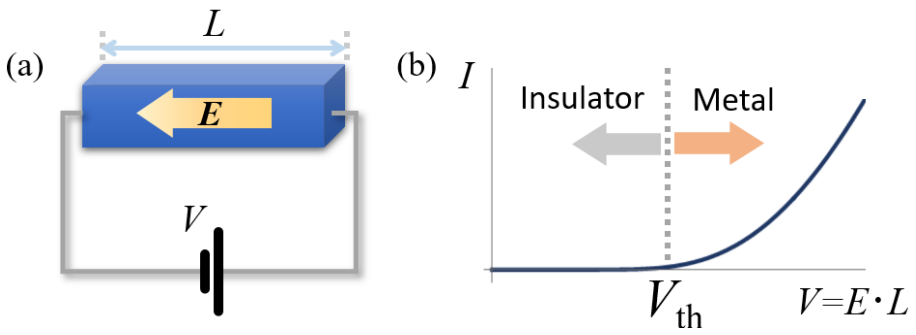

Figure 1.2: (a) Schematic picture of an insulator under a DC electric field $\boldsymbol{E}$. (b) A typical I-V characteristic of dielectric breakdown phenomena. At the threshold voltage $V_{\rm th}$, the nonequilibrium insulator-metal transition occurs.

(ii) *Nonlinear transport phenomena.*
As seen from the I-V characteristic (Fig. 1.2(b)), the breakdown phenomenon is a nonlinear transport phenomena which cannot be captured by linear response theory. Then, to construct the alternative theory beyond linear response, the studies of dielectric breakdown phenomena can give a new insights about that. In addition, it is known that a nontrivial nonlinear transport phenomenon called "negative differential resistance" appears at the voltage sufficiently stronger than the threshold. This is the phenomenon that increasing the electric field reduces the amount of current. The mechanism is theoretically unclear and clarifying it is a challenging problem [38–40].

(iii) *Analog of Schwinger mechanism in high energy physics*
Applying extremely strong electric fields to the vacuum, a pair of electron and positron is created. In high energy physics, this is called "Schwinger mechanism" [41] and related topics form a research field called "strong field physics". To realize this phenomenon, we need electric fields stronger than about 10^{16} V/cm which is impossible to achieve within current experimental technologies. On the other hand, there appears a pair of electron and hole as charge carriers in breakdown of Mott insulators and this is very similar as Schwinger mechanism. Indeed, they share several common physical properties and theoretical description, e.g. pair-production rate and threshold field. Since the Mott breakdown is experimentally achievable, the breakdown in strongly correlated insulators can be used as a "simulator" of Schwinger mechanism and help to investigate strong field physics.

(iv) *Current-carrying metallic state*
Dielectric breakdown phenomena change insulators to current-carrying metallic states and thus can be regarded as nonequilibrium insulator-to-metal transitions induced by electric fields. Not only the breakdown phenomenon itself, but this metallic states are also interesting. For example, it is reported recently that the current-carrying metallic state appears in Cu_2RuO_4 after the Mott breakdown and this state shows very strong diamagnetism [6]. Surprisingly, this current-induced diamagnetism is strongest among non-superconducting materials. This current-carrying state is out of scope of linear response theory and can be regarded as a nonequilibrium steady state. Although there were several attempts to understand nonequilibrium steady states mainly in the field of statistical physics [42], investigation of this kind of states in solids and current-induced

phenomena beyond linear response theory has just started both experimentally and theoretically and thus further developments are desired in future.

From these reasons, the study of dielectric breakdown is meaningful. However, the study of nonequilibrium phenomena induced with DC-fields has been less focused on than the phenomena induced with AC-field. We think that this is because the most studies of DC-field-induced phenomena are limited to mainly the linear response regime. However, the strong electric fields are realized in recent years and then the number of this kind of studies is expected to increase.

In this thesis, we describe our proposal related to DC-field-induced phenomena in Chap. 4. This proposal is closely related to the breakdown in Mott insulators for our setup in this proposal are the same as the setup of dielectric breakdown. In our proposal, we consider the Mott insulator with strong electric fields which do not induce the breakdown and find that the electric fields enhance the magnetic correlation.

1.2 Dynamical controls of solid states

Needless to say, the most important goal of condensed matter physics is to completely understand the physical properties of unknown matter. On the other hand, for the materials whose properties are already well-understood, it is also very important to know how to control their properties. To establish the technique for controlling states of matter is crucial not only for engineering but also for fundamental physics. This is because new controlling schemes open a way to explore new physics. For example, to investigate phase transitions in experiments, we have to control the parameters of the systems systematically.

Experimental techniques for controlling various parameters have been established and applied to experiments and even to engineering. For example, temperature, pressure, chemical doping, magnetic field are typical parameters which can be changed in experiments. The change of these parameters induces the modification of microscopic parameters (e.g. hopping amplitude, interaction strength, filling and so on) and then can realize the phase transitions between equilibrium states. On the other hand, application of strong electric fields brings the system out of equilibrium states and nonequilibrium states are realized transiently. If we can do this in a controlled way, controlling states of matter is extended to nonequilibrium states. We call the controls which are realized with utilizing nonequilibrium phenomena "dynamical controls". Of course, the nonequilibrium phenomena shown in the previous section, light-induced superconductivity and dielectric breakdown, are used for dynamical controls. Light-induced superconductivity can be used for controlling superconducting-like states even at high temperature. Dielectric breakdown can be regarded as a field-induced switching from insulators to metals. In this section, we show the other examples which are interesting from the viewpoint of dynamical controls.

Before explaining the other examples, we mention the advantages of dynamical controls over usual controls near equilibrium. One is that the controls difficult or impossible in equilibrium can be made possible. For example, although the critical temperature in usual equilibrium superconductors are limited to low temperature, light-induced superconductivity has a potential that it makes possible to switching the superconductivity even at room temperature. The other is that the ultrafast controls are made possible. As we mentioned above, we cannot apply standard statistical mechanics to the phenomena in the ultrafast timescale (e.g. fs or ps time scale). Thus, it is inevitable to use nonequilibrium phenomena. The ultrafast controls enable us to change a state of matter to the different state for very short time. It means that it is easy to return to the original state with turning off the electric field. This is quite different

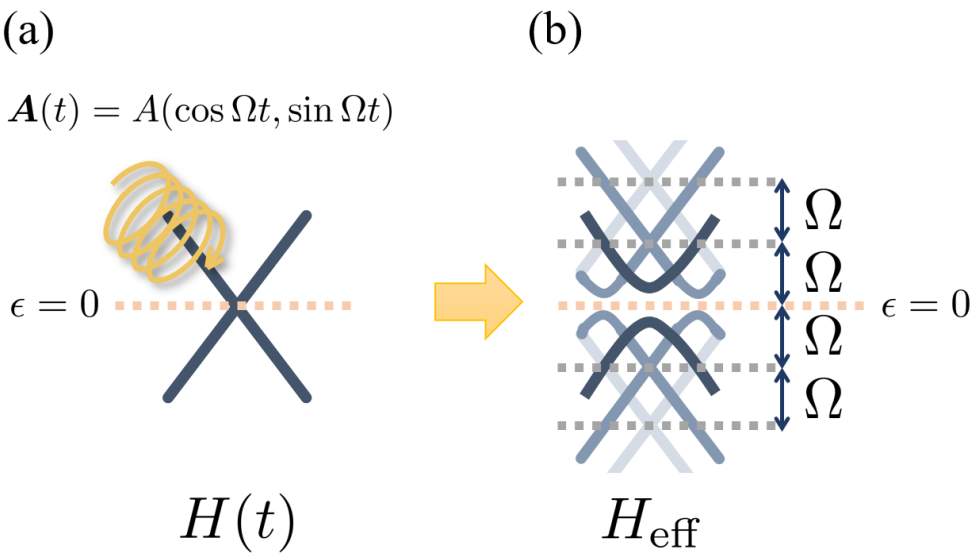

Figure 1.3: Schematic picture of the modification of a band structure with AC electric fields.(a) We consider the band structure in solids (massless Dirac cone) and application of laser light ($\boldsymbol{A}(t) = A(\cos\Omega t, \sin\Omega t)$, i.e. circularly polarized laser) to the solids. (b) When the laser light is irradiated to the solids, the band structure is effectively modified like this. This structure is experimentally observed [3, 4].

from the control with chemical doping. Furthermore, this is considered to be used as a new principle of ultrafast switching device from the engineering point of view.

To clarify what we mean by dynamical controls and their advantages explained above, we give two types of dynamical controls. One is control of band structures and the other is control of magnetism.

Controls of band structures

How are band structures modified under strong electric fields? Of course, weak electric fields do not change band structures and thus we consider the effect of electric fields with original band structures. However, when the intensity of electric fields becomes sufficiently strong, the situation changes. Electronic states in solids (i.e. Bloch states) couple to the applied AC electric fields (Fig. 1.3 (a)) and form the "dressed states" which are called Floquet states or Floquet-Bloch states (Fig. 1.3 (b)). These names come from "Floquet theory" which is a theoretical framework for time-periodic quantum systems and we explain its detail in Sec. 1.3. The spectrum of the Floquet states are the eigenvalues of the effective Hamiltonian describing the nonequilibrium steady states induced with AC driving (The definition of the effective Hamiltonian is shown in Sec. 1.3).

As shown in the Fig. 1.3 (b), the Floquet states also form a band structure like usual Bloch states, but there are significant differences. One is that Floquet states have a periodic structure in the energy direction as shown in Fig. 1.3 (b) [7]. This can be understood as an

[7]Strictly speaking, the eigenvalues of the effective Hamiltonian are different from the usual "energy" due to this periodic structure in the energy direction. Thus, they are called "quasi-energy" in the studies with Floquet theory.

analog of the periodicity of Bloch states in the momentum space. Bloch states appear in a periodic potential, and thus the periodicity related to the conjugate variables, which are namely momentum, emerges. The other difference is that the effective band structure reflects the symmetry of electric fields. For example, the appearance of the gap at the zero energy, where the original band structure is gapless, reflects the time-reversal symmetry breaking of circularly polarized laser light $\boldsymbol{A}(t) = A(\cos\Omega t, \sin\Omega t)$. Indeed, linearly polarized laser light, e.g. $\boldsymbol{A}(t) = A(\cos\Omega t, \cos\Omega t)$, cannot open the gap at zero energy in this band structure. This kind of the manifestation of symmetry is not limited to this specific case. It is shown that the symmetry of the effective Hamiltonian is determined by the symmetry of the original time-dependent Hamiltonian in general [43].

Utilizing these differences, the controls of band structures with laser light have been proposed by many researchers [2, 44–50]. A pioneering work in this direction is the work by T. Oka and H. Aoki in 2009. They consider graphene irradiated by circularly polarized laser light and show how the band structure and the transport properties are modified. The band structure is modified like Fig. 1.3 (b) and the finite gap appears at the Dirac point. They show that this gap-opening is the topological phase transition in the Haldane model defined on a honeycomb lattice [51] and there appear the chiral edge modes corresponding to the topological invariant called Chern number. This state is called "Floquet topological insulator" and similar phenomena are investigated related to various topological phases including Z_2 topological insulators [45], fractional Chern insulators [52] and Weyl semimetals [53].

From the experimental point of view, similar phenomena first observed in the Tr-ARPES measurement at the surface of the topological insulator Bi_2Se_3 in 2013 [3]. After that, a similar setup as the original proposal by Oka and Aoki is realized in the system of cold atoms in an optical honeycomb lattice and the topological phase transitions are experimentally observed in 2014 [54]. Since atoms are charge neutral, they used a technique called "lattice shaking" to induce the artificial gauge fields corresponding to laser light. They directly change the optical lattice potential time-dependently and atoms feel the force which gives the similar effect as the electric fields. This kind of technique, which is the design of the time-dependence in the Hamiltonian to realize desired quantum states, is called "Floquet engineering" and this has been developed in the field of cold atomic systems and established as one of the important experimental techniques for preparing the experimental setup. For example, the other group is also realized the Haldane model in a similar way to investigate the quantum dynamics in topological systems [55]. In contrast, the experimental observations of Floquet states in solids have been few and limited to the the surface of Bi_2Se_3 [3, 4] and there have been the ARPES measurements until quite recently. However, a preprint about the observation of anomalous Hall effect in graphene irradiated by circularly polarized laser light has been posted on arXiv very recently in 2018 [5]. This anomalous Hall effect is expected to be an evidence of Floquet topological insulators. It is important that the transport measurement, which provides macroscopic observables, gives the evidence because this opens a way to control the macroscopic properties of solids via engineering of band structure with laser light.

In summary, dynamical controls of band structures are theoretically proposed and already experimentally realized even in solids. In these studies, topological phases, characterized by band structures, play an important role. However, band structure can affect the various physical properties of solids and thus the investigation should not be limited to topological phenomena. Since the dynamical controls of band structures can realize new band structures different from equilibrium states as explained above, we expect that the dynamical controls of band structures are applied to a variety of materials and help to explore a new nonequilibrium phenomena in solids.

As described above, the dynamical controls of band structures are mainly considered in weakly interacting systems (e.g. semiconductors, graphene). To extend these studies and find new schemes for controls, we have investigate *strongly correlated electron systems* and explain the results about them in this thesis. In Chap. 2, we discuss the control of the band structure of the Bogoliubov quasi-particles in d-wave superconductors which are typically realized in strongly correlated electron systems. In Chap 3, we consider the control of the band structure strongly renormalized by electron correlation in heavy fermion materials.

Controls of magnetism

The control of magnetism with laser fields is one of the most important examples of dynamical controls. It is because this control can be applied to spintronic devices. Spintronics is a technology alternative to electronics and expected to realize efficient data storage and transfer. The core process in spintronics is the control of spin degrees of freedom. Making shorter the time for this process, it should be possible to achieve higher efficiency and faster processing. For this purpose, dynamical controls of magnets with laser light are anticipated to be used because applying strong laser light can induce nonequilibrium collective phenomena related spins and then the spin states are changed in an ultrafast time scale (e.g. fs or ps time scale). To consider the control in this time scale, equilibrium statistical mechanics cannot be used and we need to consider nonequilibrium phenomena. In this sense, the dynamical control of magnets is a promising way to utilize nonequilibrium states for engineering. Indeed, this direction has been gathering great attention and the research field of "ultrafast spintronics" has been formed [56].

Studies of dynamical controls of magnetism start from the discovery of the ultrafast demagnetization, which is a phenomenon that application of laser light to ferromagnets reduces the magnetization in the ultrafast time scale. The first observation was reported by E. Beaurepaire *et al.* in 1996 and they reported that application of 60 fs pulse to ferromagnetic nickel induces the 40 % reduction of the magnetization for almost 5 ps [57]. This experiment stimulated the other researchers and then the controls of magnetization with laser light have been intensively investigated. For example, while the above experiment is understood as a thermal effect induced by the rapid optical absorption, non-thermal effect inducing magnetization with circularly polarized laser light is claimed to be observed in a multiferroic ferromagnet $DyFeO_3$ [58]. In addition, the application of a similar non-thermal effect inducing magnetization to the all-optical magnetic recording by femtosecond laser pulses was already discussed [59]. In summary, the control of magnetization has been well-studied and is reaching to possible application to spintronic devices.

While these are the manipulation of the magnetization, other kinds of controls in magnets are also discussed in recent years. One is the control of quantities other than magnetization itself. For example, it is discussed that application of spatially modulated laser light induces the spin current in multiferroic magnets [60]. Spatial modulation of laser fields is expected to be realized using plasmonic microstructures [61–63] and thus it should be useful for spintronic devices. The other is the control of microscopic interaction between spins. In magnets based on simple Mott insulators, antiferromagnetic Heisenberg interaction is known to be dominant. With a second-order perturbative calculation in a single-band Hubbard model, we can calculate the effective spin model as

$$H_{\text{eff}} = J_H \sum_{\boldsymbol{r}\boldsymbol{r}'} \boldsymbol{S}_{\boldsymbol{r}} \cdot \boldsymbol{S}_{\boldsymbol{r}'}, \tag{1.1}$$

where $\boldsymbol{S}_{\boldsymbol{r}}$ is a spin-1/2 operator defined on a site $\boldsymbol{r}$ and $J_H = 4t^2/U$ with a hopping amplitude t and a Coulomb interaction U in the Hubbard model. Here, J is obviously positive. However,

it is reported that the sign of the Heisenberg coupling can be changed with laser irradiation [64, 65]. They employ a second-order perturbative calculation with considering the virtual processes via Floquet states induced with laser light and obtain the effective Heisenberg coupling as

$$J_{\text{eff}} = \sum_n \frac{4t^2 |J_n(A)|^2}{U - n\omega} \tag{1.2}$$

$$= J_H \left(1 + \frac{1}{2\left[1 - \left(\frac{\omega}{U}\right)^2\right]} A^2 \right) + \mathcal{O}(A^4), \tag{1.3}$$

where A and ω are the amplitude and the frequency of the laser fields. From eq. (1.3), we can see that laser field whose frequency ω is larger than U and intensity A is sufficently strong makes the effective coupling J_{eff} negative. This mechanism is expected to be used for antiferromagnetic-ferromagnetic switching in an ultrafast time scale, which should be difficult in current techniques in spintronics. Besides the Heisenberg-type interactions existing even without laser light, we can also discuss other interactions appearing only when applying laser light. For example, it is theoretically shown that application of circularly polarized laser light to Mott insulators breaks the time-reversal symmetry and then induces the scalar-chirality-type interaction $H_{\text{Chiral}} = \sum_{ijk} \boldsymbol{S}_i \cdot (\boldsymbol{S}_j \times \boldsymbol{S}_k)$ which is not allowed when preserving the time-reversal symmetry [66, 67]. This interaction is known to induce chiral spin liquids [68–70] and thus this scheme is used for controlling such an exotic states of matter.

In this thesis, we present our results related to the dynamical control of microscopic interaction. We consider the application of DC electric fields or low-frequency AC fields (e.g. THz fields) and show that the Heisenberg-type interaction is enhanced along the electric fields. In Chap. 4, we show this argument and apply it to control the magnetic orders, spin liquids, and topological phases in quantum spin systems.

1.3 Theoretical developments

As described above, fascinating nonequilibrium phenomena have been found and various schemes for dynamical control utilizing them have also been proposed and are almost being realized in experiments. However, the physics behind them cannot be described with conventional tools in condensed matter theory. Then, we need new tools to tackle the nonequilibrium phenomena. Fortunately, thanks to the recent developments in condensed matter theory and statistical physics, our knowledge about theory for nonequilibrium phenomena in quantum many-body systems is rapidly growing and several useful tools are being established. In this section, we first briefly review such theoretical developments and then give an explanation focusing on one of theoretical treatments called Floquet theory which is a main theoretical tool in Chap. 2 and Chap. 3.

Overview of theoretical treatments

One of the most crucial problems is that we cannot apply standard statistical mechanics. In the transient phenomena induced with strong laser pulse, the time scale is too short to apply it. For nonequilibrium steady states, we need the information far from equilibrium in the regime going beyond linear response. In such a situation, what we can safely use is just quantum mechanics. Thus, we have to solve time-dependent quantum many-body problems to investigate nonequilibrium phenomena in solids. Of course, it is impossible to solve these problems in general and thus we have to take some approximations.

There are various approaches with different approximations to tackle the nonequilibrium phenomena and we can classify them. First, the approaches are divided into numerical and analytical approaches. Numerical approaches make it possible to obtain the real-time dynamics for a broad range of parameters and thus they are very strong when the numerical cost is allowed. In contrast, numerical calculations for long-time and large-size are difficult in general and it is difficult to qualitative understanding of phenomena via numerical results in many cases. On the other hand, the analytical approaches are possible for very limited parameters (i.e. integrable models) or some simplified models, but they can give a qualitative understanding and sometimes provide universal properties not depending on the specific models.

There are many kinds of numerical approaches for nonequilibrium phenomena and the new approaches are also being proposed intensively. It is difficult to give a systematic review and it is out of scope of this thesis because our studies are mainly based on the analytic approach. Thus, we only mention several well-known approaches here. For one-dimensional systems, there exists a very powerful approach called time-dependent density matrix renormalization group (Time-dependent DMRG) [71–74]. This approach is based on a variational method about a trial wave function described with matrix product states and known to give a numerically exact results even for intermediate system size. For two- or three-dimensional systems, nonequilibrium dynamical mean-field theory (Nonequilibrium DMFT) is known to be a powerful methods for calculating nonequilibrium dynamics [75]. This approach is based on the Keldysh's Green function formalism and an approximation of taking only spatially-local correlation into account is used. This approximation corresponds to mapping the generic quantum many-body problems to single-impurity problems, which are known to be relatively easy to solve. Thus, using nonequilibrium DMFT with some solver of the impurity problem, we can calculate the many-body quantum dynamics. Note that there does not exist a very strong solver like continuous-time quantum Monte Carlo method [76] for equilibrium DMFT [77] and thus we have to rely on some diagrammatic approach (e.g. non-crossing approximation). Thus, it is important task to establish a strong solver for the nonequilibrium impurity problem.

When we use analytic approaches, we have two choices. One is to choose some *exactly solvable models* whose dynamics can be calculated analytically or with easy numerics. In this direction, nonequilibrium dynamics of conformal field theory (CFT) describing many one-dimensional quantum many-body systems is actively studied [78]. Due to high symmetry of the theory, we can use several analytical techniques and get analytical results. It is very useful for discussing universal properties of nonequilibrium phenomena, but the applicable models are limited. The other way is to use some simplified models, which make the problem easy enough to solve analytically or with easy numerics. In this direction, the approach that we expected to be promising is to use the effective Hamiltonian in Floquet theory. It is recently established and very useful for discussing the nonequilibrium steady states under AC fields and thus we explain this treatment below. Indeed, this treatment plays an important role in Chap. 2 and Chap. 3.

Floquet theory for quantum many-body systems[8]

Floquet theory is a theoretical framework for time-periodic quantum systems based on Floquet's theorem. Floquet's theorem is originally a theorem for differential equations including a periodic parameter. In most cases for application to physics, this periodic parameter represents

[8]There are nice review papers on Floquet theory closely related to the contents in this subsection. They are cited as [7, 79, 80].

time. Thus, we here explain the Flqouet's theorem for time-periodic Schrödinger equation

$$i\frac{d}{dt}\left|\psi(t)\right\rangle = H(t)\left|\psi(t)\right\rangle, \tag{1.4}$$

where the Hamiltonian is time-periodic, i.e. $H(t+T) = H(t)$. Floquet's theorem says that the solution of the Schrödinger equation (1.4) is given as a product of exponential function of time $e^{-i\epsilon t}$ and time-periodic states $|\phi(t)\rangle$, i.e. $\psi(t) = e^{-i\epsilon t}|\phi(t)\rangle$ and $|\phi(t+T)\rangle = |\phi(t)\rangle$ [9]. ϵ is a quantity called *quasi-energy*. Using the Floquet's theorem, we can expand $|\phi(t)\rangle$ in a Fourier series as $|\phi(t)\rangle = \sum_{n=-\infty}^{\infty} e^{in\Omega t}|\phi_n\rangle$ with $\Omega = 2\pi/T$. Substituting this series and the Fourier series expansion of the Hamiltonian $H(t) = \sum_{n=-\infty}^{\infty} H_n e^{in\Omega t}$ into eq.(1.4), we obtain equations of the Fourier modes as

$$\sum_{m,n=-\infty}^{\infty} (H_{m-n} + n\Omega\delta_{mn})\left|\phi_n\right\rangle = \epsilon\left|\phi_m\right\rangle, \tag{1.5}$$

which is also written in a matrix form as

$$\begin{pmatrix} \ddots & & & & \\ & H_0+\Omega & H_{+1} & H_{+2} & \\ & H_{-1} & H_0 & H_{+1} & \\ & H_{-2} & H_{-1} & H_0-\Omega & \\ & & & & \ddots \end{pmatrix} \begin{pmatrix} \vdots \\ |\phi_{+1}\rangle \\ |\phi_0\rangle \\ |\phi_{-1}\rangle \\ \vdots \end{pmatrix} = \epsilon \begin{pmatrix} \vdots \\ |\phi_{+1}\rangle \\ |\phi_0\rangle \\ |\phi_{-1}\rangle \\ \vdots \end{pmatrix}. \tag{1.6}$$

Here, we just rewrite the original Schrödinger equation (1.4) into the equations for Fourier modes (1.5). This equation is mathematically equivalent, but the form of eq. (1.5) is suggestive. It is because this equation looks like an eigenvalue equation and does not include any time-dependence explicitly. In other words, it means that the time-dependent problem is mapped to the time-independent eigenvalue problem. This eigenvalue problem can be interpreted as one of a static many-"bands" systems as shown in Fig. 1.4. The "band" corresponds to the diagonal sectors represented by $H_0 + n\omega$ ($n \in \mathbb{Z}$). Corresponding to the time-periodicity, there appears the periodicity with Ω in the quasi-energy direction. The off-diagonal components, i.e. H_n ($n \neq 0$), give hybridization between the "bands". We can interpret H_n (H_{-n}) as a operator corresponding to the n-photon absorption (emission) process and understand in the way that such absorption and emission processes connect the sectors with different photon numbers $H_0 + n\omega$ [10].

It seems that the above mapping makes the problem easier because it is reduced to the static problem. However, as we mentioned above, the equation (1.5) is equivalent to the original Schrödinger equation and thus the difficulty of time-dependent problems still remains. The reason why the problem is still difficult is that the matrix of the above eigenvalue problem is infinite-dimensional. To go further, we have to reduce the dimension of matrix. One of the ways to reduce it is just to truncate the matrix at a certain size. To obtain the reliable results, we can check whether the results are unchanged or not and, if they are not changed, we can believe them. This approach is usefully applicable to various systems, but it is needed to diagonalize large matrices with numerical calculations. Thus, it is difficult to obtain qualitative

[9] Strictly speaking, the solution of the Schrödinger equation (1.4) is given as a superposition of this product form.

[10] We here use the term "photon" just for interpretation and this does not mean the elementary quanta of electromagnetic fields. We consider a generic time-dependent Hamiltonian up to here and we cannot determine the physical meaning without specifying the physical systems.

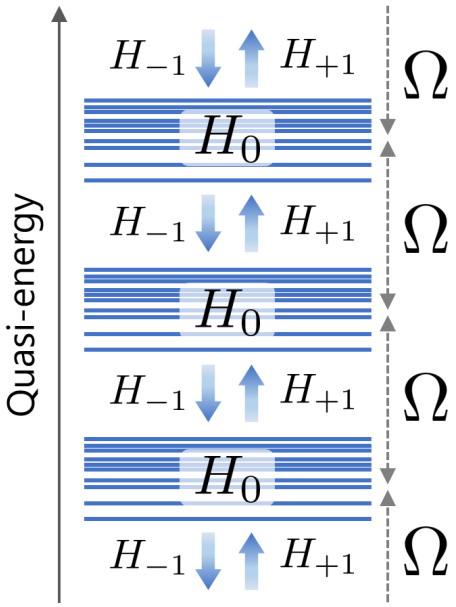

Figure 1.4: Schematic picture of a static many-"bands" system corresponding to the eigenvalue problem (1.5). The "band" corresponds to the diagonal sectors represented by $H_0+n\omega$ ($n \in \mathbb{Z}$). The off-diagonal components H_n ($n \neq 0$) give hybridization between the "bands".

understanding. For this purpose, the other way is much better. This is the approach to use an effective Hamiltonian in the high frequency limit. Taking this limit, the sectors with different photon numbers deviate from each other and the effect of absorption and emission of photons are treated perturbatively. Thus, we focus on one sector and project out the other sectors with including the effect from other sectors as a perturbation. Due to the projection, we can obtain the effective Hamiltonian whose dimension is the same as that of the original Hamiltonian $H(t)$.

Several approaches for calculating the effective Hamiltonian are known, e.g. Flouqet-Magnus expansion, van-Vleck expansion and Brillouin-Wigner expansion. These expansions should be equivalent when taking a sufficient number of higher order terms into account, but they can give different results for truncating at a certain order [11]. In practice, we use the truncated effective Hamiltonian and it can be a problem. Thus, we have to be careful about that. However, these expansions give the same result up to the first order [12] as

$$H_{\text{eff}} = H_0 + \sum_{n=1}^{\infty} \frac{[H_n, H_{-n}]}{n\omega} + \mathcal{O}(\omega^{-2}). \tag{1.7}$$

Thus, we use the above expansion (1.7) up to the first order in this thesis. Fortunately, all the results in this thesis can be understood within the first order.

This effective Hamiltonian approach enables us to obtain a finite-dimensional and static Hamiltonian (1.7) from the time-dependent problem (1.4). Because the effective Hamiltonian

[11] It is known that there is a relation among these three expansions. Mikami *et al.* give a comprehensive paper about the relation between them [81]. For details, please see this paper.

[12] Strictly speaking, the first order terms of Floquet-Magnus expansion include the other terms depending on the initial time of the dynamics, which do not exist in the other expansions. However, we focus on the macroscopic quantity and phases of matter induced with laser light in this thesis and they do not depend on the initial time which corresponds to the carrier envelope phase of laser light. Thus, we do not consider the terms depending on the initial time.

does not depend on time, theoretical techniques developed for equilibrium states are expected to be applicable to it. However, the applicability is actually unclear only based on the above discussion. It is because the original problem (1.4) is *time-dependent* and thus it is not clarified when the description of the *static* effective Hamiltonian works. To answer this questions, we have to consider the real-time dynamics of quantum many-body systems. In general, it is difficult to know this dynamics, but we can know only when the effective Hamiltonian (1.7) gives a valid description within the real-time dynamics. This is unveiled by the recent studies in statistical physics about thermalization in closed and periodically-driven quantum systems. In the following, we explain when the effective Hamiltonian is valid and whether the techniques in equilibrium can be applicable to the effective Hamiltonian based on these studies. We start from the case of closed quantum systems and introduce an important concept, "*Floquet prethermalization*". After that, we explain the realistic case in solids realized with laser pulse having a finite width.

Let us consider the dynamics of periodically-driven quantum many-body systems. Naively thinking, periodic driving (e.g. irradiation of laser light) supplies the energy to the system and then the closed system is expected to heat up. Finally, the system is considered to reach a completely randomized state corresponding to infinite temperature states in the long time limit. Thanks to the recent numerical study [82], this intuitive argument is confirmed to be correct. It is shown that the expectation value of an observable $\hat{O}$ reaches its thermal average at the infinite temperature, i.e. $O(t) = \langle\psi(t)|\hat{O}|\psi(t)\rangle \to \langle\hat{O}\rangle_{T=\infty}$ in the long time limit where $\langle\hat{O}\rangle_{T=\infty} = \mathrm{Tr}[\hat{O}]$ (see Fig. 1.5). This result suggests that we cannot see the signature of the effective Hamiltonian in this real-time dynamics because no Hamiltonian appears in the thermal average at the infinite temperature $\langle\hat{O}\rangle_{T=\infty}$.

However, there is one possibility for the appearance of the effective Hamiltonian. It is the possibility that there exists some "prethermalized state" and this state is described with the effective Hamiltonian at finite temperature. Surprisingly, this statement is proved theoretically [83–85] and numerically confirmed in several concrete models [84, 86]. This prethermalized state is called "Floquet prethermalized (FP) state" and it is realized in a transient time scale before heating up as shown in Fig. 1.5. In the FP state, the expectation value $O(t)$ is approximated with $\langle\hat{O}\rangle_{H_{\mathrm{eff}},\beta_{\mathrm{eff}}} = \mathrm{Tr}[\hat{O}\exp(-\beta_{\mathrm{eff}}H_{\mathrm{eff}}^{(n_0)})]$ where $H_{\mathrm{eff}}^{(n_0)}$ is the high-frequency expansion of the effective Hamiltonian truncated up to n_0-the order and $1/\beta_{\mathrm{eff}}$ is the effective temperature determined with the condition of the energy conservation [13]. The remarkable feature of the FP state is that its lifetime τ_{FP} becomes exponentially longer with increasing the frequency, i.e. $\tau_{\mathrm{FP}} = \mathcal{O}(\exp(\omega/J))$ where J is the typical energy scale of the original Hamiltonian $H(t)$. Because the thermalization time τ_{th} (the time for thermalizing from the initial state to the FP state. Please see Fig. 1.5) is short in most systems, it means that we can definitely realize the FP state if we choose the sufficiently high frequency. The reason why FP states appear is intuitively understood as follows. The energy injection by periodic driving is determined by the frequency of driving. If the frequency is sufficiently higher than the typical energy scale of the original Hamiltonian, it takes exponentially long time to absorb the large energy. Thus, the state where *the system feels periodic-driving but absorbs the energy very slowly* appears. This is the FP state. The existence of FP states is very important because the physical meaning of the effective Hamiltonian is clarified and then we can tackle the noequilibrium dynamics with the effective Hamiltonian. Furthermore, it is also important that the expectation values in FP states are calculated with thermal average. It means that we can apply the theory developed in

[13] This condition is written as $\langle H(0)\rangle_{\mathrm{init}} = \langle\hat{O}\rangle_{H_{\mathrm{eff}},\,\beta_{\mathrm{eff}}}$. This equation means that the energy is effectively conserved in the dynamics until the lifetime of the FP state τ_{FP}. Solving this equation for β_{eff}, we can get the effective temperature in the FP state.

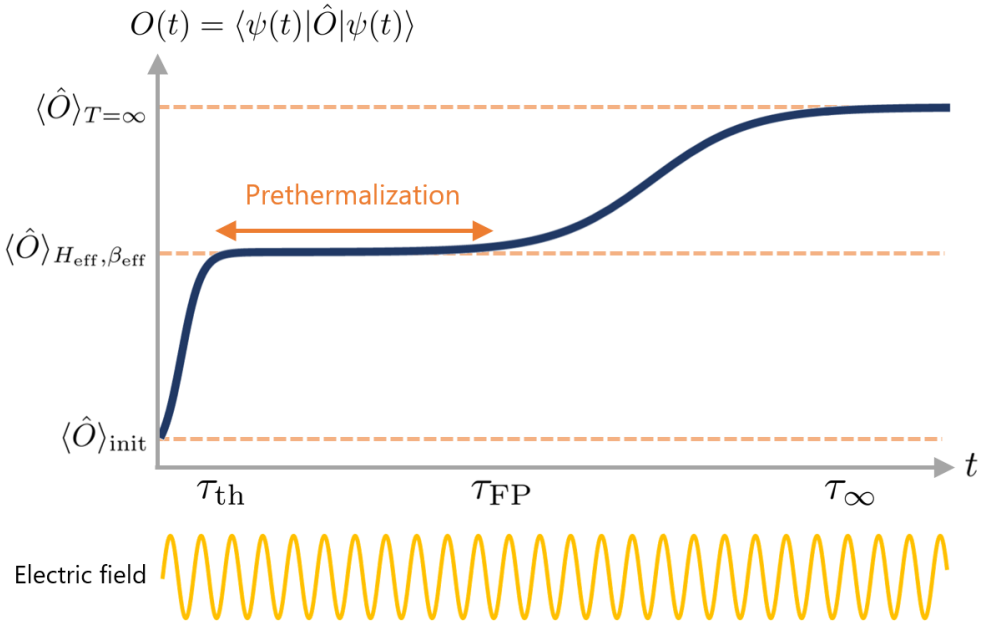

Figure 1.5: Typical real-time dynamics of closed quantum systems under the continuous periodic driving. The expectation value $\hat{O}(t)$ starts from the initial value $\langle\hat{O}\rangle_{\rm init} = \langle\psi(0)|\hat{O}|\psi(0)\rangle$ and reaches $\langle\hat{O}\rangle_{T\to\infty} = {\rm Tr}[\hat{O}]$. In the intermediate time scale between $\tau_{\rm th}$ and $\tau_{\rm FP}$, the Floquet prethermalized (FP) state appears and $O(t)$ is approximated with $\langle\hat{O}\rangle_{H_{\rm eff},\beta_{\rm eff}} = {\rm Tr}[\hat{O}\exp(-\beta_{\rm eff}H_{\rm eff}^{(n_0)})]$.

the study of equilibrium states. In this thesis, we apply the techniques for strongly correlated electrons (e.g. slave boson methods in Chap. 3) based on this point.

As described above, the physical meaning of the effective Hamiltonian in the dynamics of closed periodically-driven quantum many-body systems is clarified and it gives a significant foundation of the Floquet theory for many-body systems. However, we have to modify several points in the above discussion to apply the concept of the FP state to the realistic situation of experiments in solids. There are two points to modify.

One is that strong laser light is expected to be realized as a finite-width pulse shown in Fig. 1.6. It is different from the above discussion since we considered the continuous wave above. This difference gives two modification in the real-time dynamics. One is the thermalization time is expected to be longer because the strength of laser light becomes smaller. The other point is that the application of laser light stops before heating up when the pulse width is sufficiently short. From this point, the laser light should be shorter to avoid the heating, but the laser light must be longer than the thermalization time. Therefore, we have to choose the intermediate width of laser pulse.

The other point is that solids are not closed quantum systems and inevitably couple to various environments, e.g. phonons. It is quite different from cold atomic systems. Thus, we cannot naively apply the theory of closed systems to solids, but it is possible in our case because the pulse width is typically very short and then the lifetime $\tau_{\rm FP}$ is also short. Since the dynamics of environments is typically much slower than that of electrons, the systems are approximated to be a closed quantum systems only in an ultrafast time scale. Indeed, the signature of Floquet states is observed in experiments where the short pulse whose width is 100

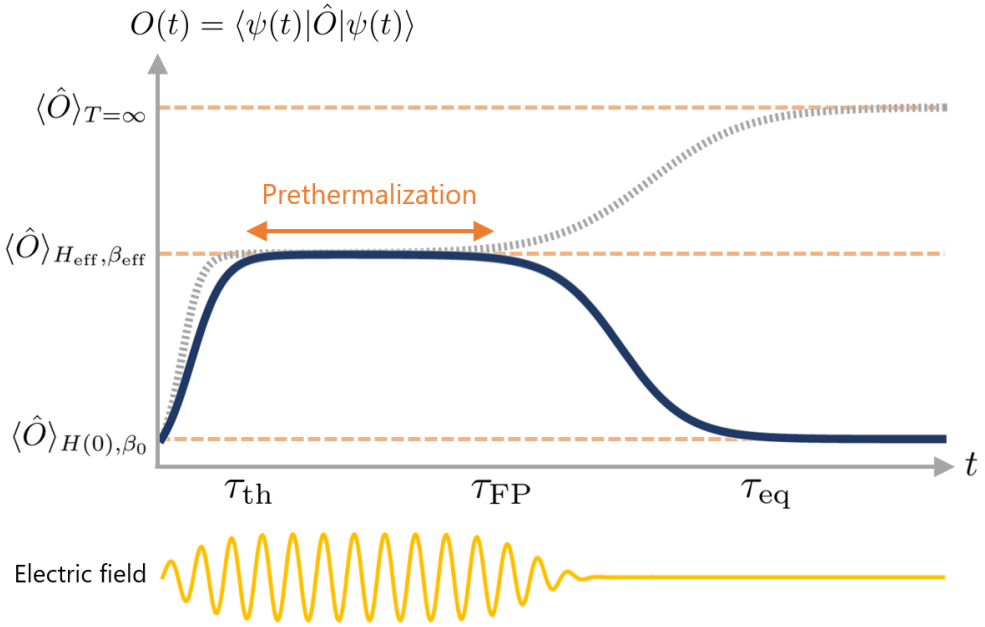

Figure 1.6: Typical real-time dynamics of closed quantum systems under the pulse driving in solids. The expectation value $\hat{O}(t)$ starts from the thermal value $\langle\hat{O}\rangle_{H(0),\beta_0} = \mathrm{Tr}[\hat{O}\exp(-\beta_0 H(0))]$. Before $O(t)$ reaches $\langle\hat{O}\rangle_{T\to\infty} = \mathrm{Tr}[\hat{O}]$, the driving is stopped and $O(t)$ goes back to the thermal value $\langle\hat{O}\rangle_{H(0),\beta_0}$. In the intermediate time scale between $\tau_{\rm th}$ and $\tau_{\rm FP}$, the Floquet prethermalized (FP) state appears and $O(t)$ is approximated with $\langle\hat{O}\rangle_{H_{\rm eff},\beta_{\rm eff}} = \mathrm{Tr}[\hat{O}\exp(-\beta_{\rm eff}H_{\rm eff}^{(n_0)})]$.

fs is used [3, 4]. However, the condition of adequate pulse width is expected to depend on the detail of the experimental setups. To clarify it, we need further studies both theoretically and experimentally. In this thesis, we discuss the experimental conditions to confirm our proposals using Floquet states in Chap. 2 and Chap. 3 respectively. In addition, the existence of the environment makes the other subtle difference. It is that the system go back to the thermal states after finishing the driving due to the environment. If we start from the thermal states, it is expected that the system returns to the initial states. It is different from the closed quantum systems.

We have explained the theoretical description with Floquet theory for quantum many-body systems. In recent years, the theoretical developments of Floquet theory is very rapid and thus we have not explained some of the important developments related to Floquet theory in many-body quantum systems. For example, the relation between Floquet states and many-body localization (MBL) [87, 88], which is roughly speaking the many-body version of Anderson localization [89, 90], is not mentioned above. As we discussed, periodic driving in closed quantum systems induces heating in the long time limit, but MBL prevents the heating. Thus, the periodically-driven many-body localized states reaches nontrivial steady states in the long time limit and their properties are extensively investigated. In addition, we did not mention the phases of matter only existing in periodically-driven systems. The typical examples are anomalous Floquet topological states [49, 50] and discrete time crystals [91, 92] (the latter was briefly mentioned in Sec. 1.1). The investigation of these states is also important and indeed energetically done in recent years.

1.4 Our motivation

In Sec. 1.1 and 1.2, we have explained the nonequilibrium phenomena in solids under AC and DC electric fields and the dynamical controls realized with these nonequilibrium phenomena. These phenomena are not described within the theoretical tools developed in conventional condensed matter theory, but there are theoretical developments providing new theoretical tools for treating nonequilibrium phenomena. We explained these developments in Sec. 1.3 and devoted most part of the section for explanation of Floquet theory for quantum many-body systems which enables us to analyze solids under AC electric fields.

These situations excite us because interesting and unexplored phenomena are found in experiments and the theoretical tools for them are being established recently. We think that now is the time for theorists to apply new theoretical tools to cutting-edge experimental setups and find new exciting phenomena as the application of linear response theory gave fruitful results and developments in condensed matter physics. Furthermore, as explained in Sec. 1.2, nonequilibrium phenomena enable us to control states of matter dynamically and can realize controls which cannot be done in equilibrium. Then, such controlling schemes have a potential to bring a breakthrough to a future technology or to be a new mechanism for future devices. Therefore, we believe that studying nonequilibrium phenomena and dynamical controls in solids is one of the most important future directions in condensed matter physics.

To contribute to the development in this direction, we have studied nonequilibrium phenomena and proposed new schemes for controlling states of matte using them. In particular, we have studied them in strongly correlated quantum systems. There are two reasons why we focus on them.

One is that strongly correlated systems show various interesting phases of matter. The most famous example is high-temperature superconductors in cuprates as briefly mentioned in Sec. 1.1. The electron correlation is supposed to play an important role for realized d-wave superconductivity in cuprates [10]. Magnetism is also crucially related to electron correlation and magnetic spin systems can show exotic quantum states of matter like quantum spin liquids [93, 94] or the Haldane-gap phase [95, 96] due to strong correlation between spins. Furthermore, heavy fermion systems show rich phase diagrams including magnetic phases and superconducting phases due to the competition between two correlation effects, Kondo effect and Ruderman-Kittel-Kasuya-Yoshida (RKKY) interaction. All these are very important and interesting topics having been investigated in condensed matter physics. To discuss the control of such phases, we have to understand the interplay between laser light and strong correlation. This is a difficult task, but it is worthy of being studied.

The other is that strongly-interacting systems become tractable recently. As explained in Sec. 1.3, recent theoretical developments clarify the relation between the real-time dynamics and the effective description via Floquet theory. It enables us to treat the nonequilibrium strongly correlated quantum systems using the effective Hamiltonian. The strength of the approach with the effective Hamiltonian is that we can use the technique developed in physics of equilibrium systems. Although the effective Hamiltonian only gives the information in the high-frequency limit, this approach can be a very powerful tool for exploring strongly correlated systems. From these reasons, we have studied nonequilibrium phenomena and dynamical controls in them. In the following chapters, we explain the results in our studies.

1.5 Overview of this thesis

Finally, we explain the organization of this thesis. This thesis consists of five chapters, and Chaps. 2, 3, and 4 present our results. In this chapter, we gave an introduction of "nonequilibrium phenomena" and "dynamical controls" and explained recent theoretical developments related them. Based on the contents in this chapter, we explain our recent results in the following chapters. In each chapter, we give different theoretical proposals in strongly correlated materials. The proposals in Chap.2 and 3 are related to AC fields. The proposal in Chap.4 is closely related to DC field, but also related to slow AC fields, e.g. THz fields.

In Chap. 2, we explain our proposal to realize laser-induced topological superconductivity in d-wave superconductors. Based on the effective Hamiltonian approach, we show that the circularly polarized laser light modifies the Bogoliubov spectrum and realize a full-gap superconductor effectively. We find that this full-gap superconducting state is topologically nontrivial and characterized by Chern numer. The experimental realization of topological superconductivity is quite limited, and thus our proposal is expected to be useful because our proposal can be applicable to d-wave superconductors which are widely realized in strongly correlated electron materials including cuprate supercondutors.

In Chap. 3, we study heavy fermion systems under AC fields. We derive a periodic-Anderson-type generic effective model describing laser-irradiated heavy fermion systems with Floquet theory. Using this model, we discuss the nature of Kondo effect and topological phases under AC fields. We find that the behavior of Kondo effect depends on the lattice structure and, in most cases, we can realize the laser-induced magnetic phase transition via controlling Kondo effect with laser light. As for topological phases, we find that there appears a new phase of weak topological insulator which does not appear without laser light and circularly polarized laser light can induce a Weyl semimetal phase in heavy fermion systems.

In Chap. 4, we propose a new schemes to control insulating magnets with DC fields or slow AC fields. We derive the effective model of Mott insulators under DC electric fields and find that the spin-spin interaction strength in the direction parallel to the electric field are generically enhanced. Using this scheme, we propose the control of magnetic and topological orders in magnetic insulators. For this purpose, we demonstrate that several magnetic or topological ordered phases such as quantum spin liquids and Haldane-gap states can be induced if we apply a strong enough DC electric field to typical frustrated or low-dimensional magnets. Our proposal is effective especially for magnets in the vicinity of magnetic phase transition points, and would also be applicable for magnets under low-frequency AC electric fields such as terahertz laser pulses.

Finally, we conclude this thesis and explain our future outlook in Chap. 5.

Chapter 2

Laser-induced topological superconductivity in d-wave superconductors

2.1 Introduction

In this chapter, we explain our theoretical proposal for realizing topological superconductors (TSCs) with laser light [97]. TSCs have attracted a great deal of interest from the viewpoint of realization of Majorana fermions in solid states and a possible application to quantum computation [60, 98]. However, it is the current situation that experimental realization of TSCs is still limited. There are two main ways to search for topological superconductors. First one is to engineer a TSC in artificial systems by proximity effect (artificial TSCs). In recent studies, there are substantial developments in some artificial systems, such as a ferromagnetic atomic chain on a superconductor [99] or a nanowire on a superconductor [100]. In these artificial systems, the realization of TSCs is confirmed to a certain extent. Second way is to find a material which is intrinsically a TSC (intrinsic TSC). Some candidate materials of intrinsic TSCs have been proposed, for instance, a spin-triplet superconductor Sr_2RuO_4 [101] and a doped topological insulator $Cu_xBi_2Se_3$ [102–104]. However, nodal excitations in nearly gapless Sr_2RuO_4 [105, 106] are harmful for experimental detection of topological response, and topological nontriviality in $Cu_xBi_2Se_3$ is still under debate [107]. Therefore, further search of intrinsic TSCs is one of the important issues in the research field.

On the other hand, as explained in Chap. 1, tremendous developments have been achieved in the controls of topological phases with laser light [2, 43, 45, 49, 52, 108–110]. A typical example of the laser-induced topological state is a quantum Hall state in graphene [2, 43, 47]. This state is induced not by static magnetic field but by circularly polarized dynamical laser light. In this case, laser light effectively induces the next-nearest hopping with complex phase, which makes the system gapped, and thus the topologically non-trivial states similar to the Haldane model [51] are realized. This phenomenon is confirmed experimentally in graphene very recently [5]. In addition, a similar phenomenon is also observed on the surface of the laser-irradiated topological insulators by Tr-ARPES experiments [3]. The ARPES image obtained in the experiments shows that the surface Dirac cone becomes gapped when the laser light is applied to the system.

Motivated by these situations, we propose a possible way to realize TSCs with application of the laser light to well-known materials. We discover that the TSCs can be realized in d-wave superconductors, such as cuprate, fabricated on a substrate irradiated by circularly polarized

laser light. We consider a thin film of cuprate superconductors as a typical example of d-wave superconductors and apply Floquet theory to the theoretical model of cuprate superconductor and derive an effective model under the irradiation of the laser light. Based on this effective model, we reveal that the system acquires the topologically nontrivial nature, which is characterized by Chern numbers, and show that the laser-induced magnetic field in the effective model plays a crucial role in realizing TSCs.

This Chapter is organized as follows. In Sec. 2.2, we introduce our model and methods. Next we show the derivation of an effective model which describes laser-irradiated cuprate thin films in Sec. 2.3. In Sec. 2.4, we discuss topological properties of the effective model. We also show the topological phase diagram and clarify the nature of each phase. In Sec. 2.5, we discuss the experimental conditions to realize TSCs. Finally, the summary of this chapter is presented in Sec. 2.6.

2.2 Model and Methods

A setup of the system is schematically shown in Fig. 2.1. We consider a thin film of cuprate superconductors fabricated on a substrate. Because of the asymmetric potential due to the substrate, Rashba spin-orbit coupling appears. In order to describe such a situation, we introduce a Rashba-Hubbard model as

$$\begin{aligned}\mathcal{H} &= \sum_{\boldsymbol{k}\sigma} \xi(\boldsymbol{k}) c^\dagger_{\boldsymbol{k}\sigma} c_{\boldsymbol{k}\sigma} \\ &\quad + \sum_{\boldsymbol{k}\sigma\sigma'} (\alpha \boldsymbol{g}(\boldsymbol{k}) \cdot \boldsymbol{\sigma})_{\sigma\sigma'} c^\dagger_{\boldsymbol{k}\sigma} c_{\boldsymbol{k}\sigma'} + U \sum_i n_{i\uparrow} n_{i\downarrow},\end{aligned} \tag{2.1}$$

where

$$\xi(\boldsymbol{k}) = -2t(\cos k_x + \cos k_y) + 4t' \cos k_x \cos k_y - \mu, \tag{2.2}$$

$$\boldsymbol{g}(\boldsymbol{k}) = (-\sin k_y, \sin k_x, 0), \tag{2.3}$$

with $c_{\boldsymbol{k}\sigma}$ being the annihilation operator of electrons with momentum $\boldsymbol{k}$ and spin σ. We choose the form of $\xi(\boldsymbol{k})$, which includes the next-nearest neighbor hopping t', in order to reproduce the Fermi surface of typical high-T_c cuprates.

Next we consider the effect of laser light. We treat the laser light as time-dependent classical electromagnetic fields $\boldsymbol{A}(t)$ and introduce them as Peierls phases. This treatment is equivalent to substituting $\boldsymbol{k}$ with $\boldsymbol{k} - \boldsymbol{A}(t)$. With this substitution, we obtain the time-dependent model, which describes laser-illuminated cuprate thin films, as

$$\begin{aligned}\mathcal{H}(t) &= \sum_{\boldsymbol{k}\sigma} \xi(\boldsymbol{k} - \boldsymbol{A}(t)) c^\dagger_{\boldsymbol{k}\sigma} c_{\boldsymbol{k}\sigma} \\ &\quad + \sum_{\boldsymbol{k}\sigma\sigma'} (\alpha \boldsymbol{g}(\boldsymbol{k} - \boldsymbol{A}(t)) \cdot \boldsymbol{\sigma})_{\sigma\sigma'} c^\dagger_{\boldsymbol{k}\sigma} c_{\boldsymbol{k}\sigma'} + U \sum_i n_{i\uparrow} n_{i\downarrow}\end{aligned} \tag{2.4}$$

with $\boldsymbol{A}(t) = (A_x \cos \omega t, A_y \sin \omega t, 0)$, which corresponds to circularly ($A_x = A_y$) or elliptically ($A_x \neq A_y$) polarized laser light.

Generally speaking, it is difficult to solve time-dependent quantum many-body problems. However, as for time-periodic problems, we can analyze them with Floquet theory explained in Sec. 1.3. The model Hamiltonian (2.4) is periodic in time and therefore we can apply Floquet theory to it. As explained in Sec. 1.4, there appear nonequilibrium steady states, called Floquet prethermalized states, which have finite life time when the frequency is sufficiently high[83–85].

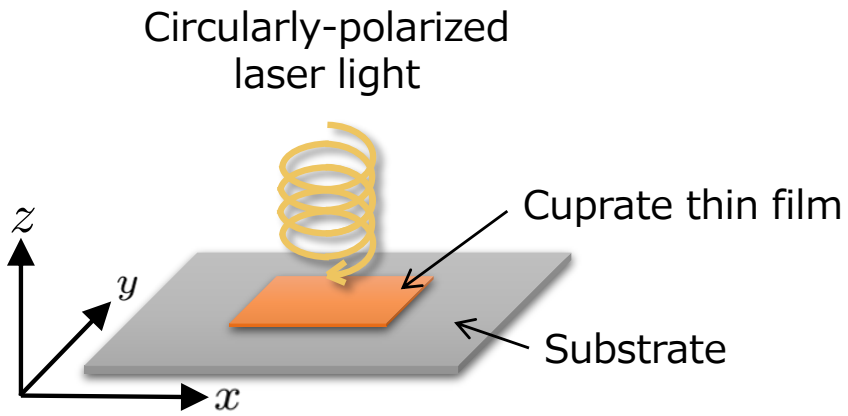

Figure 2.1: Schematic picture of the setup. A thin film of cuprate superconductors fabricated on a substrate is irradiated by circularly polarized laser light in the z-direction.

The nonequilibrium steady states are known to be described with an effective Hamiltonian in Floquet theory. Though it is difficult to directly calculate the effective Hamiltonian, there are useful methods to derive the effective Hamiltonian with a perturbative expansion [81]. For this purpose, we use the perturbative expansion eq. (1.7) shown in Sec. 1.4. For convenience, we write down the formula again as

$$\mathcal{H}_{\rm eff} = \mathcal{H}_0 + \sum_{n>0} \frac{[\mathcal{H}_n, \mathcal{H}_{-n}]}{n\omega} + \mathcal{O}\left(\omega^{-2}\right), \tag{2.5}$$

where $\mathcal{H}_n = \frac{1}{T}\int_{-T/2}^{T/2} dt \mathcal{H}(t) e^{-in\omega t}$. The second term in the case of the laser-irradiated systems represents the second order perturbation process of the n-photon absorption $\mathcal{H}_n$ and n-photon emission $\mathcal{H}_{-n}$ in off-resonant light. If the laser intensity is sufficiently small, it is reduced to virtual processes related to one-photon absorption $\mathcal{H}_1$ and emission $\mathcal{H}_{-1}$.

2.3 Derivation of the effective model

In this section, we calculate the effective Hamiltonian (3.7) up to the first order in $1/\omega$. The effective model describes the nonequilibrium steady states of the irradiated thin film of cuprate superconductors. The model is obtained as

$$\begin{aligned}
\mathcal{H}_{\rm eff} &= \mathcal{H}_0 + \sum_{n>0} \frac{[\mathcal{H}_n, \mathcal{H}_{-n}]}{n\omega} \\
&= \sum_{\boldsymbol{k}\sigma} \tilde{\xi}_0(\boldsymbol{k}) c^\dagger_{\boldsymbol{k}\sigma} c_{\boldsymbol{k}\sigma} \\
&+ \sum_{\boldsymbol{k}\sigma\sigma'} (\alpha \tilde{\boldsymbol{g}}_0(\boldsymbol{k}) \cdot \boldsymbol{\sigma})_{\sigma\sigma'} c^\dagger_{\boldsymbol{k}\sigma} c_{\boldsymbol{k}\sigma'} + U \sum_i n_{i\uparrow} n_{i\downarrow} \\
&- \sum_{\boldsymbol{k}\sigma\sigma'} \mu_B \tilde{H}(\boldsymbol{k}) \sigma_z c^\dagger_{\boldsymbol{k}\sigma} c_{\boldsymbol{k}\sigma'},
\end{aligned} \tag{2.6}$$

where

$$\tilde{\xi}_0(\boldsymbol{k}) = -2t(J_0(A_x)\cos k_x + J_0(A_y)\cos k_y) + 4t' J_0\left(\sqrt{A_x^2 + A_y^2}\right)\cos k_x \cos k_y - \mu, \tag{2.7}$$

$$\tilde{\boldsymbol{g}}_0(\boldsymbol{k}) = (-J_0(A_y)\sin k_y, J_0(A_x)\sin k_x, 0), \tag{2.8}$$

$$\tilde{H}(\boldsymbol{k}) = \frac{4\alpha^2 \mathcal{J}^2(A_x, A_y)}{\mu_B \omega}\cos k_x \cos k_y, \tag{2.9}$$

$$\mathcal{J}^2(A_x, A_y) = \sum_{m=0} \frac{(-1)^m J_{2m+1}(A_x) J_{2m+1}(A_y)}{2m+1}, \tag{2.10}$$

and $J_n(x)$ represents the n-th Bessel function. Note that the first three terms come from the zero-th Fourier component (i.e. the time average of the original time-dependent Hamiltonian) and the last term comes form the commutator part, which does not include the interaction term because the original Hubbard interaction term does not depend on time. We see two effects induced by the laser light. The first one is so-called "dynamical localization"[111]. With this effect, the hopping amplitude t, t' and the coupling constant α are renormalized by the 0-th Bessel function. This effect induces the deformation of Fermi surface, resulting in topological phase transitions as we mention below. The second one is "laser-induced magnetic field". It causes the Zeeman splitting of which splitting-width varies in momentum space. It plays a crucial role in realizing TSC in this system.

Next we consider the Bogoliubov-de Gennes (BdG) Hamiltonian which describes superconducting states. The order parameter of cuprate superconductors is known to be d-wave [112]. However, in our system, the Rahba spin-orbit coupling breaks the inversion symmetry and thus p-wave pairing may be admixed with d-wave pairing [113]. Therefore we investigate the D+p-wave superconducting state by adopting a simple form $\Delta(\boldsymbol{k}) = i[\psi(\boldsymbol{k}) + \boldsymbol{d}(\boldsymbol{k})\cdot\boldsymbol{\sigma}]\sigma_y$ with $\psi(\boldsymbol{k}) = \Delta_d(\cos k_x - \cos k_y)$ and $\boldsymbol{d}(\boldsymbol{k}) = \Delta_p(\sin k_y, \sin k_x, 0)$. We assume that $|\Delta_d|$ is much larger than $|\Delta_p|$. With the D+p wave superconducting order parameter and the BCS-type decoupling of the interaction term, we write down the BdG Hamiltonian as $\mathcal{H}_{\mathrm{BdG}} = 1/2\sum_{\boldsymbol{k}} \Psi_{\boldsymbol{k}}^\dagger \mathcal{H}(\boldsymbol{k})\Psi_{\boldsymbol{k}}$, where

$$\mathcal{H}(\boldsymbol{k}) = \begin{pmatrix} \mathcal{H}_N(\boldsymbol{k}) & \Delta(\boldsymbol{k}) \\ \Delta^\dagger(\boldsymbol{k}) & -\mathcal{H}_N^T(-\boldsymbol{k}) \end{pmatrix}, \tag{2.11}$$

$$\mathcal{H}_N(\boldsymbol{k}) = \tilde{\xi}_0(\boldsymbol{k})\sigma_0 + \alpha\tilde{g}_0(\boldsymbol{k})\cdot\boldsymbol{\sigma} - \mu_B\tilde{H}(\boldsymbol{k})\sigma_z, \tag{2.12}$$

and $\Psi_{\boldsymbol{k}}^\dagger = (c_{\boldsymbol{k}\uparrow}^\dagger, c_{\boldsymbol{k}\downarrow}^\dagger, c_{-\boldsymbol{k}\uparrow}, c_{-\boldsymbol{k}\downarrow})$. Without laser light ($A_x = A_y = 0$), this model represents the original $D + p$ wave superconductor and thus it has point nodes (shown in Fig. 2.2 (a)). With finite intensity of laser light ($A_x, A_y > 0$), the point nodes are gapped out (shown in Fig. 2.2 (b)). Later we show that the TSC is realized and the chiral Majorana edge modes appear in the laser-induced gap (shown in Fig. 2.3). This gap opening is caused by the laser-induced magnetic field (2.9). This term breaks the time-reversal symmetry and changes the symmetry class of the BdG Hamiltonian to class D.

Before closing this section, we remark on differences from the case of usual magnetic field applied to cuprate superconductors. When the orbital depairing effect is neglected, this case is described by the model similar to ours, which has already been studied by Yoshida and Yanase [114, 115]. However, there are two important differences from their studies. First, the laser-induced magnetic fields do not induce vortices in superconductors. Usual magnetic fields induce vortices and easily suppress the superconducting states. On the other hand, the synthetic magnetic field induced by the laser light leads to only the Zeeman-type energy splitting

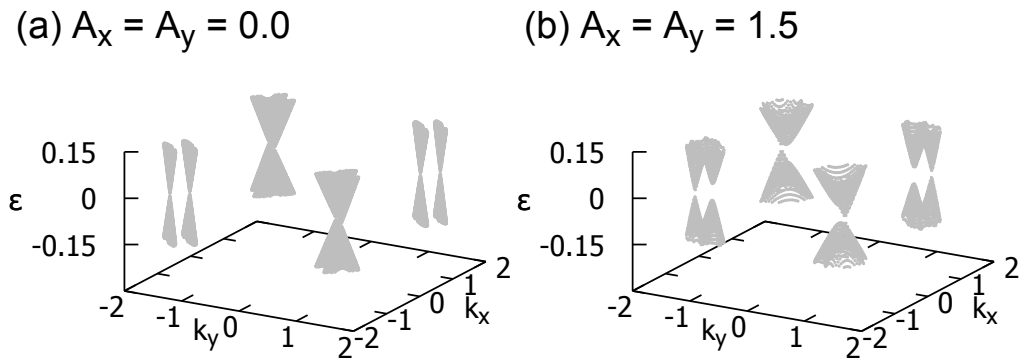

Figure 2.2: Quasi-particle spectrum of the effective model (a) without laser-irradiation and (b) with laser-irradiation. The data are obtained by diagonalizing the BdG Hamiltonian (2.11). We choose the parameters as $t = 1.0$, $t' = 0.2$, $\alpha = 0.3$, $\omega = 0.4$, $\Delta_d = 0.4$, and $\Delta_p = 0.08$.

(shown in Eq. (2.6)) and oscillating gauge fields do not induce the vortices in superconductors. This is an advantage in realizing the TSC. Second one is that the laser light induces hopping renormalization (dynamical localization). As we mention below, the structure of superconducting gap is modified by the dynamical localization, and thus the topological states, which cannot be stabilized by usual magnetic fields, are realized.

2.4 Topological phases

2.4.1 Chern number and Phase diagram

As we mentioned above, our BdG Hamiltonian belongs to the symmetry class D in two dimensions. Therefore, the gapped state of this model is specified by the Chern number C[116] , which is defined by

$$C = \frac{1}{2\pi i}\int d\boldsymbol{k}\epsilon^{ij}\sum_{n:\text{filled}}\partial_{k_i}\langle u_n(\boldsymbol{k})|\partial_{k_j}u_n(\boldsymbol{k})\rangle\,. \tag{2.13}$$

We calculate the Chern number by two methods. The first one is an analytical method, which is proposed by Daido and Yanase [115]. Their derivation can be straightforwardly applied to our model. The analytic form is obtained as

$$C = \sum_{(\pm,\boldsymbol{k}_0)}\frac{1}{2}\text{sgn}\left[\frac{(\hat{\boldsymbol{z}}\times\nabla_{\boldsymbol{k}}E_\pm)\cdot\nabla_{\boldsymbol{k}}(\psi\pm\boldsymbol{d}\cdot\hat{\boldsymbol{g}})}{\mu_B(\tilde{H}\hat{\boldsymbol{z}})\cdot(\hat{\boldsymbol{g}}\times\boldsymbol{d})/\alpha}\right]_{\boldsymbol{k}=\boldsymbol{k}_0}, \tag{2.14}$$

where $\hat{\boldsymbol{z}}$ is a unit vector in the z-direction, $E_\pm = \tilde{\xi}_0(\boldsymbol{k}) \pm \alpha|\tilde{\boldsymbol{g}}(\boldsymbol{k})|$ and $\hat{\boldsymbol{g}} = \tilde{\boldsymbol{g}}(\boldsymbol{k})/|\tilde{\boldsymbol{g}}(\boldsymbol{k})|$. The summation is taken over all the gapped nodes $\boldsymbol{k}_0$ on Fermi surfaces of the $E_\pm$ bands. The energy spectrum is written as [115]

$$\mathcal{E}_+ = \pm\sqrt{E_+^2 + |(\psi+\boldsymbol{d}\cdot\tilde{\boldsymbol{g}}) + i(\mu_B(\tilde{H}\hat{\boldsymbol{z}})\cdot(\hat{\boldsymbol{g}}\times\boldsymbol{d})/\alpha|\tilde{\boldsymbol{g}}|)|^2}, \tag{2.15}$$

$$\mathcal{E}_- = \pm\sqrt{E_-^2 + |(\psi-\boldsymbol{d}\cdot\tilde{\boldsymbol{g}}) + i(\mu_B(\tilde{H}\hat{\boldsymbol{z}})\cdot(\hat{\boldsymbol{g}}\times\boldsymbol{d})/\alpha|\tilde{\boldsymbol{g}}|)|^2}. \tag{2.16}$$

Therefore, the gap nodes appear in the absence of the layer light at $\boldsymbol{k}_0$ satisfying

$$E_\pm(\boldsymbol{k}_0) = \psi(\boldsymbol{k}_0) \pm \boldsymbol{d}(\boldsymbol{k}_0)\cdot\tilde{\boldsymbol{g}}(\boldsymbol{k}_0) = 0. \tag{2.17}$$

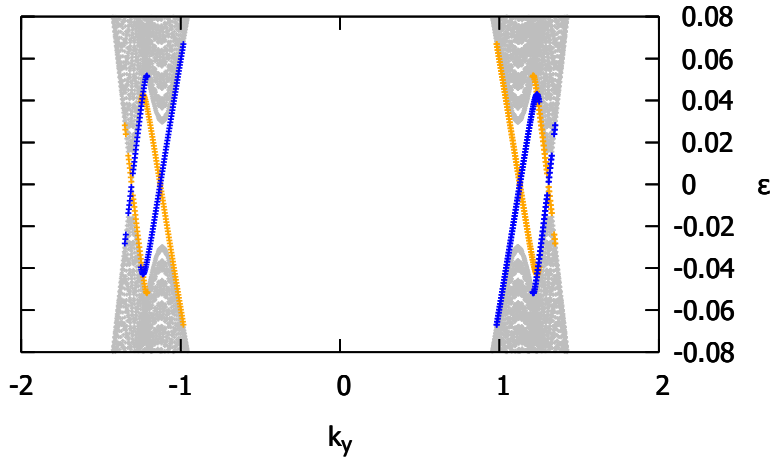

Figure 2.3: Energy spectra in a ribbon-shaped system with open boundary conditions along the x-axis and periodic boundary conditions along the y-axis. The orange dots and blue dots show the Majorana mode localized at each side of edges, respectively. Four edge modes appear at each edge, corresponding to the Chern number $C = -4$. We choose the parameters as $t = 1.0$, $t' = 0.2$, $\alpha = 0.3$, $\omega = 0.4$, $\Delta_d = 0.4$, and $\Delta_p = 0.08$. The filling n is 0.8 ($n = 1$ represents half-filling).

The gapped nodes at $\boldsymbol{k}_0$ are intersections of a Fermi surface $E_\pm(\boldsymbol{k}) = 0$ and zeros of order parameter $\psi(\boldsymbol{k}) \pm \boldsymbol{d}(\boldsymbol{k}) \cdot \boldsymbol{g}(\tilde{\boldsymbol{k}}) = 0$.

Based on the analytic formula (2.14), we can evaluate the Chern number with counting the contribution from gapped nodes. Each gapped node gives a contribution $+1/2$ or $-1/2$. Sign of each contribution can be estimated as follows. First we define the direction parallel to the Fermi surface of $E_\pm(\boldsymbol{k})$ bands as $\hat{k}_\pm = \hat{\boldsymbol{z}} \times \nabla_{\boldsymbol{k}} E_\pm / |\hat{\boldsymbol{z}} \times \nabla_{\boldsymbol{k}} E_\pm|$. Next we check the change of the sign of $\psi \pm \boldsymbol{d} \cdot \hat{\boldsymbol{g}} / (\mu_B (\tilde{H}\hat{\boldsymbol{z}}) \cdot (\hat{\boldsymbol{g}} \times \boldsymbol{d})/\alpha)$, which is in the argument of the function of Eq. (2.14). When it changes from negative to positive along $\hat{k}_\pm$ direction at gapped nodes, the contribution is $+1/2$, and vice versa. Summing up all the contributions, we obtain the Chern number of the total bands.

This analytic formula is very useful for understanding the origin of the Chern number. However, it is not convenient for systematic calculations in a broad range of parameters. Therefore, for systematic calculation in a broad range of parameters, we use another method to calculate the Chern number. This is called Fukui-Hatsugai-Suzuki method [117], which is an efficient numerical method to calculate the Chern number of the model defined on discretized momentum space. With this approach, we calculate the Chern number for each (A_x, A_y) point and obtain the topological phase diagram which is shown in Fig. 2.4. In the phase diagram, the number of electrons is fixed by tuning the chemical potential μ. In some regions, the Chern number is finite, implying the TSCs. In the following subsections, Secs. IVB and IVC, we clarify the nature of the superconducting phases in the low intensity region ($A_x, A_y \lesssim 1.5$) and in the high intensity region ($A_x, A_y \gtrsim 1.5$), respectively.

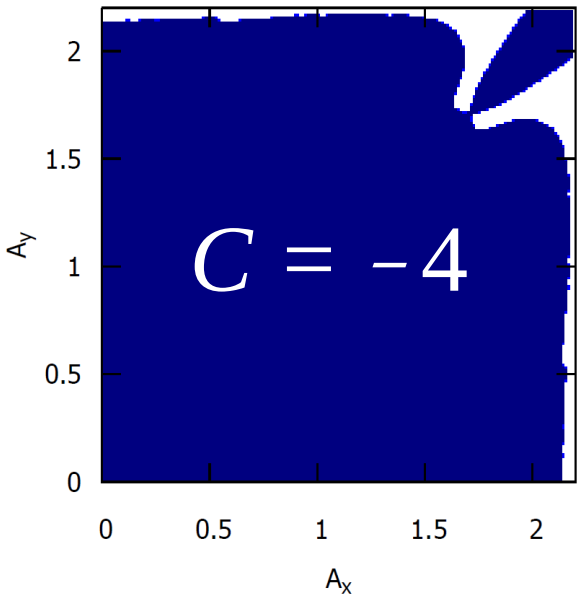

Figure 2.4: Topological phase diagram of the laser-irradiated superconducting cuprate thin films. Color plot shows numerically calculated Chern numbers for each (A_x, A_y) point. The white region shows a topologically trivial phase ($C = 0$) and the blue region corresponds to a topologically nontrivial phases ($C = -4$). We choose the parameters as $t = 1.0$, $t' = 0.2$, $\alpha = 0.3$, $\omega = 36.0$, $\Delta_d = 0.05$, and $\Delta_p = 0.01$.

2.4.2 Weak intensity region

In the weak intensity region, we find that a TSC specified by $C = -4$ is realized in a broad range of parameters. Even with infinitesimally weak intensity of laser light, the TSC is realized in our model, and thus it is possible to experimentally realize TSCs with relatively weak laser light. This is one of the main results of this study. The energy spectrum of the ribbon-shaped system is shown in Fig. 2.3. As expected from the bulk-edge correspondence, four chiral Majorana modes appear near the edge of the system. The number of chiral Majorana modes corresponds to the Chern number $C = -4$.

The reason why the $C = -4$ phase is realized is understood with the analytic formula (2.14). As we mentioned above, the Chern number is determined by the gapped nodes, which are defined as intersections of a Fermi surface and zeros of order parameters (they are shown in Fig. 2.5). Dividing the contributions from two Fermi surfaces of the $E_+(\boldsymbol{k}) = 0$ and $E_-(\boldsymbol{k}) = 0$ bands, we write as $C = C_+ + C_-$.

We here evaluate $C_\pm$. In the case of circularly polarized laser ($A_x = A_y$), all of the four nodes on each Fermi surface are crystallographically equivalent since they are transformed by the four-fold rotation. Therefore, they give the same contributions [115] and thus $C_\pm$ must be either 2 or -2. Moreover, the superconducting gaps of each Fermi surface can be adiabatically deformed to each other without closing the gap, and thus the contributions to the Chern number is equivalent. Therefore $C_+ = C_-$ and we conclude that the Chern number is either 4 or -4. With the procedure mentioned in Sec. 2.4.1, we find that the $C = -4$ phase is realized. In the case of elliptically polarized laser($A_x \neq A_y$), the superconducting gap can be adiabatically deformed to that in the case of circularly polarized laser, and thus the Chern number is not changed. Indeed, the $C = -4$ phase is realized in a broad parameter range of the laser light as

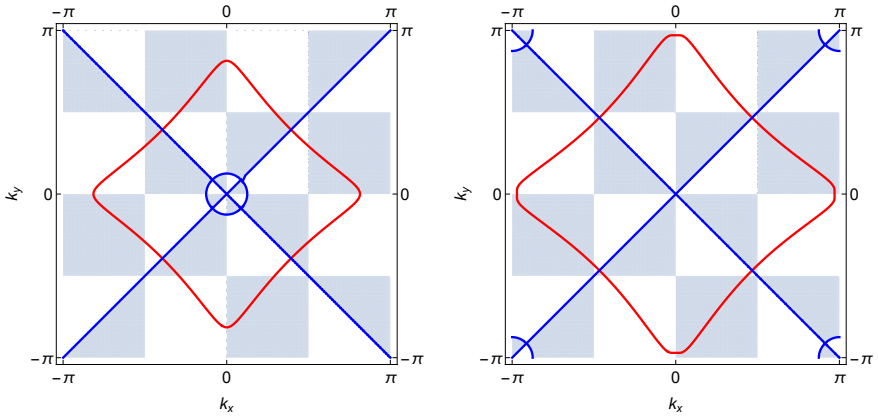

Figure 2.5: Fermi surfaces (red lines) and zeros of superconducting gap (blue lines) with weak intensity of laser light $(A_x, A_y) = (0.1, 0.1)$. The $E_+(\boldsymbol{k})$ band is shown in the left panel and the $E_-(\boldsymbol{k})$ band is shown in the right panel. The shaded region represents $(\psi \pm \boldsymbol{d}\cdot\hat{\boldsymbol{g}})/(\mu_B(\tilde{H}\hat{\boldsymbol{z}})\cdot(\hat{\boldsymbol{g}}\times\boldsymbol{d})/\alpha) < 0$. We use the same parameters as in the phase diagram, Fig.4 .

shown in Fig. 2.4.

At the end of this subsection, we discuss the effect of laser light on the superconducting order parameter. Though the superconducting order parameter is assumed to be $D + p$ wave in this study, the nature of the superconducting order can be changed by laser light through two effects, the paramagnetic effect and the deformation of the Fermi surface. However, the laser-induced magnetic field is very small and its effect on the superconducting order parameter is negligible. In the weak intensity region, deformation of Fermi surface is also small. Therefore the assumption of the $D + p$-wave superconducting order is valid in this region.

2.4.3 Strong intensity region

Even with strong intensity of laser light, the system shows the topologically non-trivial phase with $C = -4$. Furthermore, under elliptic light $(A_x \neq A_y)$, different topological phases, such as $C = 0, 2$ and -2 are realized (The phases of $C = 2$ and -2 appear out of the region of Fig. 2.4). For example, the phase with $C = -2$ appear in a finite region around the point $(A_x, A_y) = (2.8, 2.1)$, which is shown in Fig. 2.6(b). The appearance of $C = 0, 2$ and -2 reflects the fact that the rotation symmetry of the superconducting gap is reduced from four-fold to two-fold under the elliptic light.

The reason why these non-trivial Chern numbers are realized can also be understood with the analytic formula (2.14). Among them, we explain the phase of $C = 0$ and $C = -2$. In Figs. 2.6 (a) and 2.6 (c), we show the case of $C = 0$. We can see that the symmetry of superconducting gap is reduced due to the elliptic laser light, but the system still has two-fold rotational symmetry. By this symmetry, $C_\pm$ is restricted to $2, 0$ or -2. As we mentioned above, the sign of each contribution can be estimated from the sign of $\psi \pm \boldsymbol{d}\cdot\hat{\boldsymbol{g}}/(\mu_B(\tilde{H}\hat{\boldsymbol{z}})\cdot(\hat{\boldsymbol{g}}\times\boldsymbol{d})/\alpha)$, which is shown in Fig. 2.6 (a) by shading. The change of the sign is opposite between the $E_+(\boldsymbol{k})$ band and $E_-(\boldsymbol{k})$ band. Therefore C_+ and C_- have opposite signs and thus $C = 0$. It is a topologically trivial state, which can be realized by strong laser irradiation.

Next we discuss the $C = -2$ phase in Fig. 2.6 (b). The figure shows twelve nodes (four nodes in the left panel and eight nodes in the right panel). Due to two-fold rotational symmetry,

C_+ is limited to $2, 0$ or -2 and C_- must be $4, 0$ or -4. Estimating the contribution from each node, we obtain $C_+ = -2$ and $C_- = 0$ and thus the Chern number C is equal to -2. Owing to numerical difficulties, the global phase diagram including the phases of $C = 2$ and -2 is not shown. However, we have confirmed that the phases of $C = 2$ and -2 appear in a finite region of the phase diagram as we mentioned above.

This strong intensity region includes the regime where the effective value of the hopping t or t' is renormalized to zero. In the case that the effective value of t is equal to zero, there is only the next nearest neighbor hopping t'. For example, such a situation is realized at $(A_x, A_y) = (2.4, 0.3)$, where the nearest neighbor hopping t in the x-direction is almost completely suppressed. The structure of the Fermi surfaces and the superconducting gap are shown in Fig. 2.6(d). In this case, a quasi-one-dimensional band dispersion is achieved and it corresponds to a topologically trivial state ($C = 0$). Due to the nesting structure of the Fermi surfaces, a spin density wave order may be favored.

Finally, we remark on the effects of strong laser light on the superconducting order. As we mentioned at the end of Sec. 2.4, there are two laser-induced effects, paramagnetic effect and deformation of Fermi surfaces. Even in the strong intensity region, laser-induced magnetic field is still small for cuprates. However, the Fermi surfaces are drastically deformed and thus it is possible that the superconducting order is modified. However, the present system is very likely to remain topologically-nontrivial as long as the nodal spin-singlet component is dominant[115]. Therefore, we expect TSCs even when the superconducting gap is more or less deformed from the original $D + p$-wave one.

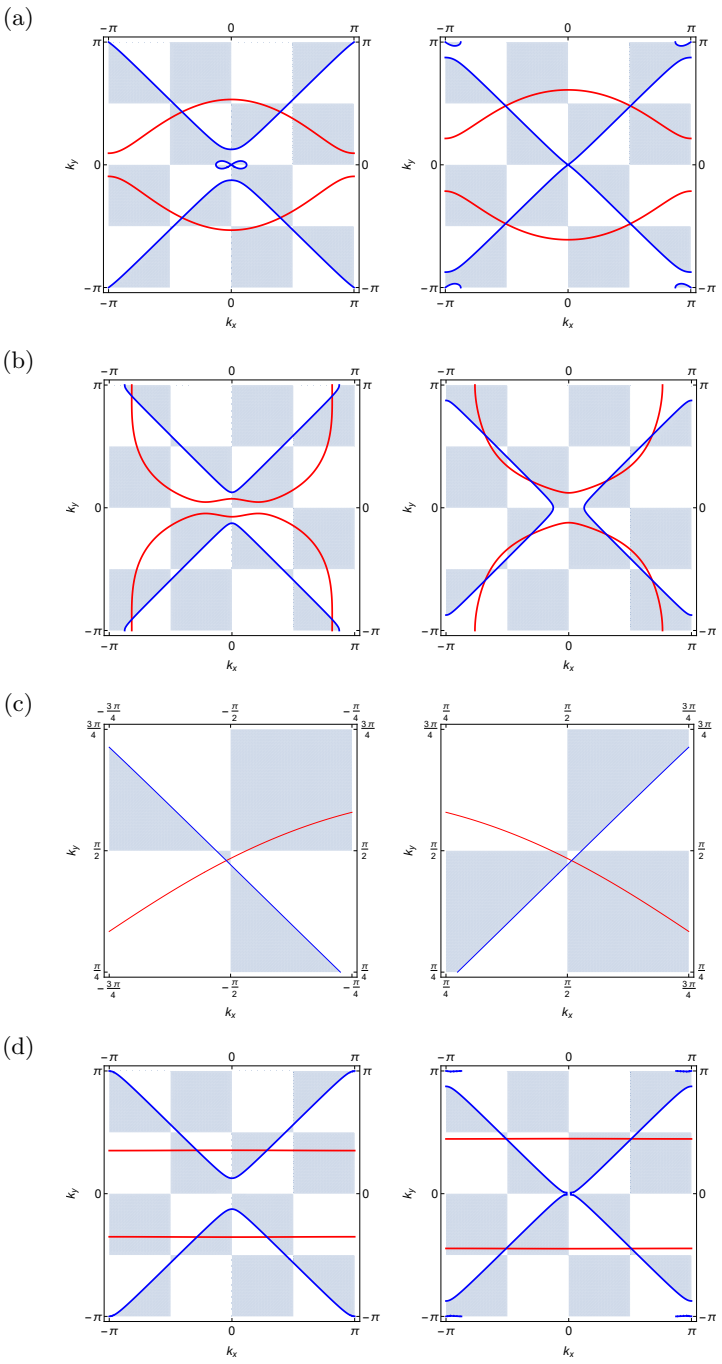

Figure 2.6: (a, b) Fermi surfaces (red lines) and zeros of superconducting gap (blue lines) with strong intensity of laser light (a, c) $(A_x, A_y) = (2.1, 1.8)$, (b) $(A_x, A_y) = (2.8, 2.1)$, and (d) $(A_x, A_y) = (2.4, 0.3)$. The $E_+(\boldsymbol{k})$ band is shown in the left panel and the $E_-(\boldsymbol{k})$ band is shown in the right panel. The shaded region represents $(\psi \pm \boldsymbol{d} \cdot \hat{\boldsymbol{g}})/(\mu_B(\tilde{H}\hat{\boldsymbol{z}}) \cdot (\hat{\boldsymbol{g}} \times \boldsymbol{d})/\alpha) < 0$. We use the same parameters as in the phase diagram, Fig.4. (c) Enlarged figures of the right panel of Fig. (6.a). The detail of the structure near the gapped nodal points is shown.

2.5 Experimental setup

Our proposal has two advantages in experimentally realizing TSCs. First one is that the topologically-non trivial states can be realized by infinitesimal intensity of laser light in our model as we mentioned above. Indeed, any fine tuning of parameters is not required for TSCs. Second one is that the laser-induced magnetic field gives rise to only the Zeeman effect (paramagnetic effect) and thus does not induce vortices. Because of these advantages, a laser-irradiated cuprate thin film is a promising candidate for TSCs. In the following, we discuss the experimental conditions about materials and laser light as well as experimental methods.

Concerning candidate materials, a cuprate superconductor has advantages since its superconducting state is expected to be robust to the perturbations of laser light due to its high critical temperature. With a slight modification (e.g. the form of $\xi(\boldsymbol{k})$), our calculation can be applied to any d-wave superconductors with Rashba spin-orbit coupling. Thus some of the heavy fermion superconductors, such as $CeCoIn_5$ [118], are also a candidate material for laser-induced topological superconductors.

In our model, the laser light is characterized by its frequency and intensity. Strictly speaking, the frequency must be sufficiently high and off-resonant since our calculation is based on the high-frequency expansion. Within the scope of our calculation, frequency must be higher than the band width $8t$. In solid state systems, there are so many unoccupied bands above Fermi energy, then should choose an appropriate frequency so as to make it off-resonant. On the other hand, if the frequency is small, the effective Hamiltonian is modified by the higher order terms in $1/\omega$ [1]. However, we expect that the topological signatures of the effective Hamiltonian may remain. For example, even by the low frequency laser light, a nodal point of Dirac cone is gapped out [3], which is the behavior similar to the case of the off-resonant driving. Furthermore, it is reported that TSCs universally appear in noncentrosymmetric systems without time-reversal symmetry [115], in which our model is included.

Regarding the intensity of the laser light, the topological superconducting gap is opened by infinitesimal intensity. However weak-intensity laser opens only a small gap, which must be larger than the energy scale of thermal excitations in order to detect it experimentally. Thus there exists the minimum value of the required intensity to observe the TSC. Here we estimate the minimum intensity from the formula which stands for the size of the energy gap (derived from eqs. (2.15) and (2.16))

$$\left| \frac{\mu_B(\tilde{H}(\boldsymbol{k})\hat{\boldsymbol{z}}) \cdot (\hat{\boldsymbol{g}}(\boldsymbol{k}) \times \boldsymbol{d}(\boldsymbol{k}))}{\alpha \tilde{\boldsymbol{g}}(\boldsymbol{k})} \right|_{\boldsymbol{k}=\boldsymbol{k}_0} \sim \frac{4\alpha^2}{\omega} \frac{\Delta_p}{\tilde{\alpha}} J_1(A_x) J_1(A_y), \tag{2.18}$$

where the renormalized coupling constant is $\tilde{\alpha} = (J_0(A_x)^2 + J_0(A_y)^2)^{1/2}\alpha$. The amplitude of admixed p-wave component Δ_p is estimated as $\Delta_p \sim \Delta_d \tilde{\alpha}/E_F$ [119, 120]. When $\alpha = 0.1\text{eV}$, $\omega = 10\text{eV}$ and $\Delta_d/E_F = 0.1$ are adopted, in order to make the superconducting gap $0.1\text{meV} \sim 1\text{K}$, we need $A_x = A_y = 1.21$, which corresponds to the electric field amplitude $E \sim 600\text{MV/cm}$. It is the minimum amplitude to observe TSC in the experiments at temperature $\mathcal{T} \sim 1\text{K}$. At lower temperature than 1K, we can observe TSC with lower amplitude of laser light. Moreover, the formula (2.18) implies the condition for the optimal laser intensity corresponding to the maximum energy gap because the energy gap depends on the 1-st Bessel function $J_1(x)$ which takes a maximum value(~ 0.58) at $x \sim 1.84$. This amplitude of the vector potential $A \sim 1.84$ corresponds to the electric field amplitude $E \sim 1\text{GV/cm}$. With this intensity, the energy gap

[1] For example, the 2nd order term $1/\omega^2$ gives two effects. One is the modification of the parameters of the effective Hamiltonian which have already appeared in the 1st order. Second is the creation of new interaction terms which do not conserve the spins.

is estimated as 0.4meV. In order to realize a large gap, we should prepare a system which has large α and apply laser with intermediate frequency as long as the high-frequency expansion is appropriate and the off-resonant condition is satisfied.

To experimentally probe the phenomena proposed here, we need to use a method suitable for observing transient phenomena because we may use pulse laser in order to obtain strong intensity of laser light. Then the TSC is realized only when laser light is applied. As for the protocol of the application of laser light, we need to consider two conditions.(i) Too long laser pulse leads the interacting systems to infinite temperature trivial states [82], and thus we have to choose a short laser pulse. In other words, we have to quit the driving before the system heats up [83]. (ii) It takes time to reach the states described by the effective Hamiltonian. Moreover, to realize the ground states of the effective Hamiltonian we have to switch on the driving adiabatically [44, 121]. Therefore we should use a long and slowly developing pulse. Considering these two conditions, we choose intermediate time scale adequately to realize TSC. The important point for our proposal is that such an intermediate time scale should exist. Regarding the first condition, we can make the time for heating up longer by using higher frequency of laser light [84] or contriving the substrate to release the energy in the system. With respect to the second condition, although it is difficult to estimate the time scale, such a relaxation can happen in the femtosecond time scale [122]. Therefore, we can choose some appropriate time scale longer than the femtosecond scale and shorter than the time for heating up to observe TSC.

Finally, the most promising experimental tool to detect TSC is Tr-ARPES. The nodal structure of cuprate superconductors has been already observed in ARPES experiments[123]. Therefore, we believe that the gap-opening at the nodes will be detected with Tr-ARPES.

2.6 Summary of this chapter

In this chapter, we have suggested a possible way to realize TSCs with application of laser light to thin films of d-wave superconductors, e.g. cuprate thin films [124, 125]. Using Floquet theory, we have analyzed the model of laser-irradiated d-wave superconductors with a Rashba-type spin-orbit coupling. We have derived an effective model and discussed its topological nature. The effective model includes the laser-induced magnetic fields, which make the system fully gapped and lead the system to the topologically non-trivial states characterized by Chern numbers. The laser-induced magnetic fields do not create vortices in the superconductors, and thus our proposal has an advantage in experimentally realizing TSCs.

Chapter 3

Heavy fermion systems under AC electric fields

3.1 Introduction

In this chapter, we discuss dynamical controls of heavy fermion systems with AC electric fields (laser light). Heavy fermion systems are a typical example of the strongly correlated electron systems [126]. Here, the interplay of conduction electrons and localized electrons induces the Kondo effect and the RKKY interaction and their competiton provides rich phase diagrams including various quantum phases. Moreover, perturbations to the system, e.g. pressure, possibly drive the quantum phase transitions, which are indeed observed in various materials. In addition, recent studies have revealed that there also appear topological phases, e.g. topological Kondo insulators [127, 128], in the phase diagrams of heavy fermion systems. Therefore, heavy fermion systems are considered to be a desirable platform for studying various quantum phases in strongly correlated electron systems and the transitions among them.

To clarify how this rich structure of quantum phases is changed with AC electric fields out of equilibrium, we study laser-irradiated heavy fermion systems [129, 130]. To be specific, we theoretically investigate the periodic Anderson model with electric fields. The schematic picture of the setup is shown in Fig. 4.1. The periodic Anderson model is a simple model of heavy fermion systems. Using Floquet theory and slave boson approach, we derive a general effective model which describes the laser-irradiated heavy fermion systems. We show that there are two laser-induced effects in this model. One is dynamical localization [111], which suppresses hopping and hybridization. The other is laser-induced hopping and hybridization. These effects change the properties of the original heavy fermion systems. The first effect, dynamical localization, modifies the behavior of the Kondo effect. Especially, we point out that the Kondo effect can be enhanced or suppressed by laser light depending on the spatial structures of hybridization. The second effect, laser-induced hopping and hybridization, drives topological phase transitions. In three dimensional topological Kondo insulators, linearly polarized laser light induces a phase transition between trivial, weak topological, and strong topological Kondo insulators. Furthermore, with circularly polarized laser light, the system realizes strongly correlated Weyl semimetals. We provide a first step for revealing the basic properties of laser-irradiated heavy fermion systems and for controlling their properties by strong laser light.

This chapter is organized as follows. In Sec. 3.2, we introduce the periodic Anderson model and two theoretical methods. The first method is slave boson technique to treat the interaction effect. The second method is Floquet theory which is known as a versatile tool for time-periodic quantum systems. In Sec. 3.3, we discuss our main results. We derive a genric effective model

that describes laser-irradiated Kondo insulators and show that there are two effects induced by laser light. To demonstrate how these effects change the nature of the original systems, we discuss the impact of them on the Kondo effect in Sec. 3.4. We then discuss how the laser-induced effects change the topological properties of the original systems in Sec. 3.5. We show that these effects lead to topological phase transitions. Furthermore, we discuss experimental setups to confirm our results in Sec. 3.6. Finally, we summarize our results in Sec. 3.7.

3.2 Setup and Model

3.2.1 Periodic Anderson model with slave boson approach

In order to study the effect of laser light on heavy fermion systems, we introduce a theoretical model, which is a variant of the periodic Anderson model. The model Hamiltonian reads

$$\begin{aligned}\mathcal{H} = &\sum_{ij\sigma}\{t_{c,ij} - \mu\delta_{ij}\}c^\dagger_{i\sigma}c_{j\sigma} + \sum_{ij\sigma}\{t_{f,ij} + (\epsilon_f - \mu)\delta_{ij}\}f^\dagger_{i\sigma}f_{j\sigma} \\ &+ \sum_{ij\sigma\sigma'}\{V_{ij\sigma\sigma'}c^\dagger_{i\sigma}f_{j\sigma'} + \text{h.c.}\} + U\sum_i n^{(f)}_{i\uparrow}n^{(f)}_{i\downarrow},\end{aligned} \tag{3.1}$$

with $t_{c,ii} = t_{f,ii} = 0$, $t_{c,ij} = (t_{c,ji})^*$ and $t_{f,ij} = (t_{f,ji})^*$. We assume $t_{f,ij} \ll t_{c,ij}$. $\sigma, \sigma'(=\uparrow,\downarrow)$ stand for the (pseudo)spin. This model consists of conduction electrons specified by the annihilation (creation) operator $c_{i\sigma}$ ($c^\dagger_{i\sigma}$) and almost localized f-electrons specified by $f_{i\sigma}$ ($f^\dagger_{i\sigma}$). The term including $V_{ij\sigma\sigma'}$ represents the hybridization of the conduction and localized f-electrons. Due to the localized orbit of f-electrons, the electron correlation among f-electrons is strong, and thus we introduce a Hubbard-type interaction for them, as shown in the last term of the Hamiltonian (3.1). $n^{(f)}_{i\sigma}$ represents the number operator of the f-orbit at the i-th site and the definition is $n^{(f)}_{i\sigma} = f^\dagger_{i\sigma}f_{i\sigma}$.

To incorporate the correlation effect among f-electrons, we use a slave-boson mean field treatment [131–134]. It assumes a renormalized band structure, which results in the mean-field Hamiltonian,

$$\begin{aligned}\mathcal{H}_{\text{MF}} = &\sum_{ij\sigma}\{t_{c,ij} - \mu\delta_{ij}\}c^\dagger_{i\sigma}c_{j\sigma} \\ &+ \sum_{ij\sigma}\{|b|^2 t_{f,ij} + (\epsilon_f + \lambda - \mu)\delta_{ij}\}f^\dagger_{i\sigma}f_{j\sigma} \\ &+ \sum_{ij\sigma\sigma'}\{b^* V_{ij\sigma\sigma'}c^\dagger_{i\sigma}f_{j\sigma'} + \text{h.c.}\},\end{aligned} \tag{3.2}$$

where b is a renormalization factor and λ represents an energy shift of f-orbital level by the interaction effect.

In this study, we numerically solve self-consistent equations for b and λ and determine their values for each temperature. We show the derivation of the self-consistent equations in

Appendix. A. The explicit form of the equations is

$$\lambda = \frac{1}{N}\sum_{i\neq j\sigma} t_{f,ij}\langle f^\dagger_{i\sigma} f_{j\sigma}\rangle + \frac{1}{Nb^*}\sum_{ij\sigma\sigma'} V^*_{ji\sigma'\sigma}\langle f^\dagger_{i\sigma} c_{j\sigma'}\rangle, \tag{3.3}$$

$$|b|^2 = 1 - \frac{1}{N}\sum_{i\sigma}\langle f^\dagger_{i\sigma} f_{i\sigma}\rangle, \tag{3.4}$$

where N is the number of sites and $\langle\cdots\rangle$ stands for a thermal average with the mean-field Lagrangian $\mathcal{L}_{\rm MF}$ (The definition is presented in Appendix A). Since we consider insulating systems in this study, we solve simultaneously the equations (3.3), (3.4) and the condition of half-filling,

$$n_{\rm fill} = \frac{1}{N}\sum_{i\sigma}\Big(\langle c^\dagger_{i\sigma} c_{i\sigma}\rangle + \langle f^\dagger_{i\sigma} f_{i\sigma}\rangle\Big) = 2, \tag{3.5}$$

and determine the chemical potential μ for each temperature. Since there are two types of electrons (c and f) and two (pseudo) spins ($\uparrow$ and $\downarrow$) for each sites, $n_{\rm fill} = 2$ corresponds to half-filling.

3.2.2 Floquet theory

Next we consider the effect of laser light. For this purpose, we first consider a time-dependent model which describes laser-illuminated heavy fermion systems. We treat laser light as oscillating electric fields, and thus introduce a Peierls phase. We obtain the time-dependent model from (3.2) as

$$\begin{aligned}\mathcal{H}(t) = &\sum_{ij\sigma}\{e^{i\boldsymbol{A}(t)\cdot\boldsymbol{r}_{ij}} t_{c,ij} - \mu\delta_{ij}\} c^\dagger_{i\sigma} c_{j\sigma} \\ &+ \sum_{ij\sigma}\{e^{i\boldsymbol{A}(t)\cdot\boldsymbol{r}_{ij}}|b|^2 t_{f,ij} + (\epsilon_f + \lambda - \mu)\delta_{ij}\} f^\dagger_{i\sigma} f_{j\sigma} \\ &+ \sum_{ij\sigma\sigma'}\{e^{i\boldsymbol{A}(t)\cdot\boldsymbol{r}_{ij}} b^* V_{ij\sigma\sigma'} c^\dagger_{i\sigma} f_{j\sigma'} + \text{h.c.}\},\end{aligned} \tag{3.6}$$

where $\boldsymbol{A}(t) = A\cos\theta_A\cos\omega t\boldsymbol{e}_x + A\sin\theta_A\cos(\omega t - \varphi)\boldsymbol{e}_y$, $\boldsymbol{e}_x = (1,0,0)$, $\boldsymbol{e}_y = (0,1,0)$, and φ is the polarization angle of the laser light. In general, it is difficult to solve a time-dependent quantum many-body problem. However, in the case of time-periodic problem, we can use a useful description with Floquet theory as explained in Sec. 1.4. The model Hamiltonian (3.6) is time-periodic and thus we can apply Floquet theory. As explained in Sec. 1.4, there appear nonequilibrium steady states, called Floquet prethermalized states, which have finite life time when the frequency is sufficiently high [83–85]. The nonequilibrium steady states are known to be described with an effective Hamiltonian in Floquet theory. Though it is difficult to directly calculate the effective Hamiltonian, there are useful methods to derive the effective Hamiltonian with a perturbative expansion [81]. For this purpose, we use the perturbative

expansion eq. (1.7) shown in Sec. 1.4. For convenience, we write down the formula again [1] as

$$\mathcal{H}_{\rm eff} = \mathcal{H}_0 + \mathcal{H}_{\rm com} + \mathcal{O}\left(\omega^{-2}\right), \tag{3.7}$$

$$\mathcal{H}_0 = \mathcal{H}^{(0)}, \tag{3.8}$$

$$\mathcal{H}_{\rm com} = \sum_{n>0} \frac{[\mathcal{H}^{(+n)}, \mathcal{H}^{(-n)}]}{n\omega}, \tag{3.9}$$

where $\mathcal{H}^{(n)} = \frac{1}{\mathcal{T}} \int_{-\mathcal{T}/2}^{\mathcal{T}/2} dt \mathcal{H}(t) e^{-in\omega t}$ with $\mathcal{T} = 2\pi/\omega$. The first term $\mathcal{H}_0$ is the time-average of the original time-dependent Hamiltonian (3.6). The second term $\mathcal{H}_{\rm com}$ represents the second order perturbation process of the n-photon absorption $\mathcal{H}^{(+n)}$ and n-photon emission $\mathcal{H}^{(-n)}$ in off-resonant light.

3.3 Effective Hamiltonian

In this section, we derive an effective model of heavy fermion systems irradiated by the laser light $\boldsymbol{A}(t)$ and show the laser-induced effects which are found in our effective model. First we calculate the n-th Fourier component of the time-dependent Hamiltonian (3.6). For this purpose, we introduce parameters $\rho_{ij} > 0$ and $\theta_A \in [0, 2\pi)$ as

$$\rho_{ij}(\theta_A) e^{i\phi_{ij}(\theta_A)} := \cos\theta_A \boldsymbol{e}_x \cdot \boldsymbol{r}_{ij} + \sin\theta_A e^{-i\varphi} \boldsymbol{e}_y \cdot \boldsymbol{r}_{ij}, \tag{3.10}$$

and use the Jacobi-Anger expansion

$$e^{iz\cos\theta} = \sum_{n=-\infty}^{\infty} i^n J_n(z) e^{in\theta}, \tag{3.11}$$

where $J_n(z)$ represents the n-th Bessel function. Then we obtain the n-th Fourier component $\mathcal{H}^{(n)}$ as

$$\begin{aligned}
\mathcal{H}^{(n)} = & \sum_{ij\sigma} \{\mathcal{J}_{ij}^{(n)}(A, \theta_A) t_{c,ij} - \mu\delta_{ij}\delta_{n0}\} c_{i\sigma}^\dagger c_{j\sigma} \\
& + \sum_{ij\sigma} \{\mathcal{J}_{ij}^{(n)}(A, \theta_A) |b|^2 t_{f,ij} + (\epsilon_f + \lambda - \mu)\delta_{ij}\delta_{n0}\} f_{i\sigma}^\dagger f_{j\sigma} \\
& + \sum_{ij\sigma\sigma'} \{\mathcal{J}_{ij}^{(n)}(A, \theta_A) b^* V_{ij\sigma\sigma'} c_{i\sigma}^\dagger f_{j\sigma'} \\
& \qquad + \mathcal{J}_{ij}^{(n)}(A, \theta_A) b V_{ji\sigma'\sigma}^* f_{i\sigma}^\dagger c_{j\sigma'}\},
\end{aligned} \tag{3.12}$$

with $\mathcal{J}_{ij}^{(n)}(A, \theta_A) = i^n J_n(A\rho_{ij}(\theta_A)) e^{in\phi_{ij}(\theta_A)}$. We apply this result to the formula (3.7) and then obtain the explicit form of the effective Hamiltonian as

$$\mathcal{H}_{\rm eff} = \mathcal{H}_0 + \mathcal{H}_{\rm com}, \tag{3.13}$$

$$\begin{aligned}
\mathcal{H}_0 = & \sum_{ij\sigma} (\tilde{t}_{c,ij} - \mu\delta_{ij}) c_{i\sigma}^\dagger c_{j\sigma} \\
& + \sum_{ij\sigma} \{|b|^2 \tilde{t}_{f,ij} + (\epsilon_f + \lambda - \mu)\delta_{ij}\} f_{i\sigma}^\dagger f_{j\sigma} \\
& + \sum_{ij\sigma\sigma'} \{b^* \tilde{V}_{ij\sigma\sigma'} c_{i\sigma}^\dagger f_{j\sigma'} + \text{h.c.}\},
\end{aligned} \tag{3.14}$$

[1] Note that the notation of Fourier components is slightly different from that of the other chapters.

$$\mathcal{H}_{\rm com} = \sum_{ij\sigma\sigma'} \tau_{c,ij\sigma\sigma'} c^\dagger_{i\sigma} c_{j\sigma'} + \sum_{ij\sigma\sigma'} |b|^2 \tau_{f,ij\sigma\sigma'} f^\dagger_{i\sigma} f_{j\sigma'} + \sum_{ij\sigma\sigma'} \left\{ b^* \Upsilon_{ij\sigma\sigma'} c^\dagger_{i\sigma} f_{j\sigma'} + \text{h.c.} \right\}, \tag{3.15}$$

where

$$\tilde{t}_{c,ij} = J_0(A\rho_{ij}(\theta_A)) t_{c,ij}, \tag{3.16}$$

$$\tilde{t}_{f,ij} = J_0(A\rho_{ij}(\theta_A)) t_{f,ij}, \tag{3.17}$$

$$\tilde{V}_{ij\sigma\sigma'} = J_0(A\rho_{ij}(\theta_A)) V_{ij\sigma\sigma'}, \tag{3.18}$$

$$\tau_{c,ij\sigma\sigma'} = 2i \sum_k \mathcal{J}_{ikj}(A, \theta_A) \frac{t_{c,ik} t_{c,kj} + |b|^2 V_{ik\sigma s} V^*_{jk\sigma' s}}{\omega}, \tag{3.19}$$

$$\tau_{f,ij\sigma\sigma'} = 2i \sum_k \mathcal{J}_{ikj}(A, \theta_A) \frac{|b|^2 t_{f,ik} t_{f,kj} + V^*_{kis\sigma} V_{kjs\sigma'}}{\omega}, \tag{3.20}$$

$$\Upsilon_{ij\sigma\sigma'} = 2i \sum_k \mathcal{J}_{ikj}(A, \theta_A) \frac{t_{c,ik} V_{kj\sigma\sigma'} + |b|^2 V_{ik\sigma\sigma'} t_{f,kj}}{\omega}, \tag{3.21}$$

$$\mathcal{J}_{ikj}(A, \theta_A) = \sum_{n>0} \frac{(-1)^n J_n(A\rho_{ik}(\theta_A)) J_n(A\rho_{kj}(\theta_A))}{n} \sin\left[n(\phi_{ik}(\theta_A) - \phi_{kj}(\theta_A)) \right]. \tag{3.22}$$

In this effective model, we find two types of effect induced by the laser light.

(i) *Dynamical localization*
Looking at the zero-th order term $\mathcal{H}_0$, we find that the amplitudes of hopping in (3.16), (3.17) and hybridization in (3.18) are renormalized by zero-th Bessel function. Thus the amplitudes decrease with increasing the laser intensity. This effect corresponds to the phenomenon called dynamical localization [111], which causes freezing of the motion of electrons when the system is irradiated by a strong electric field [122]. The important point in our study is that this affects only off-site terms ($i \neq j$) since the Peierls phase is equal to zero in on-site terms ($i = j$).

(ii) *Laser-induced hopping and hybridization*
In the commutator term $\mathcal{H}_{\rm com}$, we find the new hopping terms (3.19), (3.20) and hybridization term (3.21) which do not exist in the original Hamiltonian (3.1). They depend not only on the position but also on the spins of electrons. Thus these terms can be regarded as an effective spin-orbit coupling. They give a drastic effect on the renormalized band structure, such as a level splitting. We note that these terms can break the time-reversal symmetry depending on the polarization of the laser field. In such a case they can be interpreted as an effective magnetic field.

The important point is that these two effects are derived from the quite general model which describes heavy fermion systems. Thus these effects are expected to appear generically in heavy fermion systems.

In the following sections, we demonstrate the physical consequences of these effects with calculations of concrete models. In Sec. 3.4, we show that the dynamical localization affects the Kondo effect in Kondo insulators. We find that the Kondo effects are enhanced or suppressed by laser light depending on whether the hybridization is on-site or not. In Sec. 3.5, we demonstrate that various laser-induced topological phase transitions are realized in a certain type of Kondo insulators.

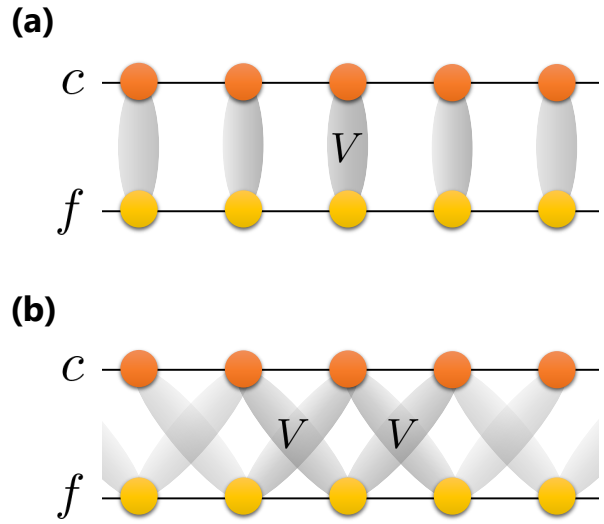

Figure 3.1: Schematic picture of c-f hybridization. (a) on-site model: The c- and f- electrons hybridize only at the same site (b) off-site model: The c- and f- electrons hybridize only at the nearest-neighbor sites. There is no on-site hybridization. Note that, although this figure treats one-dimensional systems for simplicity, we consider three-dimensional systems in our study,

3.4 Control of Kondo effect

In order to demonstrate the effect of laser light on the Kondo effect, we introduce two simple models, which show the qualitatively opposite behavior under the laser light as we see below. One is an on-site model $\mathcal{H}_{\rm on}$, which has only an on-site hybridization term. The other is an off-site model $\mathcal{H}_{\rm off}$, in which the localized electrons can hybridize to the conducting orbit only at the nearest neighbor sites. The structures of hybridization are schematically shown in Fig. 3.1. For simplicity, we assume cubic symmetry and then the Hamiltonian reads

$$\mathcal{H}_{\rm on/off} = \mathcal{H}^{(c)} + \mathcal{H}^{(f)} + \mathcal{H}^{\rm (hyb)}_{\rm on/off} + \mathcal{H}^{\rm (int)}, \tag{3.23}$$

$$\mathcal{H}^{(c)} = \sum_{\boldsymbol{k}\sigma} (\epsilon_c(\boldsymbol{k}) - \mu) c^\dagger_{\boldsymbol{k}\sigma} c_{\boldsymbol{k}\sigma}, \tag{3.24}$$

$$\mathcal{H}^{(f)} = \sum_{\boldsymbol{k}\sigma} (\epsilon_f(\boldsymbol{k}) - \mu) f^\dagger_{\boldsymbol{k}\sigma} f_{\boldsymbol{k}\sigma}, \tag{3.25}$$

$$\mathcal{H}^{\rm (int)} = U \sum_i n^{(f)}_{i\uparrow} n^{(f)}_{i\downarrow}, \tag{3.26}$$

$$\mathcal{H}^{\rm (hyb)}_{\rm on} = \sum_{\boldsymbol{k}\sigma} \{ V c^\dagger_{\boldsymbol{k}\sigma} f_{\boldsymbol{k}\sigma} + \text{h.c.} \}, \tag{3.27}$$

$$\mathcal{H}^{\rm (hyb)}_{\rm off} = \sum_{\boldsymbol{k}\sigma} \{ V(\boldsymbol{k}) c^\dagger_{\boldsymbol{k}\sigma} f_{\boldsymbol{k}\sigma} + \text{h.c.} \}, \tag{3.28}$$

with

$$\epsilon_c(\boldsymbol{k}) = -2t_c(\cos k_x + \cos k_y + \cos k_z), \tag{3.29}$$
$$\epsilon_f(\boldsymbol{k}) = \epsilon_f - 2t_f(\cos k_x + \cos k_y + \cos k_z), \tag{3.30}$$
$$V(\boldsymbol{k}) = iV(\sin k_x + \sin k_y + \sin k_z). \tag{3.31}$$

Here $c_{\boldsymbol{k}\sigma}$ and $f_{\boldsymbol{k}\sigma}$ are the momentum representations of the annihilation operators. Note that the parity of the conduction electron is fixed in the models, i.e. the on-site (off-site) model corresponds to odd (even) parity, since the parity of the localized electrons (f-orbit) is odd. Therefore most of heavy fermion materials (s-f or d-f hybridization) are represented by $\mathcal{H}_{\rm off}$ and the heavy fermion systems with p-f hybridization are represented by $\mathcal{H}_{\rm on}$.

These models correspond to the specific cases of the model discussed in Sec.III. Thus we can apply the results in Sec. 3.3 to these models. With linearly polarized laser light ($\varphi = 0$), we obtain the effective models as

$$\mathcal{H}^{\rm (lin)}_{\rm eff,on/off} = \tilde{\mathcal{H}}^{(c)} + \tilde{\mathcal{H}}^{(f)} + \tilde{\mathcal{H}}^{\rm (hyb,lin)}_{\rm on/off}, \tag{3.32}$$

$$\tilde{\mathcal{H}}^{(c)} = \sum_{\boldsymbol{k}\sigma} (\tilde{\epsilon_c}(\boldsymbol{k}) - \mu) c^\dagger_{\boldsymbol{k}\sigma} c_{\boldsymbol{k}\sigma}, \tag{3.33}$$
$$\tilde{\mathcal{H}}^{(f)} = \sum_{\boldsymbol{k}\sigma} (\tilde{\epsilon_f}(\boldsymbol{k}, |b|) + \lambda - \mu) f^\dagger_{\boldsymbol{k}\sigma} f_{\boldsymbol{k}\sigma}, \tag{3.34}$$
$$\tilde{\mathcal{H}}^{\rm (hyb,lin)}_{\rm on} = \sum_{\boldsymbol{k}\sigma} \{V b^* c^\dagger_{\boldsymbol{k}\sigma} f_{\boldsymbol{k}\sigma} + \text{h.c.}\}, \tag{3.35}$$
$$\tilde{\mathcal{H}}^{\rm (hyb,lin)}_{\rm off} = \sum_{\boldsymbol{k}\sigma} \{\tilde{V}(\boldsymbol{k}) b^* c^\dagger_{\boldsymbol{k}\sigma} f_{\boldsymbol{k}\sigma} + \text{h.c.}\}, \tag{3.36}$$

with

$$\tilde{\epsilon}_c(\boldsymbol{k}) = -2t_c(J_0(A_x)\cos k_x + J_0(A_y)\cos k_y + \cos k_z), \tag{3.37}$$

$$\tilde{\epsilon}_f(\boldsymbol{k}) = \epsilon_f - 2t_f|b|^2(J_0(A_x)\cos k_x + J_0(A_y)\cos k_y + \cos k_z), \tag{3.38}$$

$$\tilde{V}(\boldsymbol{k}) = iV(J_0(A_x)\sin k_x + J_0(A_y)\sin k_y + \sin k_z). \tag{3.39}$$

Here we define A_x and A_y as $(A_x, A_y) = A(\cos\theta_A, \sin\theta_A)$. The important difference between the on-site and off-site models is the existence/absence of the dynamical localization effect in the hybridization. Note that this effective Hamiltonian includes only the zero-th order term $\mathcal{H}_0$. Namely, the commutator contribution, $\mathcal{H}_{\rm com}$, vanishes. Thus there are only the effects of the dynamical localization which can be seen in eqs. (3.37), (3.38), and (3.39). On the other hand, in the case of the circularly polarized laser light ($\varphi = -\pi/2$), the effective Hamiltonian includes the commutator contribution, $\mathcal{H}_{\rm com}$, as

$$\mathcal{H}^{\rm (cir)}_{\rm eff,on/off} = \tilde{\mathcal{H}}^{(c)} + \tilde{\mathcal{H}}^{(f)} + \tilde{\mathcal{H}}^{\rm (hyb,cir)}_{\rm on/off}, \tag{3.40}$$

with

$$\tilde{\mathcal{H}}^{\rm (hyb,cir)}_{\rm on} = \tilde{\mathcal{H}}^{\rm (hyb,lin)}_{\rm on} = \sum_{\boldsymbol{k}\sigma} \{V b^* c^\dagger_{\boldsymbol{k}\sigma} f_{\boldsymbol{k}\sigma} + \text{h.c.}\}, \tag{3.41}$$
$$\tilde{\mathcal{H}}^{\rm (hyb,cir)}_{\rm off} = \sum_{\boldsymbol{k}\sigma} \{(\tilde{V}(\boldsymbol{k}) + \Upsilon(\boldsymbol{k})) b^* c^\dagger_{\boldsymbol{k}\sigma} f_{\boldsymbol{k}\sigma} + \text{h.c.}\}. \tag{3.42}$$

Here we have defined

$$\Upsilon(\boldsymbol{k}) = -\frac{4(t_c - |b|^2 t_f)V}{\omega}\mathcal{J}(A_x, A_y)\sin(k_x - k_y), \tag{3.43}$$

$$\mathcal{J}(A_x, A_y) = \sum_{m=0} \frac{(-1)^m J_{2m+1}(A_x)J_{2m+1}(A_y)}{2m+1}. \tag{3.44}$$

$\Upsilon(\boldsymbol{k})$ in $\tilde{\mathcal{H}}^{(\mathrm{hyb,cir})}_{\mathrm{on/off}}$ comes from $\mathcal{H}_{\mathrm{com}}$. This term corresponds to the laser-induced hybridization which does not exist in the original model and connects a site with its next-nearest-neighboring sites. Moreover, this term gives rise to the breaking of time-reversal symmetry, which is inherent in the circularly polarized laser light. As we see below, this effect only gives a small contribution to the Kondo effect. However, this kind of laser-induced hopping and hybridization plays a crucial role for the topological properties. This point is discussed in Sec. 3.5.

3.4.1 Numerical results

Linearly polarized laser light

Following the methods shown in Sec. 3.2, we numerically calculate the renormalization factor b and the energy shift of the f-electron level λ self-consistently for the effective models (3.32) and (3.40). Then, based on the results, we discuss the effect of laser light on the Kondo effect. We note here that in the slave boson approach, the fomation of Kondo singlets is well described in terms of the renormalization factor b, although the crossover behavior at finite temperatures appears as a phase transition with the order parameter b. Although this transition is artificial, it is known that the transition temperature corresponds to the Kondo temperature [131–133], which is a characteristic temperature where the Kondo effect takes place. Below the Kondo temperature, we can correctly describe the formation of the Kondo singlets and the resulting insulating behavior characteristic of the Kondo insulator.

First we consider the case of the linearly polarized laser light. The results for the on-site model are shown in Fig. 3.2(a). From Fig. 3.2(a), we find that the Kondo temperature is enhanced with increasing the intensity of laser light. Thus the Kondo effect is enhanced in the on-site model. On the other hand, we find that the Kondo temperature decreases as we increase the intensity of laser light in Fig. 3.2(b) for the off-site model. This means that the Kondo effect is suppressed in the off-site model. These results suggest that whether the Kondo effect is enhanced or suppressed depends on the spatial structure of the hybridization. Only in the off-site model, the hybridization terms couple to the electromagnetic fields and then the dynamical localization takes place in eq. (3.28). As seen in eq. (3.27), the on-site model does not show the dynamical localization in the hybridization. This difference plays a crucial role in generating the opposite behavior of the Kondo effect in those models. The origin of this behavior is discussed in Sec. 3.4.2.

Circularly polarized laser light

Next we consider the circularly polarized laser light. For the on-site model, the effective model with circularly polarized laser light is the same as the one with linearly polarized laser light, shown in eq. (3.41). Thus we study only the off-site model in this subsection.

The results for the circularly polarized laser are shown in Fig. 3.3. From Fig 3.3 (a), we find that the Kondo temperature is suppressed by increasing the laser intensity in the same manner as in the case of the linearly polarized laser. The behavior is quite similar to that in Fig. 3.2 (b.1) and thus the effect of the laser-induced hybridization, which appears only

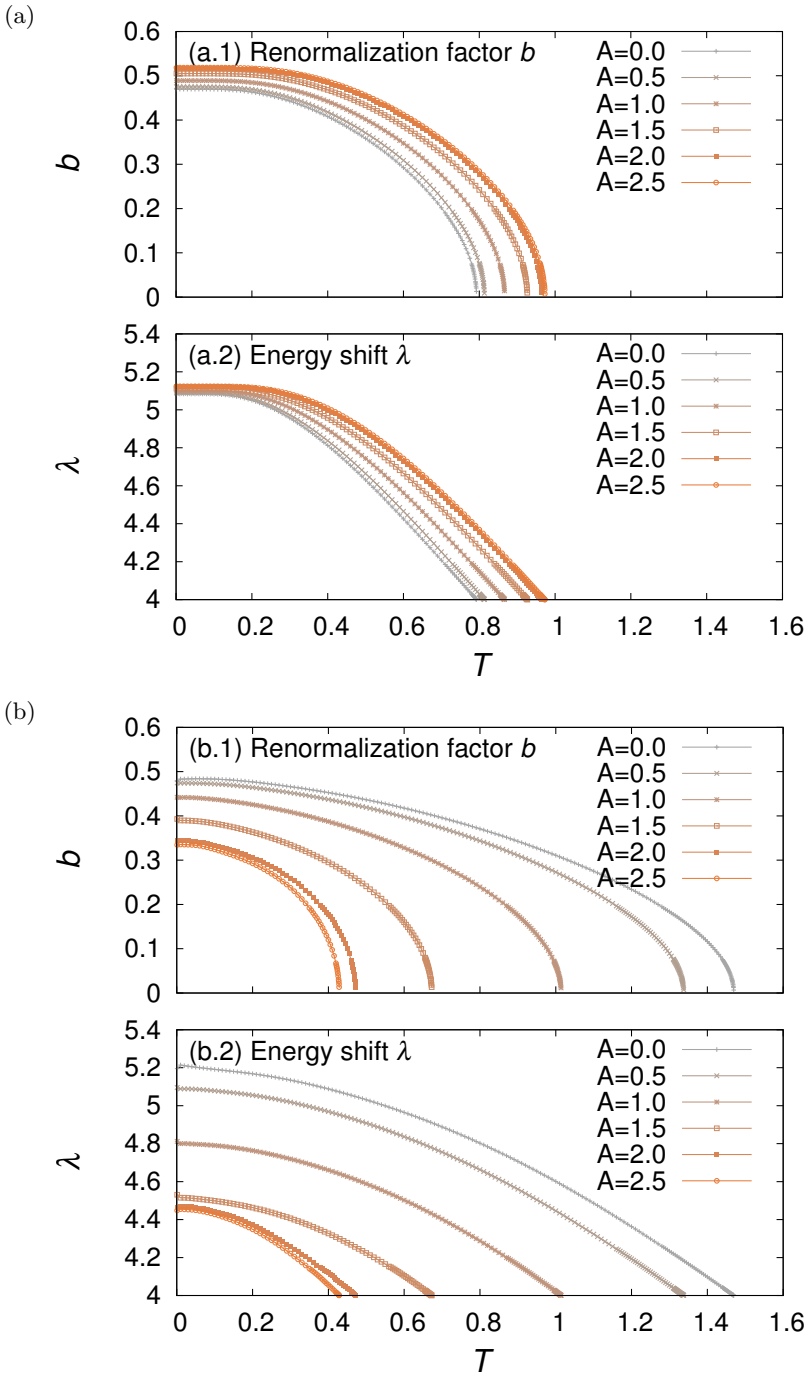

Figure 3.2: Numerical solutions of the self-consistent equations for (a) the on-site model and (b) the off-site model with the linearly polarized laser light. We show the temperature dependence of (a.1) the renormalization factor b and (a.2) the energy shift λ for the on-site model. The same things for the off-site model are shown in Fig. (b.1) and (b.2) respectively. Here $A_x = A_y = A$ and we use the parameters as $t_c = 1$, $t_f = -0.2$, $V = 3$, $\epsilon_f = -4$ and $\omega = 12.5$.

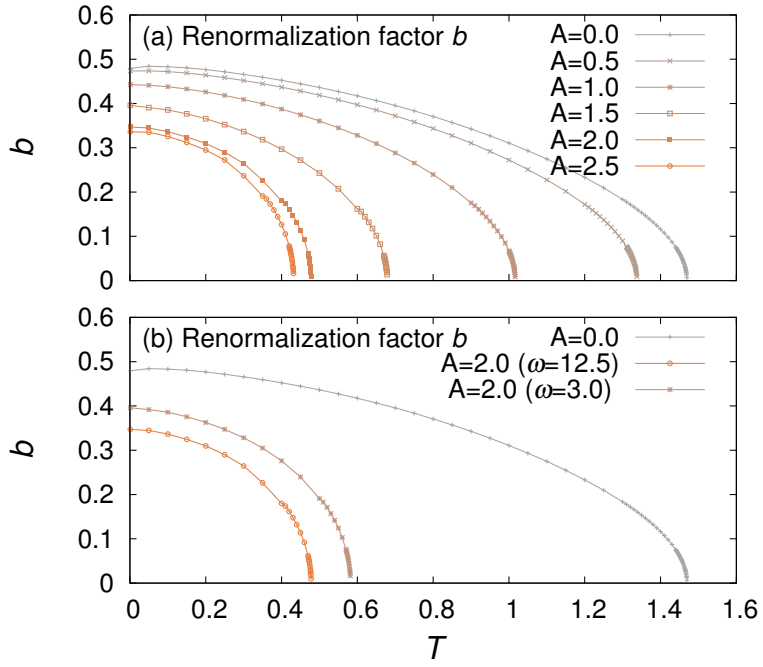

Figure 3.3: Numerical solutions of the self-consistent equations for the off-site model with the circularly polarized laser light. In Fig. (a), we show the temperature dependence of the renormalization factor b. Here $A_x = A_y = A$ and we use the parameters as $t_c = 1$, $t_f = -0.2$, $V = 3$, $\epsilon_f = -4$ and $\omega = 12.5$. In Fig.(b), to clarify the effect of laser-induced hybridization, we compare the results of $\omega = 3.0$ and $\omega = 12.5$ at the same intensity ($A = 2.0$). All the parameters except for the frequency are set same as Fig. (a).

when the laser is circularly polarized, is difficult to find out. To clarify the reason, we examine the low-frequency regime ($\omega = 3.0$), in which our high frequency expansion could still predict the qualitative tendency. The results are shown in Fig. 3.3(b). We find that the Kondo temperature in the low frequency regime ($\omega = 3.0$) is higher than the one in the high frequency regime ($\omega = 12.5$) and thus confirm that the laser-induced hybridization indeed enhances the Kondo effect. Therefore, the reason why this effect is difficult to find out in the high frequency regime ($\omega = 12.5$) is that the extra hybridization $\Upsilon(\boldsymbol{k})$ is much smaller than the zero-th order term $\mathcal{H}_0$ in the high frequency expansion and then does not give an important effect on the Kondo effect.

3.4.2 Enhancement/Suppression of Kondo effect

In order to understand the origin of the qualitatively opposite behavior of the Kondo effect in the on-site and off-site model, we give a rough estimation of the Kondo temperature in this subsection. In the strong coupling limit $U \to \infty$, it is known that the Kondo temperature is approximately given as [131]

$$T_K \simeq D \exp\left(\frac{\epsilon_f - \mu}{2\rho_0 V^2}\right). \tag{3.45}$$

Here D is the band width of the conduction electrons and ρ_0 is the density of states at the Fermi energy. We incorporate the effect of the laser light in this formula. The effective form of

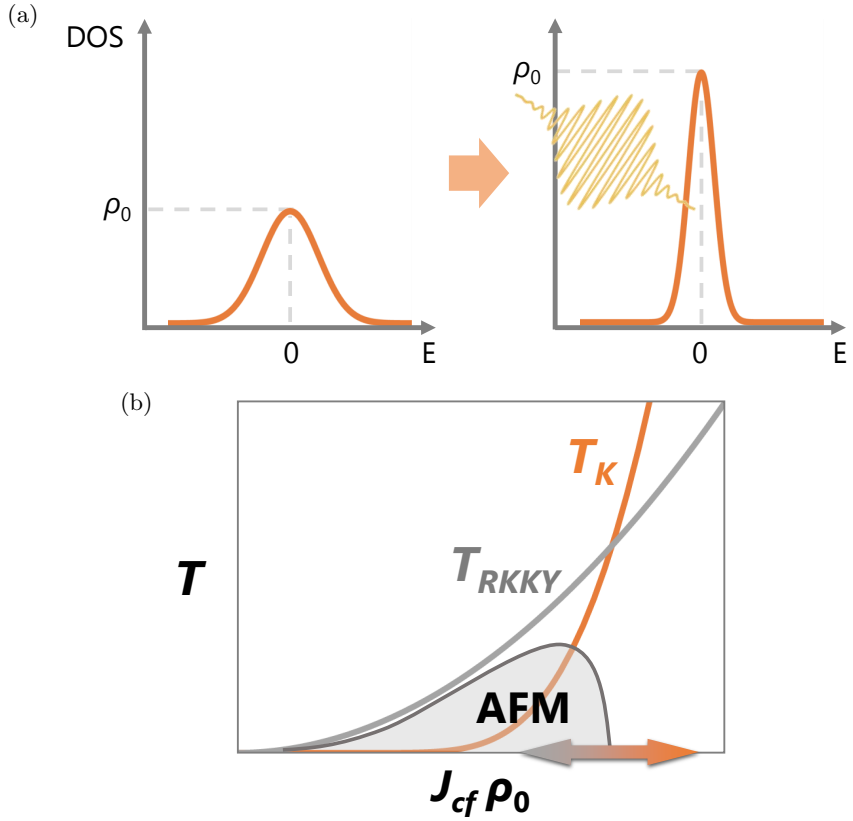

Figure 3.4: (a) The schematic picture of the enhancement of the density of states near the Fermi energy ρ_0. It is the origin of the enhancement of the Kondo effect in the on-site model. (b) Schematic Doniach phase diagram. Changing the Kondo coupling J_{cf} or the density of states ρ_0 by some perturbations, e.g. pressure, we can induces the quantum phase transition. AFM represents an antiferromagnetic phase.

the conduction band (3.29) shows that the hopping amplitude is renormalized by the zero-th Bessel function, and then we treat this effect by replacing t_c with $\tilde{t_c} = J_0(A)t_c$. Here A is the amplitude of the laser light. Considering $D \sim t$ and $\rho_0 \sim D^{-1}$, we obtain the Kondo temperature of the laser-irradiated model as

$$\tilde{T}_K^{(\mathrm{on})}(A) \simeq J_0(A) D \exp\left(J_0(A) \frac{\epsilon_f - \mu}{2\rho_0 V^2} \right). \tag{3.46}$$

Since $\epsilon_f - \mu$ is negative and thus this formula implies that the Kondo temperature increases in the low intensity region (i.e. small A). This estimation shows a qualitative agreement with the numerical results in Sec. IV B. This agreement suggests that the dynamical localization plays the key role in this enhancement of Kondo effect. The dynamical localization makes the band width narrower, thereby enhancing the density of states near the Fermi surface (see Fig. 3.4(a)). This enhancement of the density of states helps the formation of Kondo singlet.

On the other hand, in the off-site model, we have to additionally consider the dynamical localization of hybridization and thus we treat this effect by replacing V with $\tilde{V} = J_0(A)V$. Then we obtain

$$\tilde{T}_K^{(\mathrm{off})}(A) \simeq J_0(A) D \exp\left((J_0(A))^{-1} \frac{\epsilon_f - \mu}{2\rho_0 V^2} \right). \tag{3.47}$$

This formula shows that the Kondo temperature of the laser-irradiated off-site model decreases in the low intensity region. This is a qualitatively different behavior from the on-site model. The origin of th suppression is the dynamical localization effect in the c-f hybridization.

Before closing this section, we mention possible laser-induced quantum phase transitions via controlling Kondo effect with laser light. As we mentioned above, the interplay of the Kondo effect and the RKKY interaction plays a crucial role in heavy fermion systems and their competition gives various quantum phases, including the magnetically ordered phases, and the resulting phases are well described by the Doniach phase diagram [126] shown in Fig.3.4(b). We have shown that the Kondo effect can be enhanced or suppressed by laser light. Therefore, we can make either the Kondo effect or the RKKY interaction dominant. In the case that the Kondo effect is suppressed, the RKKY interaction becomes dominant and the system can realize a magnetically ordered phase. Applying the laser light effectively changes the Kondo coupling J_{cf} and the density of states ρ_0. Then the system goes beyond the quantum critical point [2] and shows a transition to a magnetic phase (typically, an antiferromagnetic phase) in Doniach phase diagram in Fig.3.4(b). This laser-induced quantum phase transition opens a new way to dynamically control the magnetic phases by laser light.

3.5 Control of topological phases

3.5.1 Model of topological Kondo insulators

Several Kondo insulators are known to show topologically nontrivial phases thanks to their peculiar hybridization structures. They are called topological Kondo insulators [127, 128], which are gathering great attention as analogue of topological insulators in strongly correlated electron systems. In this section, we demonstrate that the laser light changes the topological properties of the topological Kondo insulators. We use a variant of the periodic Anderson model which has off-site and (pseudo)spin-dependent hybridization terms, which is already introduced as a model of topological Kondo insulators in the previous works [135, 136]. The model Hamiltonian reads

$$\begin{aligned}\mathcal{H} = &\sum_{\boldsymbol{k}\sigma}(\epsilon_c(\boldsymbol{k})-\mu)c^\dagger_{\boldsymbol{k}\sigma}c_{\boldsymbol{k}\sigma} + \sum_{\boldsymbol{k}\sigma}(\epsilon_f(\boldsymbol{k})-\mu)f^\dagger_{\boldsymbol{k}\sigma}f_{\boldsymbol{k}\sigma} \\ &+ \sum_{\boldsymbol{k}\sigma\sigma'}\{(\boldsymbol{V}(\boldsymbol{k})\cdot\boldsymbol{\sigma})_{\sigma\sigma'}c^\dagger_{\boldsymbol{k}\sigma}f_{\boldsymbol{k}\sigma'} + \text{h.c.}\} + U\sum_i n^{(f)}_{i\uparrow}n^{(f)}_{i\downarrow},\end{aligned} \tag{3.48}$$

with

$$\boldsymbol{V}(\boldsymbol{k}) = V(a_1\sin k_x, a_2\sin k_y, a_3\sin k_z). \tag{3.49}$$

Here $\sigma,\sigma'(=\uparrow,\downarrow)$ stands for the (pseudo)spin and $\boldsymbol{\sigma}$ are Pauli matrices. In this study, the parameters are set as $a_1=2$, $a_2=-2$ and $a_3=4$. $\epsilon_c(\boldsymbol{k})$ and $\epsilon_f(\boldsymbol{k})$ have already been defined in eqs. (3.29) and (3.30). Since $\epsilon_c(\boldsymbol{k})$ and $\epsilon_f(\boldsymbol{k})$ are parity even and $\boldsymbol{V}(\boldsymbol{k})$ is parity odd, this model has time-reversal symmetry, and thus topological states are characterized by a Z_2 topological invariant [127, 137, 138]. With slave boson mean-fields b and λ, we can write down the topological invariants ν_{STI} and ν^α_{WTI} ($\alpha=x,y,z$) for the renormalized band structure in a

[2] Near the quantum critical point, the quantum fluctuation should be dominant and thus we may need another approach to treat quantum fluctuation beyond the slave-boson mean-field treatment (e.g. DMFT).

simplified form [139] as

$$(-1)^{\nu_{\rm STI}} = \prod_m \delta_m, \tag{3.50}$$

$$(-1)^{\nu^\alpha_{\rm WTI}} = \prod_m \delta_m \Big|_{(\boldsymbol{k}^*_m)_\alpha = 0}, \tag{3.51}$$

where $\boldsymbol{k}_m$ represents the time-reversal invariant momenta (TRIM) in three dimensional Brillouin zone, $\delta_m = {\rm sgn}(\epsilon_c(\boldsymbol{k}_m) - \bar{\epsilon}_f(\boldsymbol{k}_m, |b|^2) - \lambda)$ is the parity eigenvalue on each TRIM, and $\bar{\epsilon}_f(\boldsymbol{k}) = \epsilon_f - 2t_f|b|^2(\cos k_x + \cos k_y + \cos k_z)$. Note that $\nu_{\rm STI} = 1$ ($\nu^\alpha_{\rm WTI} = 1$) means the system is a strong (weak) topological insulator.

3.5.2 Linearly polarized laser light

First we consider the application of linearly polarized light. The model introduced above corresponds to a specific case of the model which we discussed in Sec. 3.3. Thus we can apply the results in Sec. 3.3 to this model. With linearly polarized laser light ($\varphi = 0$), we obtain the effective model as

$$\begin{aligned}\mathcal{H}_{\rm eff} = &\sum_{\boldsymbol{k}\sigma} \{\tilde{\epsilon_c}(\boldsymbol{k}) - \mu\} c^\dagger_{\boldsymbol{k}\sigma} c_{\boldsymbol{k}\sigma} \\ &+ \sum_{\boldsymbol{k}\sigma} \{\tilde{\epsilon}_f(\boldsymbol{k}) + \lambda - \mu\} f^\dagger_{\boldsymbol{k}\sigma} f_{\boldsymbol{k}\sigma} \\ &+ \sum_{\boldsymbol{k}\sigma\sigma'} \{b^*(\tilde{\boldsymbol{V}}(\boldsymbol{k}) \cdot \boldsymbol{\sigma})_{\sigma\sigma'} c^\dagger_{\boldsymbol{k}\sigma} f_{\boldsymbol{k}\sigma'} + {\rm h.c.}\},\end{aligned} \tag{3.52}$$

with

$$\widetilde{\boldsymbol{V}}(\boldsymbol{k}) = V(a_1 J_0(A_x)\sin k_x, a_2 J_0(A_y)\sin k_y, a_3 \sin k_z). \tag{3.53}$$

$\tilde{\epsilon_c}(\boldsymbol{k})$ and $\tilde{\epsilon}_f(\boldsymbol{k})$ have already been defined in eqs. (3.37) and (3.38). As with the case of on/off-site model in Sec. 3.4, this effective Hamiltonian includes only the contributions coming from the zero-th order term $\mathcal{H}_0$. Thus there is only the effect of the dynamical localization of hopping and hybridization. We discuss how these dynamical localization effects change the topological nature of the original system.

To discuss the topological properties, we use the topological invariants. In the effective model (3.52), the time-reversal symmetry of the original model is preserved, and thus we can use the Z_2 topological invariants for the effective model. The topological invariants are represented by eqs. (3.50) and (3.51) in which $\epsilon_c(\boldsymbol{k})$ and $\bar{\epsilon}_f(\boldsymbol{k})$ are replaced by $\tilde{\epsilon_c}(\boldsymbol{k})$ and $\tilde{\epsilon}_f(\boldsymbol{k})$. The topological invariants include b and λ, which are calculated for each temperature T and laser intensity A. We calculate numerically $b = b(T, A)$ and $\lambda = \lambda(T, A)$ (Here we assume $A_x = A_y = A$) and use them to obtain $\nu_{\rm STI}(b(T, A), \lambda(T, A))$ and $\nu^\alpha_{\rm WTI}(b(T, A), \lambda(T, A))$. Note that we here apply the formula of the topological invariants at zero temperature to the mean-field Hamiltonian. This means that we calculate the topological invariants for the renormalized band structure determined at finite temperature. In the low temperature regime sufficiently below the Kondo temperature, which roughly corresponds to the gap size, the renormalized band structure is well defined and thus our treatment should appropriately describe the topological phases even at finite temperatures.

First we show the numerical results of the temperature dependence of b and λ in Fig. 3.5 (a) and (b) respectively. They show that the Kondo temperature decreases with increasing

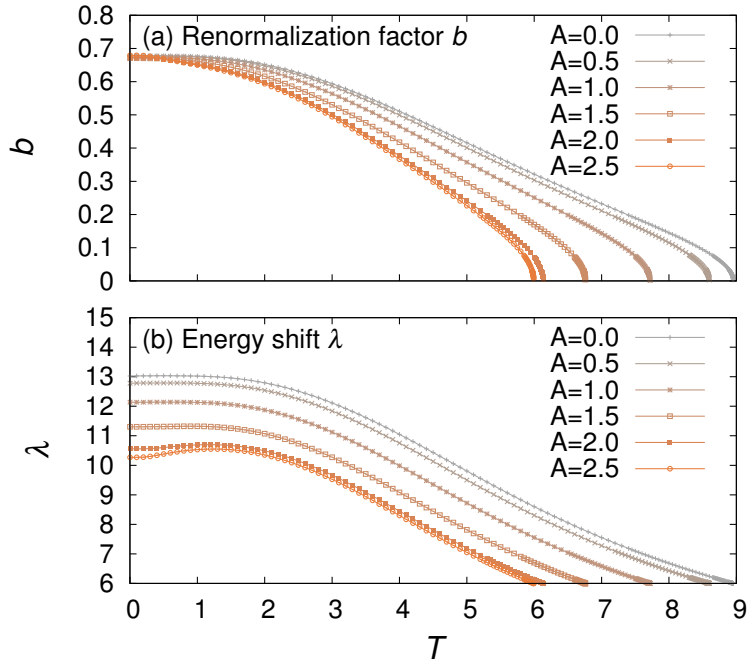

Figure 3.5: Numerical solutions of the self-consistent equations for the model of topological Kondo insulator with the linearly polarized laser light. In Fig. (a) and Fig. (b), we show the temperature dependence of the renormalization factor b and the energy shift λ respectively. Here $A_x = A_y = A$ and we use the parameters as $t_c = 1$, $t_f = -0.2$, $V = 3$, $\epsilon_f = -6$ and $\omega = 12.5$.

the intensity of laser light. This behavior is similar to the off-site model discussed in Sec. 3.4 because the model (3.48) also has only off-site hybridizations.

Using these results, we calculate the topological invariants (3.50) and (3.51) and present the results in Fig. 3.6. The topological invariants indeed change with temperature and laser intensity, implying that there exist the topological phase transitions induced by linearly polarized laser light.

Next we calculate the topological invariants in a broad range of (T, A) systematically and obtain the topological phase diagram shown in Fig.3.7. Note that all the boundaries located next to the trivial metal (tMetal) phase denote the crossover induced by Kondo effect. The other phase boundaries represent the topological phase transition which is well-defined by the renormalized band structure though it looks like a crossover in the high temperature region due to thermal fluctuations.

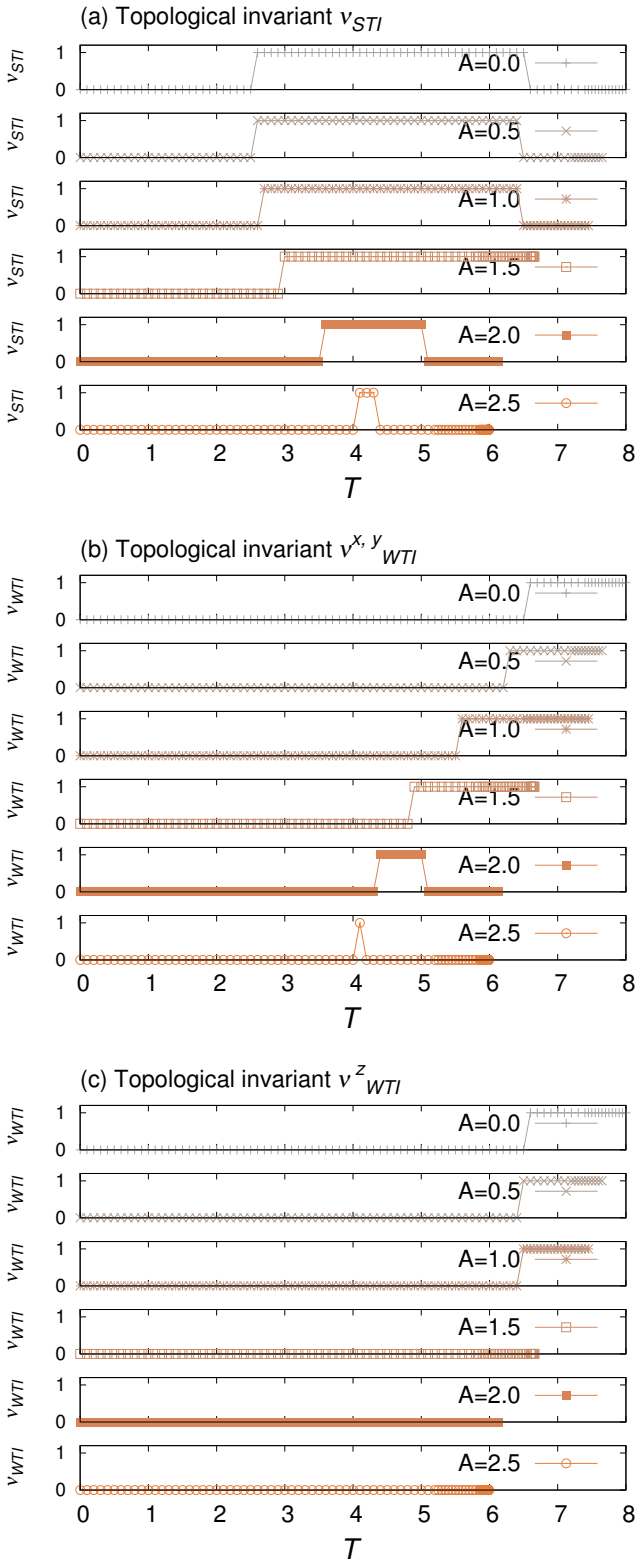

Figure 3.6: Topological invariants (a) $\nu_{\rm STI}$, (b) $\nu^{x,y}_{\rm WTI}$ and, (c) $\nu^{z}_{\rm WTI}$. Above the Kondo temperature, the topological invariants are not defined since the system is a paramagnetic metal. Here we use the parameters as $t_c = 1$, $t_f = -0.2$, $V = 3$, $\epsilon_f = -4$ and $\omega = 12.5$.

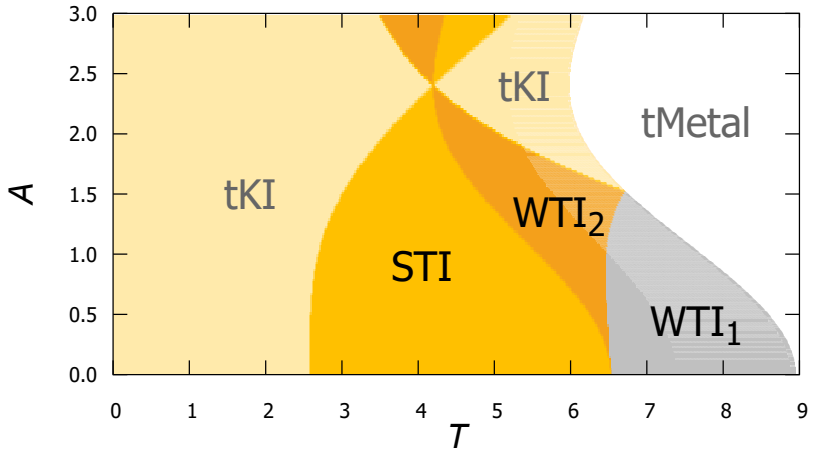

Figure 3.7: The phase diagram of the topological Kondo insulators irradiated by linearly polarized laser light. There are two topologically trivial phases and three topologically non-trivial phases: the trivial Kondo insulator phase (tKI, $b \neq 0$, all the topological invariants are zero), the trivial metal phase (tMetal, $b = 0$), the strong topological insulator (STI, $b \neq 0$, $\nu_{\rm STI} = 1$) phase and two kinds of the weak topological insulator (WTI) phases, $\rm WTI_1$ ($\boldsymbol{\nu} = (\nu^x_{\rm WTI}, \nu^y_{\rm WTI}, \nu^z_{\rm WTI}) = (1,1,1)$) and $\rm WTI_2$ ($\boldsymbol{\nu} = (1,1,0)$). Here we use the parameters as $t_c = 1$, $t_f = -0.2$, $V = 3$, $\epsilon_f = -4$ and $\omega = 12.5$.

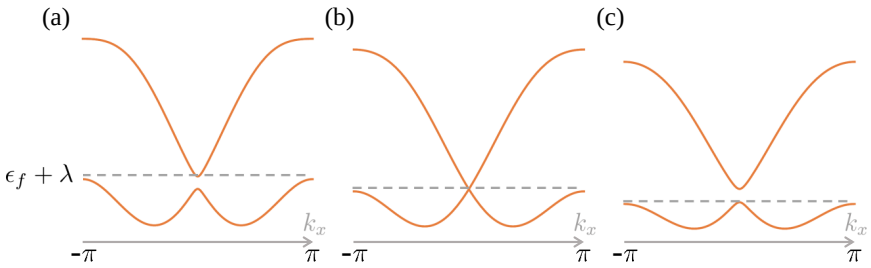

Figure 3.8: Laser-induced topological phase transition of the topological Kondo insulators with linearly polarized laser light. We show the calculated band structure for k_x (Both k_y and k_z are fixed to π). (a) Without laser light ($A = 0.0$), the system is in the STI phase. (b) Applying the laser light ($A = 0.54$), the band gap closes at the topological phase transition point. (c) Applying the strong laser light ($A = 0.8$), the system is changed to $\rm WTI_2$ phase. Here we use the parameters as $T = 6.2$, $t_c = 1$, $t_f = -0.2$, $V = 3$, $\epsilon_f = -4$ and $\omega = 12.5$.

In Fig. 3.7, we find three topologically non-trivial phases: one strong topological insulator (STI) and two types of weak topological insulators (WTIs). These WTIs have different values of the weak topological invariant of z-direction. Especially the $\rm WTI_2 (\nu^x_{\rm WTI} = \nu^y_{\rm WTI} = 1, \nu^z_{\rm WTI} = 0)$ is the phase which appears only with a finite value of the laser intensity A, because the laser light breaks the cubic symmetry to the tetragonal symmetry and the appearance of $\rm WTI_2$ is permitted. In the low intensity regime ($A \lesssim 1.0$), we find a laser-induced topological phase transition to the $\rm WTI_2$ phase near the temperature $T \sim 6.5$, which corresponds to the boundary

of the topological phases without laser light. To clarify how the phase transition occurs, we show the calculated band structure for each laser intensity in Fig. 3.8. From the figure, we find that the renormalized f-electron level $\epsilon_f + \lambda$ shifts due to the suppression of Kondo effect by laser light. According to this shift of energy level, the band touching occurs at the $A = 0.54$ shown in Fig. 3.8 (b). After the band touching, the energy gap opens and the topological invariant changes.

In the strong intensity region, we find the interesting behavior that the region of the topologically non-trivial phases shrinks to the point $(T, A) = (4.2, 2.4)$ and after that it becomes broad again with increasing the laser intensity. The value of the laser intensity $A = 2.4$ corresponds to the minimal zero of the zero-th Bessel function. At that point, the hopping and hybridization in x- and y-direction vanish due to the dynamical localization and thus the system can be regarded as a one-dimensional system in z-direction. Therefore the topological invariants related to x- and y-direction, i.e. $\nu_{\rm STI}$, $\nu^x_{\rm WTI}$, and $\nu^y_{\rm WTI}$, must be zero and then the system becomes topologically trivial.

3.5.3 Circularly polarized laser light

Next we consider the case of the circularly polarized laser ($\varphi = -\pi/2$). Using the results in Sec. 3.3, we obtain the effective model as

$$\begin{aligned}\mathcal{H}_{\rm eff} = &\sum_{\boldsymbol{k}\sigma}\{\tilde{\epsilon_c}(\boldsymbol{k}) - \mu + |b|^2\Phi_B(\boldsymbol{k})\mathrm{sgn}(\sigma)\}c^\dagger_{\boldsymbol{k}\sigma}c_{\boldsymbol{k}\sigma} \\ &+ \sum_{\boldsymbol{k}\sigma}\{\tilde{\epsilon}_f(\boldsymbol{k}) + \lambda - \mu + |b|^2\Phi_B(\boldsymbol{k})\mathrm{sgn}(\sigma)\}f^\dagger_{\boldsymbol{k}\sigma}f_{\boldsymbol{k}\sigma} \\ &+ \sum_{\boldsymbol{k}\sigma\sigma'}\{b^*((\tilde{\boldsymbol{V}}(\boldsymbol{k}) + \boldsymbol{\Phi}(\boldsymbol{k}))\cdot\boldsymbol{\sigma})_{\sigma\sigma'}c^\dagger_{\boldsymbol{k}\sigma}f_{\boldsymbol{k}\sigma'} + \mathrm{h.c.}\},\end{aligned} \tag{3.54}$$

with

$$\boldsymbol{\Phi}(\boldsymbol{k}) = -\frac{4i(t_c - |b|^2 t_f)V}{\omega}\mathcal{J}(A_x, A_y)(a_1\cos k_x \sin k_y, -a_2 \sin k_x \cos k_y, 0), \tag{3.55}$$

$$\Phi_B(\boldsymbol{k}) = -\frac{2V^2}{\omega}\mathcal{J}(A_x, A_y)(a_1 a_2^* + a_1^* a_2)\cos k_x \cos k_y. \tag{3.56}$$

$\mathcal{J}(A_x, A_y)$ has already been defined in eq. (3.44). In this effective model, we obtain two terms that come from the commutator contribution $\mathcal{H}_{\rm com}$. These terms break the time-reversal symmetry, as the circularly polarized laser does. One is the laser-induced hybridization (LH) term $\boldsymbol{\Phi}(\boldsymbol{k})$ stemming from the commutator of the kinetic term and the hybridization term. From the commutator between the x and y components of hybridization term, we obtain the other term $\Phi_B(\boldsymbol{k})$, which plays a role of the laser-induced Zeeman coupling to (pseudo)spins. Then we regard them as a laser-induced "magnetic" field (LM). This term behaves in a similar way to a usual magnetic field, but there are two differences from the usual magnetic field. One is that the LM depends on momenta, namely, it behaves like a Zeeman-type spin-orbit coupling. The other is that the LM is proportional to a square of the mean field, $|b|^2$. The mean field $|b|$ is finite only below the Kondo temperature and becomes larger in the low temperature regime. Namely, this magnetic field grows with decreasing temperature. Especially the second difference is a quite unique feature because this behavior reflects the Kondo effect and thus it only can appear in many-body Floquet systems.

As we mentioned above, the time-reversal symmetry is broken in this effective model (3.54). Therefore we cannot define the original topological numbers (3.50) and (3.51). On the other

hand, it is known that time-reversal symmetry or inversion symmetry broken topological insulators can be Weyl semimetals [140], which are topological gapless phases of matter recently gathering great attention because they have the exotic Fermi-arc surface states and show the exotic transport phenomena related to Chiral anormaly [141]. Weyl semimetals are characterized by the existence of pairs of topologically non-trivial point nodes, which correspond to the monopole and anti-monopole of Berry curvature. The texture of the Berry curvature can be detected by the Chern number for the two-dimensional subspace of the three-dimensional Brillouin zone. To detect the Weyl semimetallic phase, we calculate the Chern numbers for the k_x-k_y plane (fixing k_z) for several values of k_z. The Chern number for each k_z is defined as follows:

$$C(k_z) = \frac{1}{2\pi i} \int_{\text{B.Z.}} dk_x dk_y \epsilon^{\alpha\beta} \sum_{n:\text{filled}} \partial_{k_\alpha} \langle u_n(\boldsymbol{k}) | \partial_{k_\beta} u_n(\boldsymbol{k}) \rangle \,, \tag{3.57}$$

where α and β run over x and y. $|u_n(\boldsymbol{k})\rangle$ is the Bloch wave function defined by the eigenfunction of the effective Hamiltonian with numerically calculated b and λ for each (T, A). If we find the change of the Chern number $C(k_z)$ at k_z^*, i.e. $C(k_z > k_z^*) \neq C(k_z < k_z^*)$, we conclude that there is a Weyl node in the $k_z = k_z^*$ plane. The change of the Chern number at k_z^* corresponds to the monopole charge of the Weyl nodes. Here we numerically calculate the Chern numbers with Fukui-Hatsugai-Suzuki method by discretizing the Brillouin zone [117]. Note that we apply the formula of the topological number at zero temperature to the mean-field model which can describe even the finite temperature regime. As mentioned in the previous subsection, this treatment is reasonable in the low temperature regime sufficiently below the Kondo temperature.

Before evaluating the Chern number, we calculate b and λ for each (T, A) to obtain the renormalized band structure. We show the numerically calculated b and λ in Fig. 3.9 (a) and (b). From the figures, we find that the Kondo temperature decreases with increasing the intensity of the laser light. This behavior is qualitatively same as the linearly polarized case explained in the previous subsections. The difference from the linearly polarized laser is only the existence of the LH and LM. However the effect of them on the Kondo effect is very small and difficult to find out in the high frequency regime because they are the first-order correction in the $1/\omega$ expansion. To clarify their effect, in Fig. 3.9 (c), we show the results in the case of $\omega = 3$, in which the $1/\omega$ expansion could not be used for quantitative arguments, but it is useful to find the qualitative effect of LH and LM. From Fig. 3.9 (c), it is seen that the LH enhances the Kondo effect in all the regime below the Kondo temperature since it enlarges the amplitude of the hybridization. On the other hand, the effect of LM is different depending on the temperature regime. Very near the Kondo temperature, it seems that LM does not affect the original model. It is because the value of b becomes small there, and thus the amplitude of LM $\sim |b|^2 V^2/\omega$ also becomes small. In the temperature below the Kondo temperature, LM slightly enhances the value of b, i.e. the size of the Kondo gap. This is quite different from the usual magnetic field, which is known to suppress the Kondo effect. The key difference of the LM from the usual magnetic field is the existence of the renormalization factor $|b|^2$. This factor is considered to play an important role at low temperature and realize the enhancement of the value of b.

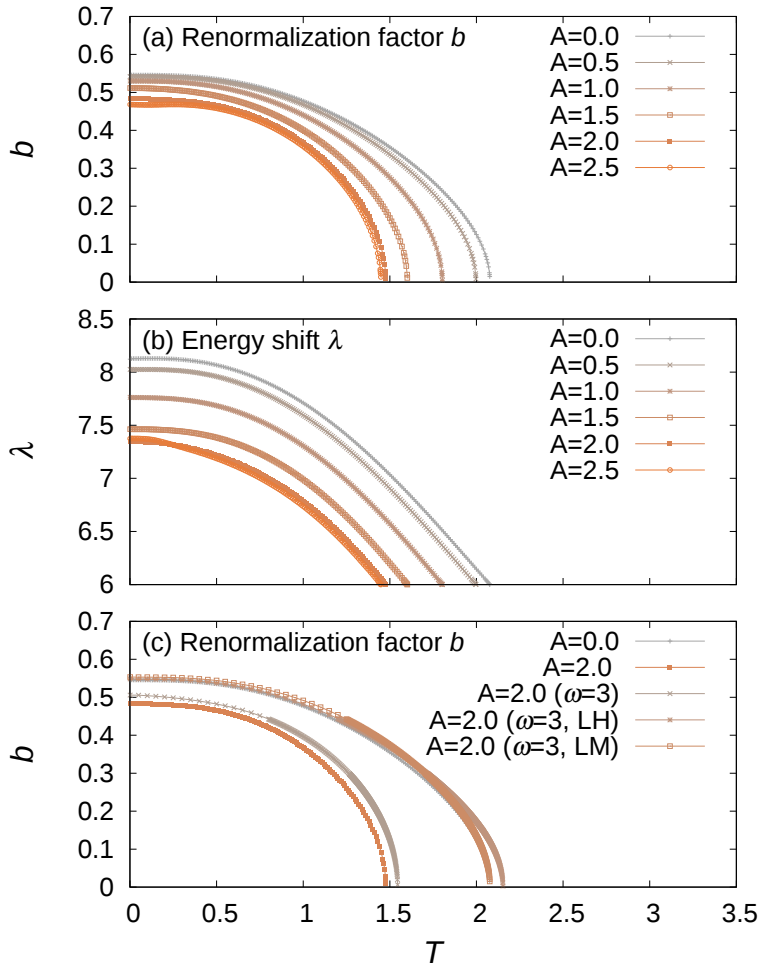

Figure 3.9: Numerical solutions of the self-consistent equations for the model of the topological Kondo insulator with the circularly polarized laser light. In Fig. (a) and Fig. (b), we show the temperature dependence of the renormalization factor b and the energy shift λ respectively. Here $A_x = A_y = A$ and we use the parameters as $t_c = 1$, $t_f = -0.2$, $V = 1.5$, $\epsilon_f = -4$ and $\omega = 12.5$. In Fig. (c), to clarify the effect which appears only in the case of circularly polarized laser, we compare the results of $\omega = 3.0$ and $\omega = 12.5$ at the same intensity ($A = 2.0$). LH and LM represents the case that only includes the effect of laser-induced hybridization and laser-induced magnetic field respectively. The other parameters than the frequency are the same as Fig. (a) and Fig. (b).

Using the calculated b and λ, we obtain the renormalized band structure and find the phase transition to Weyl semimetallic phases. To clarify this point, we show the deformation of the band structure by laser light in Fig. 3.10. Before applying the laser light, we prepare the system in the STI phase ($A = 0.0$, $T = 0.1$). With a finite laser intensity, the bands show the Zeeman-type splitting due to the LM. Increasing the laser intensity, the bands touch and cross each other. The crossing point can be Weyl nodes, which characterize the Weyl semimetal. We calculate the change of the Chern number when we go over the crossing point in the k_x-k_y plane, and find that the change is two, which corresponds to the two Weyl nodes at $(k_x, k_y, k_z) = (0, \pi, \pi), (\pi, 0, \pi)$ and . This evidences the topological non-triviality of the crossing points and the appearance of Weyl semimetallic phases.

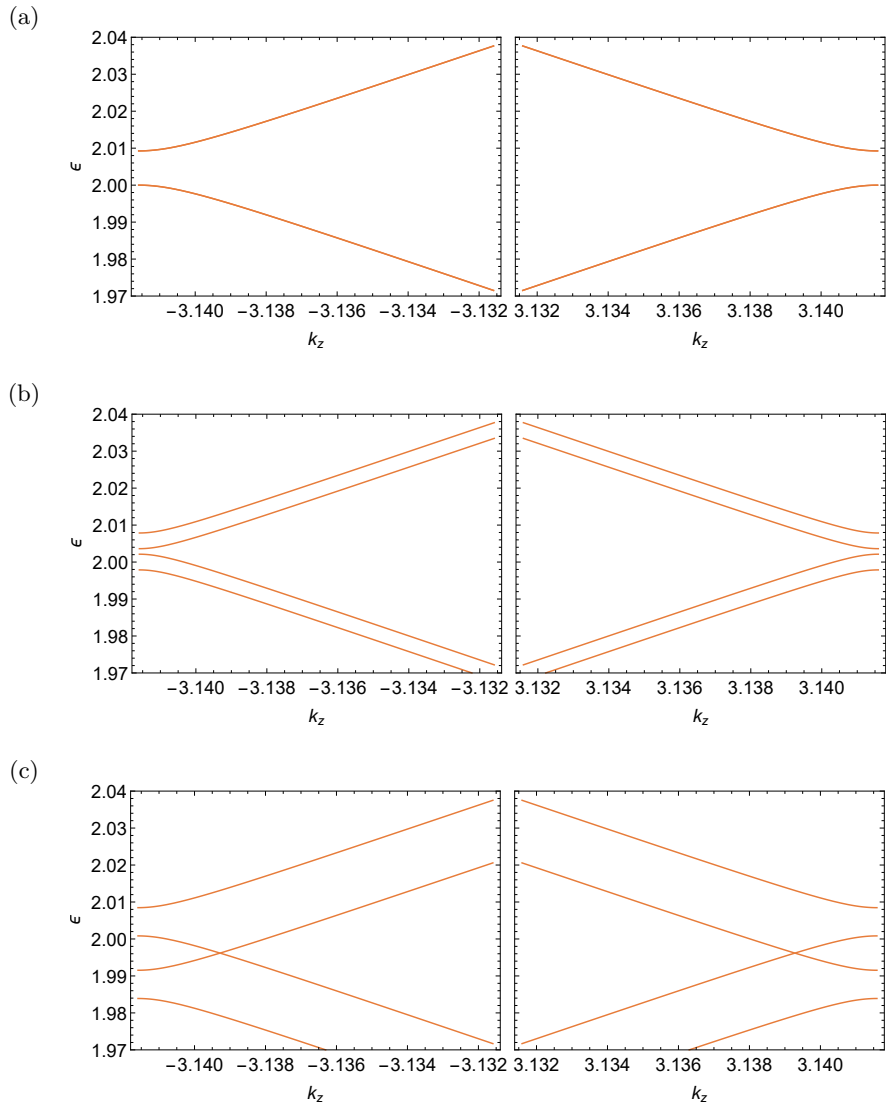

Figure 3.10: Laser-induced topological phase transition of the topological Kondo insulators with circularly polarized laser light. We show the calculated band structure for k_z ($(k_x, k_y) = (0, \pi)$) near the $k_z = \pm\pi$. (a) Without laser light ($A = 0.0$), the system is in the STI phase. (b) Applying the laser light ($A = 0.1$), the Kramers degeneracy is lifted and the bands are split by the LM. (c) Making the laser light stronger (A=0.2), the crossing points (Weyl nodes) appear near $k_z = \pm\pi$ and the system is changed to Weyl semimetallic phase Here we use the parameters as $T = 0.1$, $t_c = 1$, $t_f = -0.2$, $V = 1.5$, $\epsilon_f = -4$ and $\omega = 12.5$.

Next we calculate the Chern number for a broad range of (T, A) plane and obtain the phase diagram shown in Fig. 3.11 (a). We find four Weyl semimetallic phases, which have the Weyl nodes in different positions respectively. They are summarized in Fig. 3.11 (b). We can control the appearance of these Weyl semimetallic phases by changing the temperature and the intensity of the laser light.

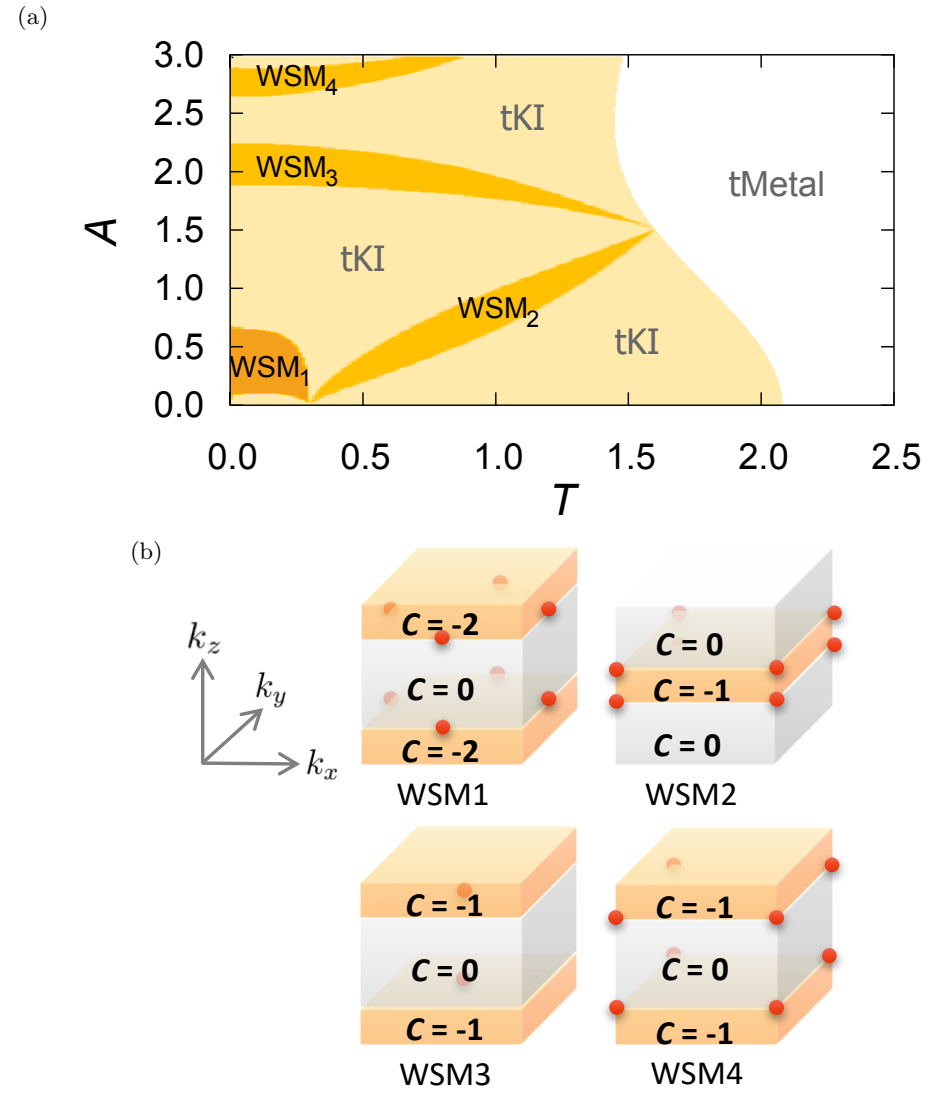

Figure 3.11: (a) The phase diagram of the topological Kondo insulators irradiated by circularly polarized laser light. There are two topologically trivial phases and four topologically non-trivial phases: the trivial Kondo insulator phase (tKI, $b \neq 0$, all the topological invariants are zero), the trivial metal phase (tMetal, $b = 0$), and four kinds of Weyl semimetallic phases (WSM_1, WSM_2, WSM_3 and WSM_4) shown in below. Here we use the parameters as $t_c = 1$, $t_f = -0.2$, $V = 1.5$, $\epsilon_f = -4$ and $\omega = 12.5$. (b) The four kinds of Weyl semimetallic phases. We show the position of the Weyl nodes (red points) in the three-dimensional Brillouin zone. The white (orange) regions represents the Chern number $C(k_z)$ is zero (finite).

We remark on two points about this phase diagram. One is that Weyl semimetallic phases are realized by relatively low intensity of laser light at the temperature near $T \sim 0.3$. The temperature $T \sim 0.3$ corresponds to the transition temperature from STI phase to WTI_2 phase in this model. Therefore, to find laser-induced Weyl semimetallic phase, the system near the topological phase transition is suitable. The other is that the Weyl semimetallic phases are extended with decreasing the temperature. It is because the LM, which is proportional to $|b|^2$, is enhanced in the low temperature region. This implies that the low temperature is better for observing Weyl semimetallic phases.

Finally we remark on the difference of our work from the previous ones that proposed the realization of Weyl semimetallic phases by laser light. There are several studies discussing the Weyl semimetallic phase realized by laser light using Floquet theory [53, 142–144]. However they are limited to the free electron systems. In our study, we consider the Kondo insulator, which is the strongly correlated insulator, and discuss the stability of the Kondo effect under laser light. We find that the Kondo effect is suppressed by laser light but there still exists the regime where the Kondo effect survives and the Weyl semimetallic phases can be stabilized. The application of laser light to the topological Kondo insulators is a promising way to realize the Weyl semimetals in heavy fermion systems [145].

3.6 Experimental setup

In the above sections, we have discussed the possibility to control the Kondo effect and the topological properties in Kondo insulators by laser light. In this section, we discuss the experimental setups to observe the phenomena proposed in this paper.

As for candidate materials, all the Kondo insulators are applicable to our proposal since our calculation is based on a simple model and the main results do not depend on the detail of models and approximations. There are several materials known as Kondo insulators, e.g. SmB_6 and CeNiSn [146]. They are our main targets. Moreover we expect that our results can be applicable to most of heavy fermion systems because the periodic Anderson model is a fundamental model of heavy fermion systems. The key ingredient for our proposal is that the system is at low temperature and the Kondo effect occurs. In this sense, other materials in heavy fermion systems, e.g. $CeCu_6$ and $CeCoIn_5$ [126], are also in the scope of our study. Note that, as for the results about topological properties discussed in Sec. 3.5, the system should be a topological Kondo insulator having the spin-dependent and off-site hybridization. Therefore, the candidate materials for topological Kondo insulators, e.g. SmB_6 [128] and YbB_{12} [147], are suitable to observe the laser-induced topological phase transitions. Regarding the sample, it should be a sufficiently thin slab, because laser light only penetrates into the thin region from the surface. How deep the laser light penetrates into the sample depends on materials and laser intensity, and thus we have to prepare an adequate sample to confirm our proposal. Moreover, the sample must be at low temperature below the Kondo temperature T_K, and therefore the application of laser light should be done in such low temperature regime.

The laser light is characterized by its frequency and intensity. Since our calculation is based on the high-frequency expansion, the frequency must be sufficiently high and off-resonant. Considering the energy scale in our models, frequency must be higher than the band width $12t$. Thus the ultraviolet light is suitable for our systems. In addition, in solid state systems, there are many unoccupied bands above Fermi energy, then we have to choose an appropriate frequency so as to make it off-resonant to any bands. If the frequency is not so high or the effect of resonance is crucial, the description by the effective Hamiltonian becomes worse. To access such a regime of frequency, we have to use different methods with which we can treat both the effect of low frequency and the interaction. In regard to the intensity of the laser light, we need a reasonably strong intensity according to the experimental accuracy and the phenomena which we want to observe. For example, looking at the phase diagram of the topological Kondo insulators with circularly polarized laser light in Fig. 3.11 (a), we can say that the laser intensity A higher than 0.1 is necessary to realized the Weyl semimetallic phase (WSM_1). The intensity $A \sim 0.1$ corresponds to the intensity of the electric field $E \sim 30$ MV/cm.

In experiments, we should use pulse laser with a finite width in time direction in order to

obtain strong intensity of laser light. In terms of the protocol of the application of laser light, we have to consider the following two conditions. (i) Too long laser pulse drives the interacting systems to infinite-temperature trivial states [82], and thus we need to choose a short laser pulse. In other words, we have to stop the driving before the system completely heats up [83]. (ii) It takes time to reach the states described by the effective Hamiltonian. Moreover, to realize the ground states of the effective Hamiltonian we have to switch on the driving adiabatically [44, 121]. Therefore we should use a long and slowly developing pulse. Taking into account these two conditions, we have to choose intermediate time scale adequately. In fact, it is possible to take such an intermediate time scale. Regarding the first condition, we can make the time before heating up longer using higher frequency of laser light [84]. Concerning the second condition, such a relaxation can happen in the femtosecond time scale in strongly correlated electron systems [122]. We should choose the pulse with sufficiently high frequency and with a longer width than the femtosecond time scale.

Finally, we address the experimental methods to confirm our proposal. As mentioned above, we should use the pulse laser and thus have to choose a method suitable for observing transient phenomena. Therefore transport or optical measurement is suitable. We explain how to observe the control of the Kondo effect and the topological phases respectively. As for the Kondo effect, discussed in Sec. 3.4, we have shown that laser light can enhance or suppress the Kondo temperature, resulting in the shift of the temperature where the Kondo crossover occurs. However, it is difficult to detect the shift itself since there is no singularity in the Kondo crossover. To observe this phenomenon clearly, we can utilize the quantum phase transition in terms of the Doniach phase diagram. As mentioned in the end of Sec. 3.4, the suppression or enhancement of Kondo effect changes the Kondo coupling and then the quantum phase transition occurs due to the competition between Kondo effect and RKKY interaction. The signature of this phase transition should be much more clear than the Kondo crossover. To find the signature of the phase transition by optical measurement, the pump-probe photoemission spectroscopy (PES) is the most promising way. We measure the system irradiated by the appropriate pump pulse, and then we can find the Kondo peak near the Fermi surface in the photoemission spectrum when the Kondo effect is dominant. On the other hand, the Kondo peak vanishes when the RKKY interaction is dominant. Therefore, performing the pump-probe PES with changing the laser intensity, we should find the appearance or vanishment of the Kondo peak when the system goes over the quantum critical point, which is the signature of the phase transition. Concerning the topological phases, the time-resolved and angle-resolved PES is the most promising experiment tool. If we find the change of the topological surface states, it evidences the topological phase transitions. The closing of the bulk gap is also a signature of the topological phase transitions. Applying linearly polarized laser light, we find the phase transitions from STI to WTI_2. In this phase transition, we should find the disappearance of the surface states on the (0,0,1) surface since ν^z_{WTI} changes from one to zero. In the case of the Weyl semimetallic phases realized by circularly polarized laser light, different Fermi-arc surface states are observed depending on which the Weyl semimetallic phases appear.

3.7 Summary of this chapter

In this chapter, we have derived the effective model of heavy fermion systems under high frequency laser fields with slave boson approach and Floquet theory. In the effective model, we have found two generic effects induced by laser light, dynamical localization and laser-induced hopping and hybridization. These effects change the original system and enable us to control its Kondo effect and topological properties. Regarding Kondo effect, we have found that we

can enhance or suppress the Kondo effect depending on the structure of the hybridization. As we discussed in the end of the Sec. 3.4, the enhancement and suppression of Kondo effect open a way to realize laser-induced quantum phase transitions. As for topological properties, we have found various topological phase transitions realizable in the topological Kondo insulators. With linearly polarized laser, the suppression of Kondo effect shifts the f-electron level and then induces the WTI phase which does not appear in the original model. Applying the circularly polarized laser light breaks the time-reversal symmetry and gives rise to the laser-induced synthetic magnetic fields, which creates the Weyl nodes in the band structure and realizes the Weyl semimetallic phases. Finally we have discussed the experimental setups to confirm our results. We have discussed the physics in the laser-irradiated heavy fermion systems and found several basic effects which change the original nature of the heavy fermion systems drastically. Our results opens a new possibility of dynamical controls in strongly correlated electron systems.

Chapter 4

Control of insulating magnets with DC electric fields

4.1 Introduction

In this chapter, we present our theoretical proposal for controlling insulating magnets with DC electric fields. As explained in Chap. 1, dynamical controls with AC and DC electric fields have been gathering great attention in recent years. Particularly, plenty of interesting scenarios with AC electric fields or laser light have been proposed (e.g. light-induced superconductivity [1, 23], Floquet topological insulator [2, 45, 80], ultrafast spintronics [56, 58]). The control with low-frequency or DC (static) electric fields has been also studied (e.g. electric-field-controlled magnetism in multiferroics [148–153] and dielectric breakdown in Mott insulators [6, 34, 35, 38, 154, 155]), but varieties of DC-field driven phenomena have been still limited compared with AC-field studies. DC fields usually do not make the system heated, while it is difficult to avoid heating effects in AC-field driven systems. This is a significant advantage of the DC-field study. Moreover, in recent years, experimental ways of generating strong DC electric fields (e.g., order of 1-10 MV/cm) have been developed by using several techniques based on, for example, field-effect transistors [156, 157] and nano-scale needles [158]. The technology of low-frequency AC fields has also been developed and for instance we can use terahertz (THz) laser pulses whose intensity is of the order of 1-10 MV/cm [159, 160]. Novel proposals for DC-field and low-frequency AC-field driven phenomena thereby are being anticipated.

Stimulated by this situation, we propose a new scheme to control magnetic or topological orders in Mott insulators by DC electric fields. We consider quantum magnets of Mott insulators in the presence of DC electric fields as shown in Fig. 4.1 (a). In this setup, we derive the low-energy effective spin models by applying the strong-coupling expansion, and show that exchange interactions along the DC-field direction are generally increased with the growth of the field strength. A strong electric field comparable to Mott gap is usually necessary for realizing Mott breakdown, while our proposal indicates that quantum magnetic nature can be changed with smaller DC fields in Mott insulators [1]. We show that various quantum states such as quantum spin liquids (QSLs) [93, 94, 161] and Haldane-gap states [95, 162] can be created/annihilated by applying strong DC electric fields to representative frustrated or quasi-one-dimensional (quasi-1D) magnets.

[1] In other words, there are no macroscopic current. Thus, strictly speaking, this phenomenon happens in *equilibrium*. However, enhancement of the exchange coupling, which is a key idea in this proposal, occurs with slow AC fields (e.g. THz fields) as shown in Ref. [167]. Thus, our proposal can be realized in a time-dependent way (i.e. nonequilibrium) and should be useful for dynamical controls of magnetism.

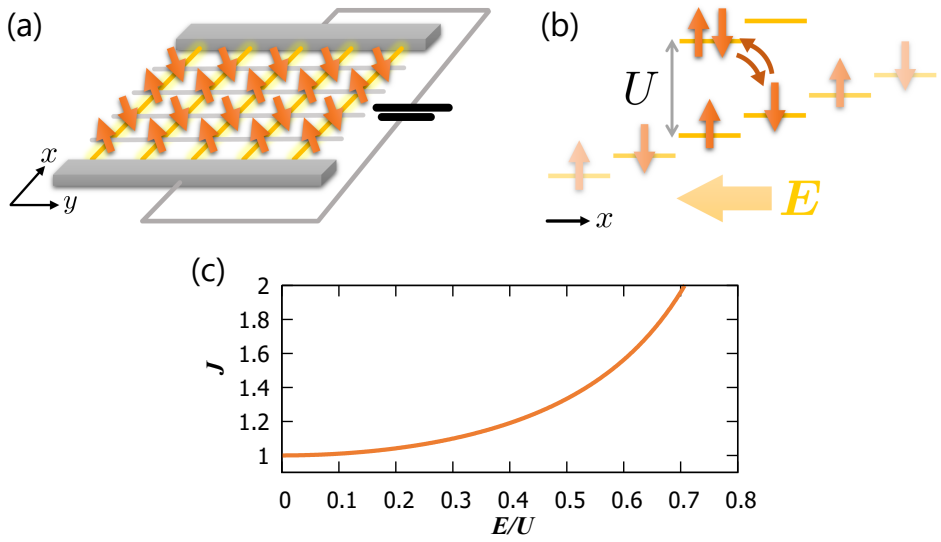

Figure 4.1: (a) Our setup of a Mott insulator under DC electric fields $\boldsymbol{E}$ along the x-direction. (b) Spatial energy level structure of the DC-field driven Mott insulator. Arrows denote the second-order virtual hopping process in the Mott state. (c) Electric-field dependence of the exchange coupling along the x-direction in the Mott system (b) [see Eq. (4.2)].

This chapter is organized as follows. In Sec. 4.2, we show that DC electric fields enhance the exchange interaction between spins based on the perturbation theory. Utilizing this enhancement, it is possible to control various phases of matter with changing spatial structure of magnetic interactions. To demonstrate the usefulness of this scheme, we explain the controls in two classes of spin systems, frustrated spin systems and quasi-1D spin systems, where our scheme works quite well. Controls of frustrated spin systems and quasi-1D spin systems are explained in Sec. 4.3 and Sec. 4.4 respectively. Finally, we summarize our results in Sec. 4.5.

4.2 Enhancement of the exchange coupling

To show how the exchange interaction is modified by DC electric fields, we first consider a generic half-filled, single-band Hubbard model subject to static electric fields $\boldsymbol{E}$. The effect of electric fields is introduced as an on-site potential and the Hamiltonian is given by

$$\mathcal{H} = \sum_{\boldsymbol{r}\boldsymbol{r}'\sigma} t_{\boldsymbol{r}\boldsymbol{r}'} c^{\dagger}_{\boldsymbol{r}\sigma} c_{\boldsymbol{r}'\sigma} + U \sum_{\boldsymbol{r}} n_{\boldsymbol{r}\uparrow} n_{\boldsymbol{r}\downarrow} + \sum_{\boldsymbol{r}\sigma} V_{\boldsymbol{r}} n_{\boldsymbol{r}\sigma}, \tag{4.1}$$

where $c_{\boldsymbol{r}\sigma}$ is a spin-σ electron annihilation operator ($\sigma = \uparrow, \downarrow$) on a site $\boldsymbol{r} = (i, j, k)$, and $n_{\boldsymbol{r}\sigma} = c^{\dagger}_{\boldsymbol{r}\sigma} c_{\boldsymbol{r}\sigma}$ (the lattice constant is set to be unity). The first and second terms respectively stand for hopping and on-site Coulomb repulsion, and the on-site potential $V_{\boldsymbol{r}}$ represents the effect of the applied electric field. For example, $V_{\boldsymbol{r}}$ is reduced to $V_i = i|\boldsymbol{E}| = iE$ when the electric field is parallel to the x-axis [2]. If the Coulomb repulsion $U > 0$ is strong enough at half filling, a Mott insulator is realized and we can derive its low-energy effective spin model by treating the kinetic term as a perturbation (large U expansion). The point is that the second-order virtual hopping amplitude becomes direction-dependent due to the field-driven

[2] Strictly speaking, we should take into account the dielectric constant ϵ defined for each material. In other words, the electric field $\boldsymbol{E}$ used here is $D = \epsilon E$.

potential $V_{\boldsymbol{r}}$ as shown in Fig. 4.1 (b). As a result, the exchange interaction becomes spatially anisotropic and the effective Hamiltonian in the second-order perturbation is given by

$$\mathcal{H}_{\text{eff}} = \sum_{\langle \boldsymbol{r},\boldsymbol{r}'\rangle} \frac{J_{\boldsymbol{r}\boldsymbol{r}'}}{1-\left(\frac{\Delta V_{\boldsymbol{r}\boldsymbol{r}'}}{U}\right)^2} \boldsymbol{S}_{\boldsymbol{r}} \cdot \boldsymbol{S}_{\boldsymbol{r}'}, \tag{4.2}$$

where $\boldsymbol{S}_{\boldsymbol{r}}$ is the electron spin operator on a site $\boldsymbol{r}$, $J_{\boldsymbol{r}\boldsymbol{r}'} = 4|t_{\boldsymbol{r}\boldsymbol{r}'}|^2/U$ and $\Delta V_{\boldsymbol{r}\boldsymbol{r}'} = V_{\boldsymbol{r}} - V_{\boldsymbol{r}'}$. The summation is taken over all the bonds $\langle \boldsymbol{r}, \boldsymbol{r}'\rangle$. The perturbation expansion would be valid if the on-site potential energy is smaller than the Mott gap [3]. If a similar strategy of the perturbation theory is applied to a half-filled two-orbital Hubbard model, we obtain the following spin-1 AFM Heisenberg model

$$\mathcal{H}_{\text{eff}} = \sum_{\langle \boldsymbol{r},\boldsymbol{r}'\rangle} \frac{J'_{\boldsymbol{r}\boldsymbol{r}'}}{1-\left(\frac{\Delta V_{\boldsymbol{r}\boldsymbol{r}'}}{U+J_H}\right)^2} \boldsymbol{S}_{\boldsymbol{r}} \cdot \boldsymbol{S}_{\boldsymbol{r}'}, \tag{4.3}$$

where $\boldsymbol{S}_{\boldsymbol{r}}$ is the spin-1 operator on a site $\boldsymbol{r}$, $J'_{\boldsymbol{r}\boldsymbol{r}'} = 2|t_{\boldsymbol{r}\boldsymbol{r}'}|^2/(U+J_H)$ and J_H is the strength of the Hund's coupling. The derivations of the above effective models (4.2) and (4.3) are given in Appendix B.

The above results and the physical picture in Fig. 4.1 (b) clearly indicate that antiferromagnetic (AFM) exchange couplings are generally enhanced by the DC electric field in a quite wide class of Mott insulators [4]. For example, if we focus on a bond $\langle \boldsymbol{r}_1, \boldsymbol{r}_2\rangle$ parallel to the electric-field direction, the potential difference $\Delta V_{\boldsymbol{r}_1\boldsymbol{r}_2}$ is given by $E|\boldsymbol{r}_1 - \boldsymbol{r}_2|$. Thereby in the spin-$\frac{1}{2}$ case, the exchange coupling on the nearest-neighboring bond is computed as $J/(1-(E/U)^2)$ with $J = 4t^2/U$ being the exchange coupling in the original Hubbard model without the potential $V_{\boldsymbol{r}}$. This effective exchange coupling is shown in Fig. 4.1 (c).

On the basis of the above perturbation theory, we show how magnetic properties of Mott insulators can be controlled by DC electric fields. For instance, Mott insulators whose U is relatively large but still $t/U \ll 1$ (e.g. organic Mott insulators) are expected to be relevant since E/U becomes relatively large. In addition, magnets residing near a transition point between two magnetic phases are also expected to be quite relevant since their phases are unstable against small changes of magnetic interactions. In the following sections, we demonstrate below that several magnetic or topological orders can be created/annihilated in typical frustrated magnets (Sec. 4.3) and quasi-1D magnets (Sec. 4.4), by tuning the strength and direction of DC fields.

Before closing this section, we give several remarks on the above results.

(i) *Higher-order spin interactions*
The higher-order corrections such as ring exchange terms and biquadratic terms [164–166] should appear approaching the weak coupling regime, i.e. t/U is large. They can also be straightforwardly computed based on our approach shown in Appendix B. In general, they are much smaller than the exchange coupling, but can give significant effects on magnetic orders in some specific cases. We leave the calculation of the higher order correction to the exchange interaction as an interesting future work.

(ii) *Low-frequency AC fields*
We stress that both the effective models (4.2) and (4.3) could be relevant even in a short time period when a sufficiently low frequency AC electric field (e.g. THz laser pulse) is

[3] About detailed conditions needed for our perturbation expansion, see Sec. B.3 in Appendix B.

[4] DC-field driven modifications of exchange couplings have been pointed out in a few specific systems [163]. However, we stress that our present results could be applied in a generic class of Mott insulators

applied to the Mott insulators instead of DC fields [5]. Note that the heating effect by THz laser would be much smaller than those of high-frequency AC fields since electrical dipole transitions beyond the Mott gap are negligible in the application of THz laser [12].

(iii) *Effect on spin-orbit (SO) couplings*
Here we do not consider the effect of breaking inversion symmetry by applying electric fields. Due to this effect, SO couplings can be changed by DC electric fields on top of exchange couplings [170–172]. However, their strength would strongly depend on the details of atomic wave functions and lattice structures. The main purpose of this study is to propose new schemes applicable to a wide range of insulating magnets. Therefore, we leave the study of this effect as a future study.

(iv) *Application to cold atomic systems*
The scope of our theory is not limited to solid state systems. Our results are also applicable to Mott insulators in ultracold atoms on optical lattices [173]. Tilting optical-lattice potentials, which is already realized in experiments, plays the same role as the DC field in solid systems [174–180]. For instance, the tilt enhances the exchange interaction and thus would be useful for realizing/controlling an AFM long range order in cold atoms [173, 181].

4.3 Control of frustrated magnets

In frustrated magnets, spatial structures of magnetic interactions determine their magnetic orders, and the modification of the spatial structures with DC electric fields enables us to change the orders. Namely, frustrated magnets are expected to give one of the best stages for electric-field control of magnetism.

First, we consider a spin-$\frac{1}{2}$ AFM Heisenberg model on a triangular lattice as a typical frustrated magnet. If we apply DC fields to a spatially-isotropic Mott insulating triangular magnet, the spin Hamiltonian is given as

$$\mathcal{H}_{\rm tri} = \sum_{\boldsymbol{r}} \sum_{k=1}^{3} J_k(E,\theta_E) \boldsymbol{S}_{\boldsymbol{r}} \cdot \boldsymbol{S}_{\boldsymbol{r}+\boldsymbol{a}_k}. \tag{4.4}$$

Here the vector $\boldsymbol{r}$ denotes a site on the triangular lattice, and primitive translation vectors $\boldsymbol{a}_{1,2,3}$ are given by $\boldsymbol{a}_1 = (1,0)$, $\boldsymbol{a}_2 = (-1/2, \sqrt{3}/2)$ and $\boldsymbol{a}_3 = \boldsymbol{a}_1 + \boldsymbol{a}_2$ (shown in Fig. 4.2 (b)). The direction of the applied DC field $\boldsymbol{E}$ is controlled with the angle θ_E as in Fig. 4.2 (a). The parameter J_k represents the strength of the exchange coupling parallel to $\boldsymbol{a}_k$ ($k = 1, 2, 3$) and their E dependence is computed as $J_1(E,\theta_E) = J/[1 - \{E\cos\theta_E/U\}^2]$, $J_2(E,\theta_E) = J/[1-\{E\cos(\theta_E - 2\pi/3)/U\}^2]$, and $J_3(E,\theta_E) = J/[1-\{E\cos(\theta_E - \pi/3)/U\}^2]$ with $J = 4t^2/U$. E-dependence of them are shown in Fig. 4.2 (g). Without electric fields ($E = 0$), the ground state of this model is a commensurate 120° structure (shown in Fig. 4.2 (b)) [182–184]. When a field $\boldsymbol{E}$ is applied, the exchange coupling becomes anisotropic, and an incommensurate spiral order would emerge. From the simple calculation of the classical ground state energy, we can determine the pitch angle of the incommensurate state as a function of $E(= |\boldsymbol{E}|)$ and θ_E. Figure 4.2 (b) depicts the pitch angle $\theta_{1(2)}$ that is defined as the difference between two neighboring spins' angle on the bond along the $\boldsymbol{a}_{1(2)}$ direction. As shown in Fig. 4.2 (d) and (e), if θ_E is locked to zero ($\pi/2$), the one dimensionality is enhanced (the system is gradually

[5] AC-field control of the exchange coupling has been discussed [64, 66, 67, 167–169] and the DC limit of Ref. [167] is consistent with one of our results (4.2). We however stress that our results are more generic and our approach can be straightforwardly extended to a generic class of Mott insulators.

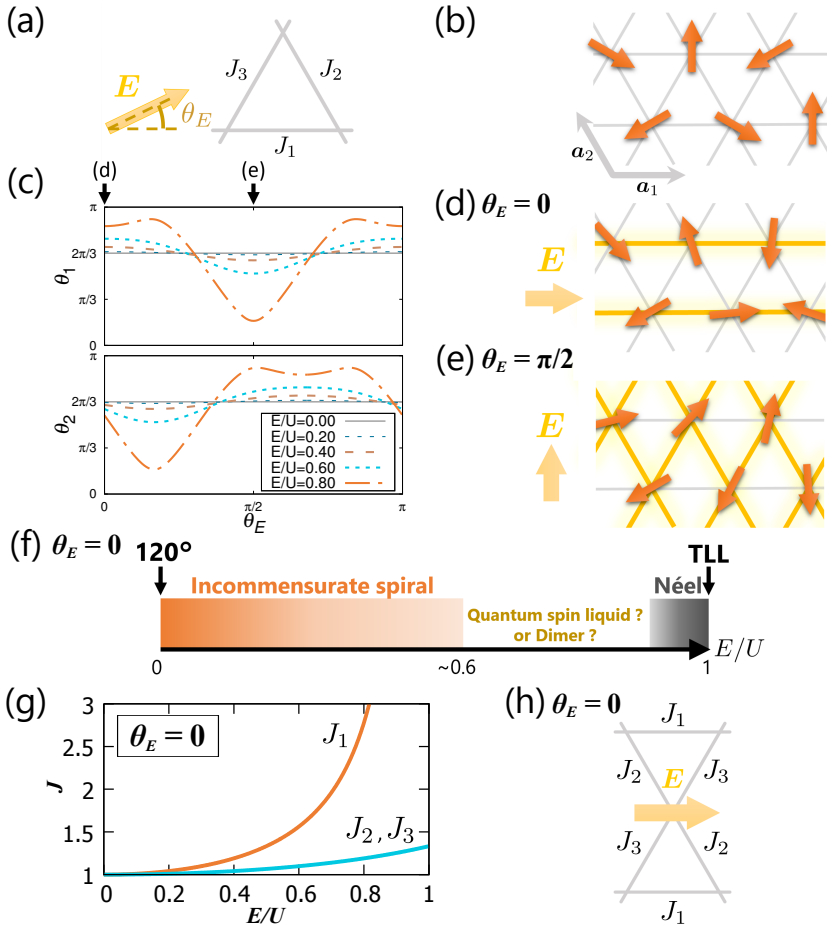

Figure 4.2: (a) Exchange couplings $J_{1,2,3}$ in a triangular lattice and the angle θ_E of the DC electric field $\boldsymbol{E}$. (b) 120° structure, which is the ground state of the triangular AFM Heisnberg model. (c) $\boldsymbol{E}$ dependence of pitch angles θ_1 and θ_2 in the spiral ordered phase of the triangular AFM model (4.4) in a DC electric field. (d, e) Typical spin configurations in the $\boldsymbol{E}$-driven spiral ordered phases for (d) $\theta_E = 0$ and (e) $\pi/2$. (f) Ground-state phase diagram of the triangular spin-$\frac{1}{2}$ AFM Heisenberg model in a DC electric filed ($\theta_E = 0$). (g) $\boldsymbol{E}$ dependence of the exchange couplings $J_{1,2,3}$ in the model (4.4). (h) Exchange couplings $J_{1,2,3}$ in a Kagomé lattice magnet with a DC electric field $\boldsymbol{E}$.

changed into a square lattice system). These results clearly indicate that the spiral order pattern can be controlled by electric fields smaller than the critical value of the Mott breakdown.

If we focus on the case of $\theta_E = 0$, the system is a spin-$\frac{1}{2}$ anisotropic triangular lattice model with $J_2 = J_3$, and it has been well studied both theoretically and experimentally [94]. Some previous studies [185–189] show that the spiral order is preserved at least up to $J_2/J_1 \sim 0.6$ when J_1 is increased with E. On the other hand, a reliable approach based on 1D quantum field theory shows that a Néel order should appear near the anisotropic limit ($J_2/J_1 \to 0$) [190]. At the point of $J_2 = 0$, the system is reduced to decoupled 1D Heisenberg chains and a Tomonaga-Luttinger liquid (TLL) phase appears. The quantum phases between spiral and Néel orders are still under debate, but it is predicted to be a QSL [186–189]. Combining these results with the E dependence of J_2/J_1, we obtain the ground-state phase diagram under the electric field $\boldsymbol{E}$ with $\theta_E = 0$, as shown in Fig. 4.2 (f). Note that the end point of the Néel order has never been theoretically determined.

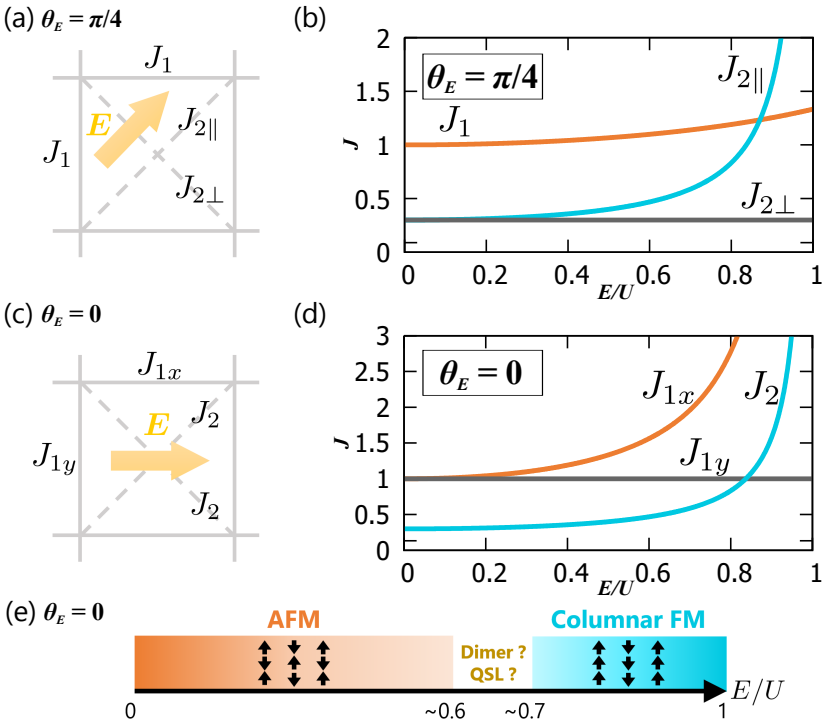

Figure 4.3: (a, c) Exchange couplings in DC-field driven J_1-J_2 square-lattice magnets for (a) $\theta_E = \pi/4$ and (c) $\theta_E = 0$. In the case of $\theta_E = \pi/4$ (0), J_2 (J_1) is changed into $J_{2\parallel}$ and $J_{2\perp}$ (J_{1x} and J_{1y}). (b, d) $\boldsymbol{E}$ dependence of the exchange couplings in the case of (b) $\theta_E = \pi/4$ and (d) $\theta_E = 0$. (e) Ground-state phase diagram of the AFM spin-$\frac{1}{2}$ Heisenberg model on a J_1-J_2 square lattice in DC electric fields ($\theta_E = 0$). In Panels (b), (d), and (e), we set $J_2/J_1 = 0.3$ at $E = 0$.

Our approach indicates that a sufficiently strong electric field $E/U \sim 0.6 = E_c/U$ is necessary for the phase transiton to a QSL state if we start from the isotropic point $J_{1,2,3} = J$ at $\boldsymbol{E} = \boldsymbol{0}$. The value of E_c is estimated as ~ 5 MV/cm if we consider a typical organic triangular magnet with lattice constant 10 Å and $U = 0.8$ eV, e.g. $(ET)_2Cu(NCS)_2$ [191, 192] and $(ET)_2Cu_2(CN)_3$ [192–194]. However, many of organic triangular Mott insulators deviate from the isotropic point and thus smaller field is enough to realize the field-induced transition. For instance, we have $E_c \sim 0.9$ MV/cm for a spatially anisotropic triangular magnet with $J_{2,3}/J_1 = (J_2/J_1)_c \times 1.01$.

In addition to the triangular lattice system, here we give a few remarks on the Kagomé lattice magnets. One sees from Fig. 4.2 (h) that if we apply an electric field to a spatially isotropic Kagomé Mott insulator, three kinds of exchange couplings $J_{1,2,3}$ appear. The $\boldsymbol{E}$ dependence of $J_{1,2,3}$ is completely same as that of the triangular lattice. Our method provides a way of generating anisotropic Kagomé lattices.

Next, we turn to the spin-$\frac{1}{2}$ J_1-J_2 magnet on a square lattice. This model is another representative of 2D frustrated systems and has been long studied [195–201]. We calculate how the exchange couplings are modified by an electric field parallel to a J_1 (J_2) bond, as shown in Fig. 4.3 (a)-(d). In the case of $\boldsymbol{E}$ parallel to the J_{1x} bond ($\theta_E = 0$), one dimensionality is enhanced along the J_{1x} bond direction, and the system approaches to a quasi-1D magnet with frustrated inter-chain interactions J_{1y} and J_2. This system has been theoretically studied and it is known that a dimer order or (Z_2) QSL state appears when the frustration between two inter-chain couplings J_{1y} and J_2 is quite strong [195, 200, 201]. Therefore, we can draw the ground-

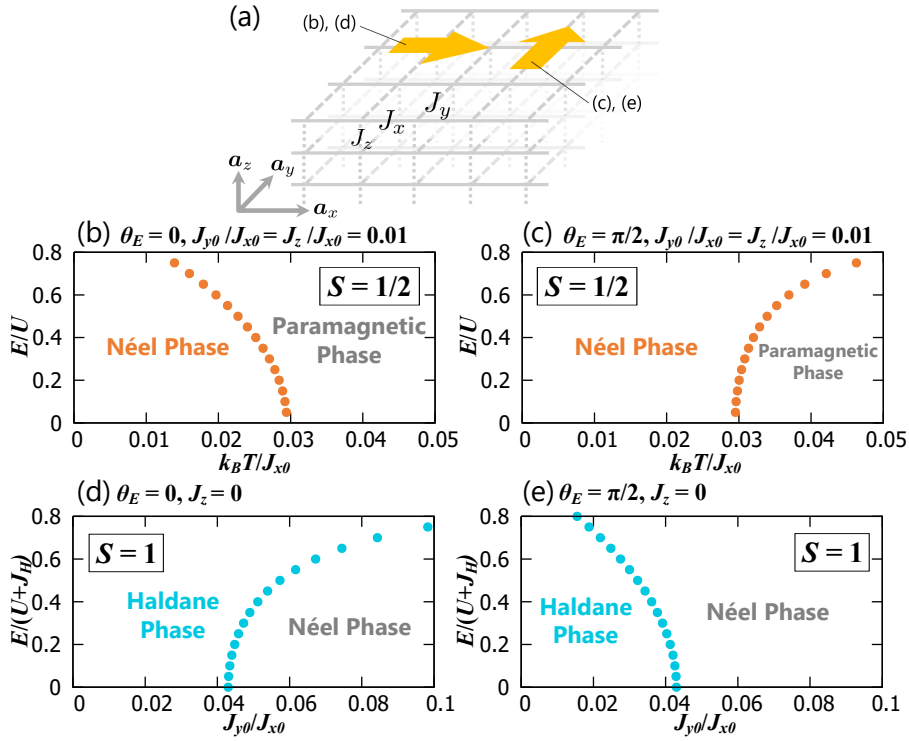

Figure 4.4: (a) Lattice structure of the quasi-one-dimensional AFM Heisenberg magnet consisting of weakly coupled 1D Heisenberg chain. Yellow arrows denote the direction of the applied DC electric field. (b-e) Phase diagrams of quasi-1D AFM Heisenberg model subject to DC electric fields. Panels (b, c) and (d, e) respectively correspond to the spin-$\frac{1}{2}$ and spin-1 results. The electric field $\boldsymbol{E}$ is parallel to the chain ($\boldsymbol{E} \parallel \boldsymbol{a}_x$) in the cases (b,d), while $\boldsymbol{E}$ is perpendicular to the chain ($\boldsymbol{E} \parallel \boldsymbol{a}_y$) in the cases (c,e).

state phase diagram under an electric field as in Fig. 4.3 (e). Namely, a sufficiently strong electric field is expected to create a QSL state as in the case of the triangular lattice. In the case of $\theta_E = \pi/4$, the system approaches to a triangular AFM Heisenberg model with an additional interaction $J_{2\perp}$. Layered vanadium oxides such as $PbVO_2$ [198, 199] or $VOMoO_4$ [196] and double perovskite oxides such as Sr_2CuTeO_6 [202] are good candidate materials for the J_1-J_2 magnet. They have a relatively large value of J_2/J_1 and thus a small electric field can make the Néel state change into dimer or QSL states.

4.4 Control of quasi-one-dimensional magnets

Purely 1D magnets do not show any magnetic orders even at low temperature due to strong fluctuation effects [203–206]. However, in a broad class of quasi-1D magnets, a magnetically ordered phase generally appears due to a weak but finite three dimensionality if temperature is sufficiently low.

When the electric field is parallel to the chain direction, the one dimensionality is further enhanced and an exotic quantum phase should appear. On the other hand, an electric field perpendicular to the chain makes the inter-chain coupling stronger and the system is expected to show a magnetic long-range order. To demonstrate our proposal, we analyze an AFM Heisenberg model on a cubic lattice consisting of weakly coupled spin chains, which is depicted in Fig. 4.4 (a). In this model, the spin chains are parallel to the x direction, a DC electric field

$\boldsymbol{E}$ is in the x-y plane, and the direction of $\boldsymbol{E}$ is defined by the angle θ_E. In this setup, the spin Hamiltonian is written as

$$\mathcal{H} = \sum_{\boldsymbol{r}} [J_x(E,\theta_E)\boldsymbol{S}_{\boldsymbol{r}} \cdot \boldsymbol{S}_{\boldsymbol{r}+\boldsymbol{a}_x} + J_y(E,\theta_E)\boldsymbol{S}_{\boldsymbol{r}} \cdot \boldsymbol{S}_{\boldsymbol{r}+\boldsymbol{a}_y}] + \sum_{\boldsymbol{r}} J_z \boldsymbol{S}_{\boldsymbol{r}} \cdot \boldsymbol{S}_{\boldsymbol{r}+\boldsymbol{a}_z}. \tag{4.5}$$

For the spin-$\frac{1}{2}$ case, the exchange couplings in the x and y directions are respectively given by $J_x(E,\theta_E) = J_{x0}/[1-\{E\cos\theta_E/U\}^2]$, $J_y(E,\theta_E) = J_{y0}/[1-\{E\cos(\theta_E-\pi/2)/U\}^2]$, and J_z is that in the z direction. For the spin-1 case, the above formulas of the exchange couplings are modified by the replacement $U \to U + J_H$.

In the spin-$\frac{1}{2}$ system, if temperature becomes low enough (typically, order of inter-chain couplings), a Néel ordered phase emerges. In general, various sorts of finite-temperature phase transition points in quasi-1D systems can be determined by applying the chain mean field theory (MFT) [207–213]. In fact, the transition points predicted by chain MFT agree well with experimental results of some quasi-1D magnets [211, 212]. We apply the chain MFT to the present spin-$\frac{1}{2}$ system and the resultant phase diagrams on the plane (k_BT, E) are summarized in Fig. 4.4 (b) and (c). The detail of the chain MFT is explained in Appendix C. The phase diagrams show that when $\boldsymbol{E}$ is parallel to the x (y) direction, the one dimensionality is enhanced (inter-chain interaction becomes stronger) and the transition temperature decreases (grows) with increasing E.

For the spin-1 case, the so-called Haldane phase, a typical symmetry-protected-topological phase, is realized in each spin-1 AFM chain in a parameter range with small inter-chain couplings, while a Néel ordered phase takes place when inter-chain couplings are strong enough. The low-energy properties of the quasi-1D spin-1 system have been accurately investigated [214–216] and a quantum Monte Carlo simulation [214] shows the quantum phase transition between Haldane and Néel phases is located at $J_y(E,\theta_E) \simeq 0.043 J_x(E,\theta_E)$ for the 2D limit with $J_z = 0$. Using this relation, we can generally determine the ground-state phase diagram of the spatially anisotropic 2D spin-1 magnets under an electirc field $\boldsymbol{E}$. Figure 4.4 (d) and (e) are respectively the phase diagrams for $\boldsymbol{E} \parallel \boldsymbol{a}_x$ ($\theta_E = 0$) and $\boldsymbol{E} \parallel \boldsymbol{a}_y$ ($\theta_E = \pi/2$). The results of Fig. 4.4 clearly indicate that we can create/annihilate ordered or topological phases of quasi-1D magnets with a sufficiently strong DC electric field.

Our predictions of Fig. 4.4 are generally relevant to a wide class of quasi-1D magnets. For example, Sr_2CuO_3 [217], Cs_2CuCl_4 [218, 219], $KCuF_3$ [220] and NMP-TCNQ [221] (NENP [222, 223] , TMNIN [224] and Y_2BaNiO_5 [225, 226]) are well known as typical quasi-1D spin-$\frac{1}{2}$ (spin-1) magnets. Particularly, the Coulomb interaction of NMP-TCNQ has been estimated as a rather small $U \sim 0.17$eV [221]. For this magnet, Fig. 4.4(c) predicts that the critical temperature can increase by about 50% if we apply DC fields $E^{\parallel} \sim 0.8$MV/cm along the interchain direction with a lattice constant $\sim 15\mathring{A}$.

4.5 Summary of this chapter

In this chapter, we have shown that DC electric fields can enhance the AFM Heisenberg coupling in general Mott insulators (See Eqs. (4.2) and (4.3)). Then we have illustrated that this enhancement is very useful for controlling the phases of magnets, and given rich phase diagrams (See Figs. 4.2-4.4). We emphasize that a weaker DC field than that for the Mott breakdown is sufficient to control the magnetism, and our method is basically free from heating issues in contrast with the AC-field control.

Chapter 5

Conclusion and Future Perspectives

In this thesis, we have shown our theoretical proposals for controlling states of matter with electric fields. In Chap. 2 and 3, we have presented proposals related to AC electric fields (laser light). In Chap. 2, it has been shown that circularly polarized laser light can induce topological superconductivity whose realization in solids is still limited. In Chap. 3, we have discussed the behavior of heavy fermion systems under laser light and shown that we can control magnetic orders and topological phases. In contrast, we have discussed the control via DC electric fields in Chap. 4. We have considered insulating magnets under DC-fields and shown that interaction between spins can be enhanced with applying electric fields. Utilizing this enhancement, we have proposed experimental schemes for controlling frustrated magnets and quasi-one-dimensional magnets. In each chapter, we have discussed parameters and setups for experimental realizations respectively.

Finally, we explain our possible future perspectives. We have given several proposals as presented in this thesis, but the scope of our proposals are still limited to very simple cases. Therefore, there are many possibilities to extend our studies. We mention three possibilities below.

(i) *Low frequency regime*

Our calculations in Chap. 2 and 3 are based on the high-frequency expansion of the effective Hamiltonian. Therefore, our results are limited to the high frequency regime. Although several findings in our studies are expected to be unchanged even in the different frequency regime, our calculations cannot be applied to the low-frequency regime directly. However, many experiments have been done with relatively low-frequency laser light, e.g. (mid-)IR or THz laser. Therefore, it is important to explore the low-frequency regime for comparing theoretical results with experiments. For this purpose, we think that Floquet DMFT approach [227] is most promising. In this approach, combination of nonequilibirum DMFT and Floquet theory enables us to analyze nonequilibrium steady states realized in driven-dissipative systems. One of the advantages of this approach is that the frequency is not limited to high-frequency since we do not use a perturbative expansion in $1/\omega$. Using this approach, we can extend our results in Chap. 2 and 3 to the low-frequency regime and expect to observe different behaviors. The other advantage is that we can treat the effect of dissipation (e.g. phonon bath) in a natural way since we have to consider the model with thermal bath for realizing the steady state. This effect is also omitted in our treatment in Chap. 2 and 3. Thus, the extension in this direction is an important future task.

(ii) *Current-carrying states*

In Chap. 4, we have discussed the behavior of magnets under DC electric fields. However, the magnets are still macroscopically insulating. On the other hand, recent experiments suggest that there can emerge interesting phenomena in current-carrying nonequilibrium steady states under DC-fields, e.g. current-induced diamagnetism [6]. Thus, studies of current-carrying states are highly desired, but theoretical treatments of such states are difficult in general. One possible way to tackle this problem is to use strong numerical approaches such as nonequilibrium DMFT or time-dependent DMRG menitoned in Sec. 1.4. Using them, several authors have tried to understand the current-carrying states [35, 155, 228, 229], but their results are not conclusive. The other way is to use some effective models. There are in-coming and out-going electrons in this nonequilibrum steady states, and thus it may be possible to use non-Hermitian Hamiltonians used as effective models of open quantum systems. Indeed, a non-Hermitian variant of the Hubbard model is proposed as an effective model for dielectric breakdown in Mott insulators [154]. Application of this model to current-carrying states is one of the promising approaches.

(iii) *Combination with ab initio calculations*

Through this thesis, we have used simplified models because they are sufficient for our purpose to demonstrate new scenarios never discussed. However, it is very important to use more complicated models containing the information of specific materials for the purpose of experimental realizations. To obtain such models, one of the most promising ways is to use first-principle (*ab initio*) calculations. Applying Floquet theory to models based on such calculations, it should be possible to discuss the nature of laser-illuminated specific materials. The studies in this direction is still limited [230], but we expect that it will become important in future when the experimental techniques are more developed.

Appendix A

Derivation of the self-consistent equations with slave boson approach

In this Appendix, we show how to obtain the self-consistent equations (3.3) and (3.4) in Chap. 3. These equations which determine b and λ are derived with slave boson approach. In this approach, to treat the correlation effect in f-orbit, the slave particle operator b_i is introduced as

$$f_{i\sigma}^{\dagger} \to f_{i\sigma}^{\dagger} b_i, \tag{A.1}$$

$$f_{i\sigma} \to f_{i\sigma} b_i^{\dagger}, \tag{A.2}$$

with the constraint,

$$f_{i\uparrow}^{\dagger} f_{i\uparrow} + f_{i\downarrow}^{\dagger} f_{i\downarrow} + b_i^{\dagger} b_i = 1. \tag{A.3}$$

b_i ($b_i^{\dagger}$) is an annihilation (creation) operator of slave bosons, which corresponds to the creation (annihilation) of the holon, i.e. vacancy. The constraint (A.3) represents the strong coupling limit $U \to \infty$, in which the double occupancy is completely suppressed.

With these expressions, we write down the Lagrangian corresponding to the periodic Anderson model. The constraint is taken into account with the method of Lagrange multiplier. The Lagrangian reads

$$\begin{aligned}
\mathcal{L} =& \sum_{ij\sigma} \{\delta_{ij}(\partial_\tau - \mu) + t_{c,ij}\} c_{i\sigma}^{\dagger}(\tau) c_{j\sigma}(\tau) \\
&+ \sum_{i\sigma} \{\partial_\tau - \mu + \epsilon_f + i\lambda_i(\tau)\} f_{i\sigma}^{\dagger}(\tau) f_{i\sigma}(\tau) + \sum_{ij\sigma} t_{f,ij} f_{i\sigma}^{\dagger}(\tau) b_i(\tau) b_j^{\dagger}(\tau) f_{j\sigma}(\tau) \\
&+ \frac{1}{\sqrt{N}} \sum_{ij\sigma\sigma'} \{V_{ij\sigma\sigma'} c_{i\sigma}^{\dagger}(\tau) b_j^{\dagger}(\tau) f_{j\sigma'}(\tau) + \text{h.c.}\} + i \sum_{\boldsymbol{i}} \lambda_i(\tau) \{b_i^{\dagger}(\tau) b_i(\tau) - 1\},
\end{aligned} \tag{A.4}$$

where $\lambda_i(\tau)$ is the Lagrange multiplier field. Next we take mean-field approximation i.e. $b_i(\tau) \to b(\tau), i\lambda_i(\tau) \to \lambda(\tau)$ and then we obtain the mean-field Lagrangian $\mathcal{L}_{\text{MF}}$ as

$$\begin{aligned}
\mathcal{L}_{\text{MF}} =& \sum_{ij\sigma} \{\delta_{ij}(\partial_\tau - \mu) + t_{c,ij}\} c_{i\sigma}^{\dagger}(\tau) c_{j\sigma}(\tau) \\
&+ \sum_{i\sigma} \{\partial_\tau - \mu + \epsilon_f + \lambda(\tau)\} f_{i\sigma}^{\dagger}(\tau) f_{i\sigma}(\tau) + \sum_{ij\sigma} t_{f,ij} |b(\tau)|^2 f_{i\sigma}^{\dagger}(\tau) f_{j\sigma}(\tau) \\
&+ \frac{1}{\sqrt{N}} \sum_{ij\sigma\sigma'} \{V_{ij\sigma\sigma'} b^*(\tau) c_{i\sigma}^{\dagger}(\tau) f_{j\sigma'}(\tau) + \text{h.c.}\} + \sum_{\boldsymbol{i}} \lambda(\tau)(|b(\tau)|^2 - 1).
\end{aligned} \tag{A.5}$$

To derive the self-consistent equations for b and λ, we integrate out the fermionic degrees of freedom c and f and derive the effective action for bosonic fields $b(\tau)$ and scalar fields $\lambda(\tau)$. The effective action S_{eff} is defined as

$$e^{-S_{\text{eff}}[b^\dagger,b,\lambda]} \equiv \int \mathcal{D}[c^\dagger, c, f^\dagger, f] e^{-S_{\text{MF}}[c^\dagger,c,f^\dagger,f,b^\dagger,b,\lambda]},$$

where

$$S_{\text{MF}} = \int_0^\beta d\tau \mathcal{L}_{\text{MF}}[c^\dagger(\tau), c(\tau), f^\dagger(\tau), f(\tau), b^\dagger(\tau), b(\tau), \lambda(\tau)]. \tag{A.6}$$

The self-consistent equations are given by the saddle point conditions for the effective action:

$$\frac{\delta S_{\text{eff}}}{\delta b(\tau)} = 0, \frac{\delta S_{\text{eff}}}{\delta \lambda(\tau)} = 0. \tag{A.7}$$

These conditions can be rewritten using S_{MF} as

$$\left\langle \frac{\delta S_{\text{MF}}}{\delta b(\tau)} \right\rangle = 0, \left\langle \frac{\delta S_{\text{MF}}}{\delta \lambda(\tau)} \right\rangle = 0, \tag{A.8}$$

where $\langle \cdots \rangle$ is the thermal average defined as

$$\langle \cdots \rangle = \frac{\int \mathcal{D}[c^\dagger(\tau), c(\tau), f^\dagger(\tau), f(\tau)] \cdots e^{-S_{\text{MF}}}}{\int \mathcal{D}[c^\dagger(\tau), c(\tau), f^\dagger(\tau), f(\tau)] e^{-S_{\text{MF}}}}. \tag{A.9}$$

Using eqs. (A.5) and (A.8), we can derive the self-consistent equations (3.3) and (3.4).

Appendix B

Derivation of effective spin models from Hubbard models under DC electric fields

In this Appendix, we present the derivations of the effective spin models discussed in Chap. 4. In Sec. B.1 and Sec. B.2, we derive spin-$\frac{1}{2}$ and spin-1 model respectively. In addition, to clarify to what extent our effective models are valid, we explain the parameter regime of the original models in Sec. B.3.

B.1 Spin-$\frac{1}{2}$ effective model from a single-band Hubbard model

This section is devoted to the derivation of the spin-$\frac{1}{2}$ effective model (4.2) in Chap.4. We start from a half-filled, repulsive Hubbard model ($U > 0$) with an arbitrary on-site potential term. The Hamiltonian reads

$$\begin{aligned}\mathcal{H} &= \sum_{ij\sigma} t_{ij} c^{\dagger}_{i\sigma} c_{j\sigma} + U \sum_{i} n_{i\uparrow} n_{i\downarrow} + \sum_{i\sigma} V_i n_{i\sigma} \\ &= \mathcal{H}_t + \mathcal{H}_U + \mathcal{H}_V, \end{aligned} \tag{B.1}$$

where $\mathcal{H}_t$, $\mathcal{H}_U$, and $\mathcal{H}_t$ denote the electron hopping, the on-site Coulomb interaction, and the on-site potential, respectively. We assume that all the on-site potential energies are smaller than the Coulomb interaction energy, i.e., $|V_i| < U$.

In order to perform perturbative calculations for any quantum system, it is generally useful to introduce projection operators onto Hilbert subspaces. Let us divide the full Hilbert space into a low- and high-energy states, $\{|\Psi_g\rangle\}$ and $\{|\Psi_e\rangle\}$, and define the projection operator onto the low-energy (high-energy) state P_e (P_g). Using these instruments, we can arrive at the effective Hamiltonian for the low-energy subspace in the second-order perturbation theory:

$$\mathcal{H}_{\text{eff}} = \mathcal{H}_{gg} + \mathcal{H}_{ge} \frac{1}{E_g - \mathcal{H}_{ee}} \mathcal{H}_{eg}, \tag{B.2}$$

where $\mathcal{H}_{\alpha\beta} = P_\alpha \mathcal{H} P_\beta$ ($\alpha, \beta = g, e$) and E_g is defined by $\mathcal{H}_{gg} |\Psi_g\rangle = E_g |\Psi_g\rangle$.

We apply the above formula (B.2) to the Mott insulating state of the Hubbard model (B.1) in the strong-coupling limit, i.e. $U \to \infty$. In this limit, the ground states of the unperturbed Hamiltonian $\mathcal{H}_U + \mathcal{H}_V$ are states where all sites are singly occupied. We treat the hopping

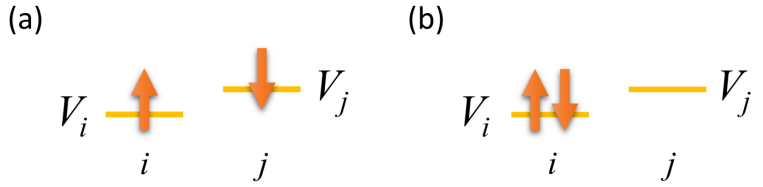

Figure B.1: Spin configuration of states relevant to the second-order perturbative calculation: (a) A ground state and (b) an intermediate state.

term $\mathcal{H}_t$ as the perturbation, and define the low-energy (high-energy) subspace as the ground states (states with doubly occupied sites).

First we consider $\mathcal{H}_{eg}$ in the Mott insulating state of the Hubbard model (B.1). In the three terms $\mathcal{H}_t$, $\mathcal{H}_U$ and $\mathcal{H}_V$ of the Hamiltonian $\mathcal{H}$, only the hopping $\mathcal{H}_t$ has a matrix element between high and low-energy states, $\{|\Psi_g\rangle\}$ and $\{|\Psi_e\rangle\}$. Therefore $\mathcal{H}_{eg}$ is written as

$$\mathcal{H}_{eg} = P_e \left(\sum_{ij\sigma} t_{ij} c^\dagger_{i\sigma} c_{j\sigma} \right) P_g. \tag{B.3}$$

From the Pauli's exclusion principle and the half-filled condition, we see that $\mathcal{H}_{eg}$ survives only when the spin indices σ on the i-th and j-th sites are different, i.e., $(S^z_i, S^z_j) = (\uparrow, \downarrow), (\downarrow, \uparrow)$, as shown in Fig. B.1 (a). We may thus rewrite $\mathcal{H}_{eg}$ as

$$\mathcal{H}_{eg} = \sum_{ij\sigma} t_{ij} c^\dagger_{i\sigma} c_{j\sigma} (S^z_i - S^z_j)^2. \tag{B.4}$$

Next we compute the energy difference between the ground and the intermediate high-energy states depicted in Fig. B.1. To this end, we may focus on two neighboring i-th and j-th sites. In the ground states, both the sites are singly occupied and thus their energy is given by $V_i + V_j$. In contrast, the i-th site is doubly occupied and the j-th site is vacant in the intermediate states. Thus the energy is $U + 2V_i$. These results lead to

$$\begin{aligned} \frac{1}{E_g - \mathcal{H}_{ee}} \mathcal{H}_{eg} &= \sum_{ij\sigma} \frac{1}{(V_i + V_j) - (U + 2V_i)} t_{ij} c^\dagger_{i\sigma} c_{j\sigma} (S^z_i - S^z_j)^2 \\ &= -\sum_{ij\sigma} \frac{1}{U - \Delta V_{ij}} t_{ij} c^\dagger_{i\sigma} c_{j\sigma} (S^z_i - S^z_j)^2. \end{aligned} \tag{B.5}$$

Here we define $\Delta V_{ij} = V_i - V_j$.

Finally, we operate the $\mathcal{H}_{ge}$ to Eq. (B.5) and then the second-order perturbation term is calculated as follows:

$$\begin{aligned}
\mathcal{H}_{ge}\frac{1}{E_g-\mathcal{H}_{ee}}\mathcal{H}_{eg} &= -P_g\sum_{i'j'\sigma'} t_{j'i'}c^\dagger_{j'\sigma'}c_{i'\sigma'}\sum_{ij\sigma}\frac{1}{U-\Delta V_{ij}}t_{ij}c^\dagger_{i\sigma}c_{j\sigma}(S^z_i-S^z_j)^2 \\
&= -\sum_{ij\sigma}\frac{|t_{ij}|^2}{U-\Delta V_{ij}}c^\dagger_{j\sigma}c_{i\sigma}c^\dagger_{i\sigma}c_{j\sigma}(S^z_i-S^z_j)^2-\sum_{ij\sigma}\frac{|t_{ij}|^2}{U-\Delta V_{ij}}c^\dagger_{j\bar{\sigma}}c_{i\bar{\sigma}}c^\dagger_{i\sigma}c_{j\sigma}(S^z_i-S^z_j)^2 \\
&= -\sum_{ij\sigma}\frac{|t_{ij}|^2}{U-\Delta V_{ij}}n_{j\sigma}(1-n_{i\sigma})(S^z_i-S^z_j)^2+\sum_{ij\sigma}\frac{|t_{ij}|^2}{U-\Delta V_{ij}}c^\dagger_{j\bar{\sigma}}c_{j\sigma}c^\dagger_{i\sigma}c_{i\bar{\sigma}}(S^z_i-S^z_j)^2 \\
&= -\sum_{ij}\frac{|t_{ij}|^2}{U-\Delta V_{ij}}(S^z_i-S^z_j)^2+\sum_{ij}\frac{|t_{ij}|^2}{U-\Delta V_{ij}}(S^-_jS^+_i+S^+_jS^-_i)(S^z_i-S^z_j)^2 \\
&= -\sum_{ij}\frac{|t_{ij}|^2}{U-\Delta V_{ij}}(S^z_i-S^z_j)^2+\sum_{ij}\frac{|t_{ij}|^2}{U-\Delta V_{ij}}(S^-_jS^+_i+S^+_jS^-_i) \\
&= \sum_{ij}\frac{|t_{ij}|^2}{U-\Delta V_{ij}}\left(-\frac{1}{2}+2S^z_iS^z_j+S^+_iS^-_j+S^-_iS^+_j\right) \\
&= \sum_{ij}\frac{2|t_{ij}|^2}{U-\Delta V_{ij}}\boldsymbol{S}_i\cdot\boldsymbol{S}_j+\text{const.},
\end{aligned} \tag{B.6}$$

where we have defined $\bar{\sigma}=-\sigma$. The first-order term $\mathcal{H}_{gg}$ gives only a constant term, and therefore the effective Hamiltonian up to the second-order perturbation theory is given by

$$\begin{aligned}
\mathcal{H}_{\text{eff}} &= \sum_{ij}\frac{2|t_{ij}|^2}{U-\Delta V_{ij}}\boldsymbol{S}_i\cdot\boldsymbol{S}_j+\text{const.} \\
&= \sum_{\langle ij\rangle}\frac{4|t_{ij}|^2}{U}\frac{1}{1-\left(\frac{\Delta V_{ij}}{U}\right)^2}\boldsymbol{S}_i\cdot\boldsymbol{S}_j+\text{const.},
\end{aligned} \tag{B.7}$$

where the summation is taken over every bond $\langle i,j\rangle$ in the last line. This is the effective model (4.2) in Chap. 4.

B.2 Spin-1 effective model from a two-band Hubbard model

In this section, we show the derivation of the effective spin-1 model (4.3) in Chap. 4. We start from a half-filled, two-orbital Hubbard model with an additional on-site potential. The Hamiltonian consists of three parts of hopping, interaction, and potential terms:

$$\mathcal{H} \;=\; \mathcal{H}_t + \mathcal{H}_V + \mathcal{H}_{\rm int}. \tag{B.8}$$

These terms are given by

$$\mathcal{H}_t = \sum_{ij}\sum_{\alpha}\sum_{\sigma} t_{ij} c^\dagger_{i\alpha\sigma} c_{j\alpha\sigma}, \tag{B.9}$$

$$\mathcal{H}_V = \sum_{i\sigma} V_i n_{i\alpha\sigma}, \tag{B.10}$$

$$\begin{aligned}\mathcal{H}_{\rm int} = {} & U\sum_i\sum_\alpha n_{i\alpha\uparrow}n_{i\alpha\downarrow} + U'\sum_i\sum_{\sigma\sigma'} n_{i1\sigma}n_{i2\sigma'} \\ & - J\sum_i\sum_{\sigma\sigma'} c^\dagger_{i1\sigma}c_{i1\sigma'}c^\dagger_{i2\sigma'}c_{i2\sigma} - J_P\sum_i\left(c^\dagger_{i1\uparrow}c^\dagger_{i1\downarrow}c_{i2\downarrow}c_{i2\uparrow} + \text{h.c.}\right).\end{aligned} \tag{B.11}$$

Here $\alpha(=1,2)$ is orbital index and $\bar{\sigma}$ denotes the opposite spin $-\sigma$. In the interaction $\mathcal{H}_{\rm int}$, U, U', J, and J_P terms denote an intra-orbital interaction, an inter-orbital interaction, a Hund's coupling and a pair hopping respectively. Due to the rotational symmetry of Coulomb interaction, $J_P = J$ is required. For convenience, we transform the interaction $\mathcal{H}_{\rm int}$ (B.11) as follows:

$$\begin{aligned}\mathcal{H}_{\rm int} = {} & U\sum_i\sum_\alpha n_{i\alpha\uparrow}n_{i\alpha\downarrow} + \left(U' - \frac{J}{2}\right)\sum_i\sum_{\sigma\sigma'} n_{i1\sigma}n_{i2\sigma'} \\ & - 2J\sum_i \boldsymbol{S}_{i1}\cdot\boldsymbol{S}_{i2} - J\sum_i\left(c^\dagger_{i1\uparrow}c^\dagger_{i1\downarrow}c_{i2\downarrow}c_{i2\uparrow} + \text{h.c.}\right),\end{aligned} \tag{B.12}$$

where we have used the identity

$$\sum_\sigma c^\dagger_{i1\sigma}c_{i1\bar{\sigma}}c^\dagger_{i2\bar{\sigma}}c_{i2\sigma} = 2\boldsymbol{S}_{i1}\cdot\boldsymbol{S}_{i2} - \frac{1}{2}\sum_\sigma n_{i1\sigma}n_{i2\sigma} + \frac{1}{2}\sum_\sigma n_{i1\sigma}n_{i2\bar{\sigma}}, \tag{B.13}$$

and $\boldsymbol{S}_{i\alpha}$ is the spin operator for an α-orbital electron on i-th site.

First we discuss the ground state under the condition of both the half-filling and the strong-coupling limit $U > U' > J \gg t$. In this condition, all the orbits are singly occupied and there are two electrons per one site in the ground states. We here introduce local bases $|\psi\rangle_i$ to represent the spin state on each site i. They are classified into the spin-triplet sector $\mathcal{T}_i$ and the spin-singlet sector $\mathcal{S}_i$:

$$\mathcal{T}_i = \{|+\rangle_i, |\circ\rangle_i, |-\rangle_i\}, \tag{B.14}$$

$$\mathcal{S}_i = \{|s\rangle_i\}. \tag{B.15}$$

Four kinds of $|\psi\rangle_i$ are defined as

$$|+\rangle_i = c^\dagger_{i1\uparrow}c^\dagger_{i2\uparrow}|0\rangle, \tag{B.16}$$

$$|-\rangle_i = c^\dagger_{i1\downarrow}c^\dagger_{i2\downarrow}|0\rangle, \tag{B.17}$$

$$|\circ\rangle_i = \frac{1}{\sqrt{2}}\left(c^\dagger_{i1\uparrow}c^\dagger_{i2\downarrow}|0\rangle + c^\dagger_{i1\downarrow}c^\dagger_{i2\uparrow}|0\rangle\right), \tag{B.18}$$

$$|s\rangle_i = \frac{1}{\sqrt{2}}\left(c^\dagger_{i1\uparrow}c^\dagger_{i2\downarrow}|0\rangle - c^\dagger_{i1\downarrow}c^\dagger_{i2\uparrow}|0\rangle\right), \tag{B.19}$$

where $|+\rangle_i$, $|-\rangle_i$, and $|\circ\rangle_i$ are respectively the $S^z = +1$, -1, and 0 state on i-th site. Within this localized spin subspace, the correlation function of two-orbital spins on a given site is computed as

$$\langle\psi|_i \boldsymbol{S}_{i1} \cdot \boldsymbol{S}_{i2} |\psi\rangle_i = \begin{cases} \frac{1}{4} & (|\psi\rangle_i \in \mathcal{T}_i) \\ -\frac{3}{4} & (|\psi\rangle_i \in \mathcal{S}_i). \end{cases} \tag{B.20}$$

This result and Hund's coupling in Eq. (B.12) clearly show that the ground state on each site is in the spin-triplet sector, namely, localized spin-1 system is realized in Eq. (B.8).

Next, we focus on the zero-potential case of $V_i = 0$. As one will see soon later, the effective model for $V_i \neq 0$ can be easily derived by simply extending the result of the $V_i = 0$ case. Using the formula (B.2), let us derive the effective spin model for the $V_i = 0$ case with the hopping $\mathcal{H}_t$ being the perturbation. To this end, we introduce the nine local bases $|\psi_i\rangle_i |\psi_j\rangle_j$ which represent neighboring i-th and j-th spin states ($\psi_{i,j} \in \{+, \circ, -\}$). In the matrix form, the bases are expressed as

$$|\Psi_{ij}\rangle = \begin{pmatrix} |+\rangle_i |+\rangle_j \\ |+\rangle_i |\circ\rangle_j \\ |+\rangle_i |-\rangle_j \\ |\circ\rangle_i |+\rangle_j \\ |\circ\rangle_i |\circ\rangle_j \\ |\circ\rangle_i |-\rangle_j \\ |-\rangle_i |+\rangle_j \\ |-\rangle_i |\circ\rangle_j \\ |-\rangle_i |-\rangle_j \end{pmatrix}. \tag{B.21}$$

Through straightforward calculation, we obtain

$$\mathcal{H}_{ge}\mathcal{H}_{eg} |+\rangle_i |-\rangle_j = -|\circ\rangle_i |\circ\rangle_j + 2|+\rangle_i |-\rangle_j , \tag{B.22}$$

$$\mathcal{H}_{ge}\mathcal{H}_{eg} |+\rangle_i |0\rangle_j = -|0\rangle_i |+\rangle_j + |+\rangle_i |0\rangle_j , \tag{B.23}$$

$$\mathcal{H}_{ge}\mathcal{H}_{eg} |0\rangle_i |0\rangle_j = -|+\rangle_i |-\rangle_j - |-\rangle_i |+\rangle_j + |\circ\rangle_i |\circ\rangle_j , \tag{B.24}$$

and

$$\mathcal{H}_{ge}\frac{1}{E_g - \mathcal{H}_{ee}}\mathcal{H}_{eg} |+\rangle_i |-\rangle_j = \frac{|t_{ij}|^2}{\Delta E_{ij}} \left(-|\circ\rangle_i |\circ\rangle_j + 2|+\rangle_i |-\rangle_j \right), \tag{B.25}$$

$$\mathcal{H}_{ge}\frac{1}{E_g - \mathcal{H}_{ee}}\mathcal{H}_{eg} |+\rangle_i |0\rangle_j = \frac{|t_{ij}|^2}{\Delta E_{ij}} \left(-|0\rangle_i |+\rangle_j + |+\rangle_i |0\rangle_j \right), \tag{B.26}$$

$$\mathcal{H}_{ge}\frac{1}{E_g - \mathcal{H}_{ee}}\mathcal{H}_{eg} |0\rangle_i |0\rangle_j = \frac{|t_{ij}|^2}{\Delta E_{ij}} \left(-|+\rangle_i |-\rangle_j - |-\rangle_i |+\rangle_j + |\circ\rangle_i |\circ\rangle_j \right), \tag{B.27}$$

where

$$\begin{aligned} \Delta E_{ij} &= \left\{ 2 \times \left(U' - \frac{J}{2} \right) - 2 \times 2J \cdot \frac{1}{4} \right\} - \left\{ U + 2 \times \left(U' - \frac{J}{2} \right) \right\} \\ &= -(U + J). \end{aligned} \tag{B.28}$$

From these results, the effective Hamiltonian in the i-th and j-th sites is given by

$$\langle\Psi_{ij}|\,\mathcal{H}_{\text{eff}}\,|\Psi_{ij}\rangle = E_g I + \frac{|t_{ij}|^2}{U+J}\begin{pmatrix} 0 & 0 & 0 & 0 & 0 & 0 & 0 & 0 & 0 \\ 0 & -1 & 0 & 1 & 0 & 0 & 0 & 0 & 0 \\ 0 & 0 & -2 & 0 & 1 & 0 & 0 & 0 & 0 \\ 0 & 1 & 0 & -1 & 0 & 0 & 0 & 0 & 0 \\ 0 & 0 & 1 & 0 & -1 & 0 & 1 & 0 & 0 \\ 0 & 0 & 0 & 0 & 0 & -1 & 0 & 1 & 0 \\ 0 & 0 & 0 & 0 & 1 & 0 & -2 & 0 & 0 \\ 0 & 0 & 0 & 0 & 0 & 1 & 0 & -1 & 0 \\ 0 & 0 & 0 & 0 & 0 & 0 & 0 & 0 & 0 \end{pmatrix}. \tag{B.29}$$

For spin-1 systems, SU(2)-symmetric interactions between two neighboring spins are limited to a bilinear term $\boldsymbol{S}_i \cdot \boldsymbol{S}_j$ and a biquadratic term $(\boldsymbol{S}_i \cdot \boldsymbol{S}_j)^2$. In our notation, the matrix elements of the bilinear term are given by

$$\langle\Psi_{ij}|\,\boldsymbol{S}_i \cdot \boldsymbol{S}_j\,|\Psi_{ij}\rangle = \begin{pmatrix} 1 & 0 & 0 & 0 & 0 & 0 & 0 & 0 & 0 \\ 0 & 0 & 0 & 1 & 0 & 0 & 0 & 0 & 0 \\ 0 & 0 & -1 & 0 & 1 & 0 & 0 & 0 & 0 \\ 0 & 1 & 0 & 0 & 0 & 0 & 0 & 0 & 0 \\ 0 & 0 & 1 & 0 & 0 & 0 & 1 & 0 & 0 \\ 0 & 0 & 0 & 0 & 0 & 0 & 0 & 1 & 0 \\ 0 & 0 & 0 & 0 & 1 & 0 & -1 & 0 & 0 \\ 0 & 0 & 0 & 0 & 0 & 1 & 0 & 0 & 0 \\ 0 & 0 & 0 & 0 & 0 & 0 & 0 & 0 & 1 \end{pmatrix}, \tag{B.30}$$

and those of the biquadratic term are computed as

$$\langle\Psi_{ij}|\,(\boldsymbol{S}_i \cdot \boldsymbol{S}_j)^2\,|\Psi_{ij}\rangle = \begin{pmatrix} 1 & 0 & 0 & 0 & 0 & 0 & 0 & 0 & 0 \\ 0 & 1 & 0 & 1 & 0 & 0 & 0 & 0 & 0 \\ 0 & 0 & 2 & 0 & -1 & 0 & 1 & 0 & 0 \\ 0 & 1 & 0 & 1 & 0 & 0 & 0 & 0 & 0 \\ 0 & 0 & -1 & 0 & 2 & 0 & -1 & 0 & 0 \\ 0 & 0 & 0 & 0 & 0 & 1 & 0 & 1 & 0 \\ 0 & 0 & 1 & 0 & -1 & 0 & 2 & 0 & 0 \\ 0 & 0 & 0 & 0 & 0 & 1 & 0 & 1 & 0 \\ 0 & 0 & 0 & 0 & 0 & 0 & 0 & 0 & 1 \end{pmatrix}. \tag{B.31}$$

Comparing Eqs. (B.29) with (B.30) and (B.31), we can find the following relation

$$\langle\Psi_{ij}|\,\mathcal{H}_{\text{eff}}\,|\Psi_{ij}\rangle = E_g I + \frac{|t_{ij}|^2}{U-J}\left(\langle\Psi_{ij}|\,\boldsymbol{S}_i \cdot \boldsymbol{S}_j\,|\Psi_{ij}\rangle - I\right). \tag{B.32}$$

From these results, the effective spin model for the zero-potential system is written as

$$\begin{aligned} \mathcal{H}_{\text{eff}} &= \sum_{ij} \frac{|t_{ij}|^2}{U+J} \boldsymbol{S}_i \cdot \boldsymbol{S}_j \\ &= \sum_{\langle ij \rangle} \frac{2|t_{ij}|^2}{U+J} \boldsymbol{S}_i \cdot \boldsymbol{S}_j \\ &= J_{ij}^{S=1} \sum_{\langle ij \rangle} \boldsymbol{S}_i \cdot \boldsymbol{S}_j, \end{aligned} \tag{B.33}$$

where we have defined $J_{ij}^{S=1} = 2|t_{ij}|^2/(U+J)$.

Finally, let us turn to a generic case with $V_i \neq 0$. In this case, most of the perturbative calculations are the same as those of the $V_i = 0$ case. However, ΔE_{ij} of Eq. (B.28) should be changed into

$$\begin{aligned}\Delta E_{ij} &= \left\{2 \times \left(U' - \frac{J}{2}\right) - 2 \times 2J \cdot \frac{1}{4}\right) + 2V_i + 2V_j\} - \left\{U + 2 \times \left(U' - \frac{J}{2}\right) + 3V_i + V_j\right\} \\ &= -(U + J + \Delta V_{ij}),\end{aligned} \tag{B.34}$$

where $\Delta V_{ij} = V_i - V_j$. Thus the effective spin model for the two-orbital Hubbard model with an on-site potential is written as

$$\begin{aligned}\mathcal{H}_{\text{eff}} &= \sum_{ij} \frac{|t_{ij}|^2}{U + J + \Delta V_{ij}} \boldsymbol{S}_i \cdot \boldsymbol{S}_j \\ &= \sum_{\langle ij \rangle} \frac{J_{ij}^{S=1}}{1 - \left(\frac{\Delta V_{ij}}{U+J}\right)^2} \boldsymbol{S}_i \cdot \boldsymbol{S}_j.\end{aligned} \tag{B.35}$$

This is the effective model (4.3) in Chap. 4.

B.3 Parameter regime for our effective models

Here, we clearly mention the parameter range where our strong-coupling approach in Secs. B.1 and B.2 is valid. There are three conditions below must be satisfied.

Condition 1: $U \gg W$ (Strong coupling)

Our study is based on the perturbative expansion in terms of $|t_{ij}|/U$, where t_{ij} is the hopping amplitude and $U(> 0)$ is the interaction strength, as illustrated in the previous Secs. B.1 and B.2. This perturbation theory is valid for $U \gg W$ where $W = \mathcal{O}(|t_{ij}|)$ is the band width.

Condition 2: $U - |e|aE \gg W$ (No "Mott breakdown")

In this paper, we consider the Mott insulating state under a spatially dependent potential V_{ij} driven by a DC field. The voltage between the neighboring sites ΔV_{ij} is given by $|e|aE$ where e, a, and E are the electron charge, the lattice constant, and the strength of the DC field, respectively. If the voltage becomes too large, the Mott insulating state is broken (Mott breakdown) and a large electric current appears. The accurate condition for the occurrence of Mott breakdown is still under debate, but we can say that the Mott insulator survives if the condition $U - |e|aE \gg W$ is satisfied. We note that this condition is hold even if $|e|aE$ becomes comparable to U and the hopping $|t_{ij}|$ is sufficiently small. We also note that the Condition 2 restricts the parameter range of the system much stronger than the Condition 1 (Condition 2 $\subset$ Condition 1).

When the applied DC field becomes strong so that $U - |e|aE$ is comparable to W, the higher-order perturbation terms cannot be negligible in our strong-coupling calculation of Secs. B.1 and B.2. Namely, our Heisenberg type models including only the lowest-order perturbation term become invalid. In such a case, ring-exchange, biquadratic interactions, etc. should be considered and there is the possibility that these higher-order interactions drastically change our phase diagrams of Figs. 4.2-4.4 in Chap. 4.

Condition 3: $U - W \gg k_{\mathrm{B}}T$ (Low temperature)

When the energy scale of temperature k_BT becomes comparable to the Mott gap $\Delta_{\mathrm{Mott}} \sim U$, many electrons are thermally excited to the upper Hubbard band and they behave as thermal carriers (see Fig. B.2) under the application of a DC electric field. This carriers yield a finite current and crucially affect the magnetism. Such a system can not be regarded as a localized spin system and thus this case is out of scope of our study. Therefore, we need the condition $U - W \gg k_BT$. Of course, this is the same as the condition that generic quantum spin models are reliable to describe magnetism of the target systems. Usually, $U - W$ is much larger than room temperature in Mott insulators. Therefore, our strong-coupling approach can be applied in a wide low-temperature range.

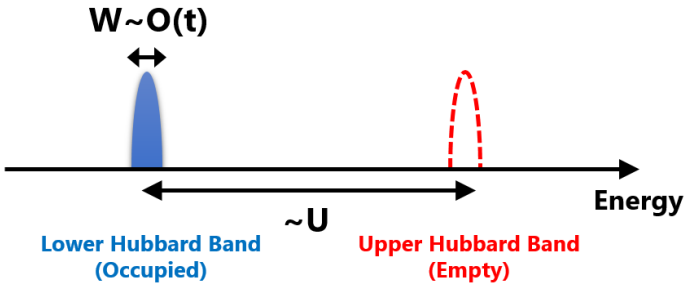

Figure B.2: Schematic picture of the density of states of half-filled Hubbard models. There are the lower Hubbard band (occupied) and the upper Hubbard band (empty) separated by the Mott gap $\Delta_{\mathrm{Mott}} \sim U$. Each band has a finite band width $W = \mathcal{O}(|t_{ij}|)$ where t_{ij} is the hopping amplitude.

Appendix C

Bosonization and chain mean-field approach

In this Appendix, we shortly explain the computation process of the critical temperature between Néel ordered and paramagnetic phases in our quasi-1D spin-$\frac{1}{2}$ model (4.5) in Chap. 4. First we summarize some results of the bosonization for spin-$\frac{1}{2}$ chains [96, 203–205]. Then, by combining the chain mean-field theory (MFT) with the bosonization results [207–213], we determine the critical temperature of the quasi-1D model (4.5).

We start from the definition of the 1D spin-$\frac{1}{2}$ XXZ chain model. The Hamiltonian is given by

$$\mathcal{H}_{\rm xxz} \;=\; J\sum_j \Big[S^x_j S^x_{j+1} + S^y_j S^y_{j+1} + \Delta_z S^z_j S^z_{j+1}\Big] - H\sum_j S^z_j, \tag{C.1}$$

where $\boldsymbol{S}_j$ is the spin-$\frac{1}{2}$ operator on j-th site, $J>0$ is the strength of the exchange interaction, Δ_z is the XXZ anisotropy parameter, and H is the external magnetic field. The point of $\Delta_z = 1$ and $H = 0$ corresponds to the SU(2)-symmetric antiferromagnetic Heisenberg model. The XXZ model is a typical integrable system and the TL-liquid phase with gapless spinon excitations widely exists in the range $-1 < \Delta_z \le 1$ at zero field $H = 0$. The TL liquid phase survives from zero field to the saturation field. The bosonization can accurately describe the low-energy properties in/around the TL-liquid phase. Through the standard bosonization process, the XXZ model in/around the TL-liquid phase is mapped to a low-energy gapless scalar-field theory, whose Hamiltonian is

$$\mathcal{H}_{\rm eff} = \int dx\; \frac{v}{2}\Big[\frac{1}{K}(\partial_x\phi)^2 + K(\partial_x\theta)^2\Big], \tag{C.2}$$

where $x = ja_0$ is the continuous coordinate (a_0 : lattice constant), and $\phi(x,t)$ and $\theta(x,t)$ are the canonical pair of real scalar fields satisfying the commutation relation $[\phi(x,t), \partial_y\theta(y,t)] = i\delta(x-y)$. Two symbols v and K respectively denote the spinon group velocity and the TL-liquid parameter. For instance, $K = 1$ and $v = \pi J a_0/2$ at the SU(2) point. Spin operators are also bosonized as

$$\begin{aligned} S^z_j &\approx M + \frac{a_0}{\sqrt{2\pi}}\partial_x\phi + (-1)^j A_1 \cos\Big(\sqrt{2\pi}\phi + 2\pi M j\Big) + \cdots, \\ S^+_j &\approx e^{i\sqrt{2\pi}\theta}\Big[(-1)^j B_0 + B_1\cos\Big(\sqrt{2\pi}\phi + 2\pi M j\Big) + \cdots\Big]. \end{aligned} \tag{C.3}$$

where $M = \langle S^z_j\rangle$ is the H-induced uniform magnetization per site, and A_n and B_n are non-universal constants depending on the model parameters J, Δ_z and H. The accurate values of

v, K, A_n and B_n have been computed by using Bethe ansatz and numerical methods [231–236]. On the basis of the formulas (C.2) and (C.3), one can correctly calculate the long-distance or long-time behavior of correlation functions in the TL-liquid phase. Let us define the dynamical spin susceptibility with the wave number k and frequency ω as $\chi_R^{ab}(k,\omega) = -\int_0^\beta d\tau \sum_k e^{-ikja_0+i\omega_n\tau}\langle T_\tau S_j^a(\tau)S_0^b(0)\rangle|_{i\omega_n=\omega+i\eta}$, where τ is imaginary time, $\beta = 1/(k_BT)$ is inverse temperature, $\omega_n = 2\pi n/\beta$ (n: integer), and η is an infinitesimal positive constant. Through the bosonization technique with Eqs. (C.2) and (C.3), one can calculate the transverse dynamical susceptibility around $k = \pi + \delta k$ in the TL-liquid phase:

$$\begin{aligned}\chi_R^{-+}(\pi+\delta k,\omega) \;\approx\; & -B_0^2\,\frac{a_0}{v}\,\sin\Big(\frac{\pi}{2K}\Big)\,\Big(\frac{2\pi a_0}{\beta v}\Big)^{1/K-2} \\ & \times B\Big(-i\frac{\beta(\omega-v\delta k)}{4\pi}+\frac{1}{4K},1-\frac{1}{2K}\Big) \\ & \times B\Big(-i\frac{\beta(\omega+v\delta k)}{4\pi}+\frac{1}{4K},1-\frac{1}{2K}\Big),\end{aligned} \tag{C.4}$$

where $S_j^\pm = S_j^x \pm iS_j^y$ and $B(x,y)$ is Beta function. This formula is quite reliable in the range of $|\delta k| \ll a_0^{-1}$ and $|\omega| \ll J, k_BT$. In the TL-liquid phase of the XXZ chain, the relation $\chi_R^{xx}(k,\omega) = \chi_R^{yy}(k,\omega) = \frac{1}{2}\chi_R^{-+}(k,\omega)$ holds.

Next, we apply the chain MFT to our quasi-1D spin-$\frac{1}{2}$ magnet (4.5) in Chap. 4 with the above bosonization results. In the chain MFT, we accurately take into account quantum and thermal fluctuation effects in the strong coupled 1D direction, while an inter-chain interaction is treated within the standard MFT. On the basis of this approach, the S^x component of the dynamical spin susceptibility in the quasi-1D system (4.5) is calculated as the following RPA-like form:

$$\chi_{\rm 3D}^{xx}(k_x,k_y,k_z,\omega) \;=\; \frac{\chi_R^{xx}(k_x,\omega)}{1-2(J_y\cos k_y + J_z\cos k_z)\chi_R^{xx}(k_x,\omega)}, \tag{C.5}$$

where the wave number k_x corresponds to the 1D-chain direction, and $k_{y,z}$ are the wave numbers along the inter-chain direction. This result is quantitatively valid in the sufficiently weak inter-chain regime $|J_{y,z}| \ll J$. The phase transition between the Néel and paramagnetic phases is determined as the point where $\chi_{\rm 3D}^{xx}(\pi,\pi,\pi,\omega\to 0)$ diverges. This point is equivalent to the condition that the denominator of Eq. (C.5) becomes zero at $\boldsymbol{k} = (\pi,\pi,\pi)$ and $\omega \to 0$:

$$-2(J_y+J_z)\chi_R^{xx}(\pi,\omega\to 0) = 1 \tag{C.6}$$

Substituting the bosonization result (C.4) into this condition, we arrive at the formula of determining the phase transition temperature:

$$B_0^2\,\frac{(J_y+J_z)a_0}{v}\,\sin\Big(\frac{\pi}{2K}\Big)\,\Big(\frac{2\pi a_0}{\beta v}\Big)^{1/K-2}\,B\Big(\frac{1}{4K},1-\frac{1}{2K}\Big)^2 = 1. \tag{C.7}$$

Using this result, we have drawn the phase boundary of Fig. 4.4 (b) and (c) in Chap. 4. We finally note a technical issue that since the parameter B_0 is ill-defined just on the SU(2) point of $\Delta_z = 1$ and $H = M = 0$, we have used its value for a nearly SU(2)-symmetric model with an infinitesimal small magnetization $M = 0.01$ in Fig. 4.4 in Chap. 4.

Bibliography

[1] D. Fausti, R. I. Tobey, N. Dean, S. Kaiser, A. Dienst, M. C. Hoffmann, S. Pyon, T. Takayama, H. Takagi, and A. Cavalleri, Science **331**, 189 (2011).

[2] T. Oka and H. Aoki, Phys. Rev. B **79**, 081406 (2009).

[3] Y. H. Wang, H. Steinberg, P. Jarillo-Herrero, and N. Gedik, Science **342**, 453 (2013).

[4] F. Mahmood, C.-K. Chan, Z. Alpichshev, D. Gardner, Y. Lee, P. A. Lee, and N. Gedik, Nat. Phys. **12**, 306 (2016).

[5] J. W. McIver, B. Schulte, F. U. Stein, T. Matsuyama, G. Jotzu, G. Meier, and A. Cavalleri, arXiv:1811.03522 (2018).

[6] C. Sow, S. Yonezawa, S. Kitamura, T. Oka, K. Kuroki, F. Nakamura, and Y. Maeno, Science **358**, 1084 (2017).

[7] A. Eckardt, Rev. Mod. Phys. **89**, 011004 (2017).

[8] R. Kubo, Journal of the Physical Society of Japan **12**, 570 (1957).

[9] F. Bloch, Zeitschrift für Physik **52**, 555 (1929).

[10] J. G. Bednorz and K. A. Müller, Zeitschrift für Physik B Condensed Matter **64**, 189 (1986).

[11] T. J. Yen, W. J. Padilla, N. Fang, D. C. Vier, D. R. Smith, J. B. Pendry, D. N. Basov, and X. Zhang, Science **303**, 1494 (2004).

[12] Y. Mukai, H. Hirori, T. Yamamoto, H. Kageyama, and K. Tanaka, New Journal of Physics **18**, 013045 (2016).

[13] T. Oka and L. Bucciantini, Phys. Rev. B **94**, 155133 (2016).

[14] S. Choi, J. Choi, R. Landig, G. Kucsko, H. Zhou, J. Isoya, F. Jelezko, S. Onoda, H. Sumiya, V. Khemani, C. von Keyserlingk, N. Y. Yao, E. Demler, and M. D. Lukin, Nature **543**, 221 EP (2017).

[15] J. Zhang, P. W. Hess, A. Kyprianidis, P. Becker, A. Lee, J. Smith, G. Pagano, I.-D. Potirniche, A. C. Potter, A. Vishwanath, N. Y. Yao, and C. Monroe, Nature **543**, 217 EP (2017).

[16] J. Rovny, R. L. Blum, and S. E. Barrett, Phys. Rev. Lett. **120**, 180603 (2018).

[17] S. Pal, N. Nishad, T. S. Mahesh, and G. J. Sreejith, Phys. Rev. Lett. **120**, 180602 (2018).

[18] T. Tomita, S. Nakajima, I. Danshita, Y. Takasu, and Y. Takahashi, Science Advances **3**, e1701513 (2017).

[19] Y. Ashida, S. Furukawa, and M. Ueda, Phys. Rev. A **94**, 053615 (2016).

[20] Y. Ashida, S. Furukawa, and M. Ueda, Nature Communications **8**, 15791 EP (2017), article.

[21] Z. Gong, Y. Ashida, K. Kawabata, K. Takasan, S. Higashikawa, and M. Ueda, Phys. Rev. X **8**, 031079 (2018).

[22] K. Mizuta, K. Takasan, M. Nakagawa, and N. Kawakami, Phys. Rev. Lett. **121**, 093001 (2018).

[23] M. Mitrano, A. Cantaluppi, D. Nicoletti, S. Kaiser, A. Perucchi, S. Lupi, P. Di Pietro, D. Pontiroli, M. Riccò, S. R. Clark, D. Jaksch, and A. Cavalleri, Nature **530**, 461 EP (2016).

[24] J.-i. Okamoto, A. Cavalleri, and L. Mathey, Phys. Rev. Lett. **117**, 227001 (2016).

[25] M. A. Sentef, A. F. Kemper, A. Georges, and C. Kollath, Phys. Rev. B **93**, 144506 (2016).

[26] M. Knap, M. Babadi, G. Refael, I. Martin, and E. Demler, Phys. Rev. B **94**, 214504 (2016).

[27] D. M. Kennes, E. Y. Wilner, D. R. Reichman, and A. J. Millis, Nature Physics **13**, 479 EP (2017).

[28] M. A. Sentef, Phys. Rev. B **95**, 205111 (2017).

[29] Y. Murakami, N. Tsuji, M. Eckstein, and P. Werner, Phys. Rev. B **96**, 045125 (2017).

[30] G. Mazza and A. Georges, Phys. Rev. B **96**, 064515 (2017).

[31] M. Schütt, P. P. Orth, A. Levchenko, and R. M. Fernandes, Phys. Rev. B **97**, 035135 (2018).

[32] C. Zener, Proceedings of the Royal Society of London A: Mathematical, Physical and Engineering Sciences, **145**, 523 (1934).

[33] Y. Taguchi, T. Matsumoto, and Y. Tokura, Phys. Rev. B **62**, 7015 (2000).

[34] H. Yamakawa, T. Miyamoto, T. Morimoto, T. Terashige, H. Yada, N. Kida, M. Suda, H. . M. Yamamoto, R. Kato, K. Miyagawa, K. Kanoda, and H. Okamoto, Nature Materials **16**, 1100 EP (2017).

[35] T. Oka, R. Arita, and H. Aoki, Phys. Rev. Lett. **91**, 066406 (2003).

[36] T. Oka and H. Aoki, Phys. Rev. Lett. **95**, 137601 (2005).

[37] T. Oka and H. Aoki, Phys. Rev. B **81**, 033103 (2010).

[38] T. Oka, Phys. Rev. B **86**, 075148 (2012).

[39] S. Ajisaka, H. Nishimura, S. Tasaki, and I. Terasaki, Progress of Theoretical Physics **121**, 1289 (2009) .

[40] S. Nakamura, Progress of Theoretical Physics **124**, 1105 (2010) .

[41] J. Schwinger, Phys. Rev. **82**, 664 (1951).

[42] S. Katz, J. L. Lebowitz, and H. Spohn, Journal of Statistical Physics **34**, 497 (1984).

[43] T. Kitagawa, E. Berg, M. Rudner, and E. Demler, Phys. Rev. B **82**, 235114 (2010).

[44] T. Kitagawa, T. Oka, A. Brataas, L. Fu, and E. Demler, Phys. Rev. B **84**, 235108 (2011).

[45] N. H. Lindner, G. Refael, and V. Galitski, Nat. Phys. **7**, 490 (2011) .

[46] B. Dóra, J. Cayssol, F. Simon, and R. Moessner, Phys. Rev. Lett. **108**, 056602 (2012).

[47] P. Delplace, A. Gómez-León, and G. Platero, Phys. Rev. B **88**, 245422 (2013).

[48] M. Ezawa, Phys. Rev. Lett. **110**, 026603 (2013).

[49] M. S. Rudner, N. H. Lindner, E. Berg, and M. Levin, Phys. Rev. X **3**, 031005 (2013).

[50] P. Titum, E. Berg, M. S. Rudner, G. Refael, and N. H. Lindner, Phys. Rev. X **6**, 021013 (2016).

[51] F. D. M. Haldane, Phys. Rev. Lett. **61**, 2015 (1988).

[52] A. G. Grushin, A. Gómez-León, and T. Neupert, Phys. Rev. Lett. **112**, 156801 (2014).

[53] R. Wang, B. Wang, R. Shen, L. Sheng, and D. Y. Xing, EPL (Europhysics Letters) **105**, 17004 (2014).

[54] G. Jotzu, M. Messer, R. Desbuquois, M. Lebrat, T. Uehlinger, D. Greif, and T. Esslinger, Nature **515**, 237 (2014).

[55] N. Fläschner, D. Vogel, M. Tarnowski, B. S. Rem, D.-S. Lühmann, M. Heyl, J. C. Budich, L. Mathey, K. Sengstock, and C. Weitenberg, Nature Physics **14**, 265 (2018).

[56] A. Kirilyuk, A. V. Kimel, and T. Rasing, Rev. Mod. Phys. **82**, 2731 (2010).

[57] E. Beaurepaire, J.-C. Merle, A. Daunois, and J.-Y. Bigot, Phys. Rev. Lett. **76**, 4250 (1996).

[58] A. V. Kimel, A. Kirilyuk, P. A. Usachev, R. V. Pisarev, A. M. Balbashov, and T. Rasing, Nature **435**, 655 EP (2005).

[59] C. D. Stanciu, F. Hansteen, A. V. Kimel, A. Kirilyuk, A. Tsukamoto, A. Itoh, and T. Rasing, Phys. Rev. Lett. **99**, 047601 (2007).

[60] M. Sato, S. Takayoshi, and T. Oka, Phys. Rev. Lett. **117**, 147202 (2016).

[61] D. Bossini, V. I. Belotelov, A. K. Zvezdin, A. N. Kalish, and A. V. Kimel, ACS Photonics **3**, 1385 (2016).

[62] M. F. Ciappina, J. A. Pérez-Hernández, A. S. Landsman, W. A. Okell, S. Zherebtsov, B. Förg, J. Schötz, L. Seiffert, T. Fennel, T. Shaaran, T. Zimmermann, A. Chacón, R. Guichard, A. Zaïr, J. W. G. Tisch, J. P. Marangos, T. Witting, A. Braun, S. A. Maier, L. Roso, M. Krüger, P. Hommelhoff, M. F. Kling, F. Krausz, and M. Lewenstein, Reports on Progress in Physics **80**, 054401 (2017).

[63] T. Arikawa, S. Morimoto, and K. Tanaka, Opt. Express **25**, 13728 (2017).

[64] J. H. Mentink, K. Balzer, and M. Eckstein, Nature Communications **6**, 6708 EP (2015), article.

[65] M. Bukov, M. Kolodrubetz, and A. Polkovnikov, Phys. Rev. Lett. **116**, 125301 (2016).

[66] M. Claassen, H.-C. Jiang, B. Moritz, and T. P. Devereaux, Nature Communications **8**, 1192 (2017).

[67] S. Kitamura, T. Oka, and H. Aoki, Phys. Rev. B **96**, 014406 (2017).

[68] J. He, S.-P. Kou, Y. Liang, and S. Feng, Phys. Rev. B **83**, 205116 (2011).

[69] B. Bauer, L. Cincio, B. P. Keller, M. Dolfi, G. Vidal, S. Trebst, and A. W. W. Ludwig, Nature Communications **5**, 5137 EP (2014), article.

[70] C. Hickey, L. Cincio, Z. Papić, and A. Paramekanti, Phys. Rev. Lett. **116**, 137202 (2016).

[71] M. A. Cazalilla and J. B. Marston, Phys. Rev. Lett. **88**, 256403 (2002).

[72] H. G. Luo, T. Xiang, and X. Q. Wang, Phys. Rev. Lett. **91**, 049701 (2003).

[73] S. R. White and A. E. Feiguin, Phys. Rev. Lett. **93**, 076401 (2004).

[74] A. J. Daley, C. Kollath, U. Schollwöck, and G. Vidal, Journal of Statistical Mechanics: Theory and Experiment **2004**, P04005 (2004).

[75] H. Aoki, N. Tsuji, M. Eckstein, M. Kollar, T. Oka, and P. Werner, Rev. Mod. Phys. **86**, 779 (2014).

[76] P. Werner, A. Comanac, L. de' Medici, M. Troyer, and A. J. Millis, Phys. Rev. Lett. **97**, 076405 (2006).

[77] A. Georges, G. Kotliar, W. Krauth, and M. J. Rozenberg, Rev. Mod. Phys. **68**, 13 (1996).

[78] D. Bernard and B. Doyon, Journal of Statistical Mechanics: Theory and Experiment **2016**, 064005 (2016).

[79] M. Bukov, L. D'Alessio, and A. Polkovnikov, Advances in Physics **64**, 139 (2015).

[80] T. Oka and S. Kitamura, Annual Review of Condensed Matter Physics **10** (2019) .

[81] T. Mikami, S. Kitamura, K. Yasuda, N. Tsuji, T. Oka, and H. Aoki, Phys. Rev. B **93**, 144307 (2016).

[82] L. D'Alessio and M. Rigol, Phys. Rev. X **4**, 041048 (2014).

[83] T. Kuwahara, T. Mori, and K. Saito, Ann. Phys. **367**, 96 (2016).

[84] T. Mori, T. Kuwahara, and K. Saito, Phys. Rev. Lett. **116**, 120401 (2016).

[85] D. A. Abanin, W. De Roeck, and F. Huveneers, Phys. Rev. Lett. **115**, 256803 (2015).

[86] S. A. Weidinger and M. Knap, Scientific Reports **7**, 45382 EP (2017), article.

[87] D. A. Abanin, W. D. Roeck, and F. Huveneers, Annals of Physics **372**, 1 (2016).

[88] R. Moessner and S. L. Sondhi, Nature Physics **13**, 424 EP (2017).

[89] R. Nandkishore and D. A. Huse, Annual Review of Condensed Matter Physics **6**, 15 (2015).

[90] E. Altman and R. Vosk, Annual Review of Condensed Matter Physics **6**, 383 (2015).

[91] D. V. Else, B. Bauer, and C. Nayak, Phys. Rev. Lett. **117**, 090402 (2016).

[92] N. Y. Yao, A. C. Potter, I.-D. Potirniche, and A. Vishwanath, Phys. Rev. Lett. **118**, 030401 (2017).

[93] L. Savary and L. Balents, Reports on Progress in Physics **80**, 016502 (2017).

[94] Y. Zhou, K. Kanoda, and T.-K. Ng, Rev. Mod. Phys. **89**, 025003 (2017).

[95] F. D. M. Haldane, Phys. Rev. Lett. **50**, 1153 (1983).

[96] I. Affleck, *in Champs, Cordes et Phenomenes Critiques; Fields, Strings and Critical Phenomena edited by E. Brézin and J. Zinn-Justin* (Elsevier, Amsterdam, 1989).

[97] K. Takasan, A. Daido, N. Kawakami, and Y. Yanase, Phys. Rev. B **95**, 134508 (2017).

[98] X.-L. Qi and S.-C. Zhang, Rev. Mod. Phys. **83**, 1057 (2011).

[99] S. Nadj-Perge, I. K. Drozdov, J. Li, H. Chen, S. Jeon, J. Seo, A. H. MacDonald, B. A. Bernevig, and A. Yazdani, Science **346**, 602 (2014).

[100] V. Mourik, K. Zuo, S. M. Frolov, S. R. Plissard, E. P. a. M. Bakkers, and L. P. Kouwenhoven, Science **336**, 1003 (2012).

[101] S. Kashiwaya, H. Kashiwaya, H. Kambara, T. Furuta, H. Yaguchi, Y. Tanaka, and Y. Maeno, Phys. Rev. Lett. **107**, 077003 (2011).

[102] S. Sasaki, M. Kriener, K. Segawa, K. Yada, Y. Tanaka, M. Sato, and Y. Ando, Phys. Rev. Lett. **107**, 217001 (2011).

[103] K. Matano, M. Kriener, K. Segawa, Y. Ando, and G.-q. Zheng, Nat. Phys. **12**, 852 (2016).

[104] S. Yonezawa, K. Tajiri, S. Nakata, Y. Nagai, Z. Wang, K. Segawa, Y. Ando, and Y. Maeno, Nat. Phys. **13**, 123–126 (2017).

[105] S. NishiZaki, Y. Maeno, and Z. Mao, J. Phys. Soc. Jpn. **69**, 572 (2000).

[106] K. Ishida, H. Mukuda, Y. Kitaoka, Z. Q. Mao, Y. Mori, and Y. Maeno, Phys. Rev. Lett. **84**, 5387 (2000).

[107] N. Levy, T. Zhang, J. Ha, F. Sharifi, A. A. Talin, Y. Kuk, and J. A. Stroscio, Phys. Rev. Lett. **110**, 117001 (2013).

[108] A. Gómez-León and G. Platero, Phys. Rev. Lett. **110**, 200403 (2013).

[109] M. Benito, A. Gómez-León, V. M. Bastidas, T. Brandes, and G. Platero, Phys. Rev. B **90**, 205127 (2014).

[110] P. Titum, E. Berg, M. S. Rudner, G. Refael, and N. H. Lindner, Phys. Rev. X **6**, 021013 (2016).

[111] D. H. Dunlap and V. M. Kenkre, Phys. Rev. B **34**, 3625 (1986).

[112] Y. Yanase, T. Jujo, T. Nomura, H. Ikeda, T. Hotta, and K. Yamada, Phys. Rep. **387**, 1 (2003).

[113] Y. Tada, N. Kawakami, and S. Fujimoto, New J. Phys. **11** (2009).

[114] T. Yoshida and Y. Yanase, Phys. Rev. B **93**, 054504 (2016).

[115] A. Daido and Y. Yanase, Phys. Rev. B **94**, 054519 (2016).

[116] D. J. Thouless, M. Kohmoto, M. P. Nightingale, and M. den Nijs, Phys. Rev. Lett. **49**, 405 (1982).

[117] T. Fukui, Y. Hatsugai, and H. Suzuki, J. Phys. Soc. Jpn. **74**, 1674 (2005).

[118] M. Shimozawa, S. K. Goh, R. Endo, R. Kobayashi, T. Watashige, Y. Mizukami, H. Ikeda, H. Shishido, Y. Yanase, T. Terashima, T. Shibauchi, and Y. Matsuda, Phys. Rev. Lett. **112**, 156404 (2014).

[119] E. Bauer and M. Sigrist (eds.), *Non-Centrosymmetric Superconductors: Introduction and Overview*, Vol. 847 (Springer, Berlin, 2012).

[120] S. Fujimoto, J. Phys. Soc. Jpn. **76**, 051008 (2007).

[121] D. Poletti and C. Kollath, Phys. Rev. A **84**, 013615 (2011).

[122] T. Ishikawa, Y. Sagae, Y. Naitoh, Y. Kawakami, H. Itoh, K. Yamamoto, K. Yakushi, H. Kishida, T. Sasaki, S. Ishihara, Y. Tanaka, K. Yonemitsu, and S. Iwai, Nat. comm. **5**, 5528 (2014).

[123] M. Hashimoto, I. M. Vishik, R.-H. He, T. P. Devereaux, and Z.-X. Shen, Nat. Phys. **10**, 483 (2014).

[124] A. T. Bollinger, G. Dubuis, J. Yoon, D. Pavuna, J. Misewich, and I. Božović, Nature **472**, 458 (2011).

[125] X. Leng, J. Garcia-Barriocanal, S. Bose, Y. Lee, and A. M. Goldman, Phys. Rev. Lett. **107**, 027001 (2011).

[126] P. Coleman, *Introduction to Many-Body Physics* (Cambridge University Press, UK, 2015).

[127] M. Dzero, K. Sun, V. Galitski, and P. Coleman, Phys. Rev. Lett. **104**, 106408 (2010).

[128] M. Dzero, J. Xia, V. Galitski, and P. Coleman, Annu. Rev. Condens. Matter Phys. **7**, 249 (2016).

[129] K. Takasan, M. Nakagawa, and N. Kawakami, Physics Procedia **75**, 447 (2015).

[130] K. Takasan, M. Nakagawa, and N. Kawakami, Phys. Rev. B **96**, 115120 (2017).

[131] P. Coleman, Phys. Rev. B **29**, 3035 (1984).

[132] P. Coleman, Phys. Rev. B **35**, 5072 (1987).

[133] D. Newns and N. Read, Advances in Physics **36**, 799 (1987).

[134] A. J. Millis and P. A. Lee, Phys. Rev. B **35**, 3394 (1987).

[135] T. Takimoto, J. Phys. Soc. Jpn. **80**, 123710 (2011).

[136] M.-T. Tran, T. Takimoto, and K.-S. Kim, Phys. Rev. B **85**, 125128 (2012).

[137] J. E. Moore and L. Balents, Phys. Rev. B **75**, 121306 (2007).

[138] L. Fu, C. L. Kane, and E. J. Mele, Phys. Rev. Lett. **98**, 106803 (2007).

[139] L. Fu and C. L. Kane, Phys. Rev. B **76**, 045302 (2007).

[140] B. Yan and C. Felser, Annu. Rev. Condens. Matter Phys. **8**, 337 (2017).

[141] P. Hosur and X. Qi, Comptes Rendus Physique **14**, 857 (2013).

[142] X.-X. Zhang, T. T. Ong, and N. Nagaosa, Phys. Rev. B **94**, 235137 (2016).

[143] H. Hübener, M. A. Sentef, U. de Giovannini, A. F. Kemper, and A. Rubio, Nat. comm. **8**, 13940 (2017).

[144] L. Bucciantini, S. Roy, S. Kitamura, and T. Oka, Phys. Rev. B **96**, 041126 (2017).

[145] Y. Xu, C. Yue, H. Weng, and X. Dai, Phys. Rev. X **7**, 011027 (2017).

[146] P. S. Riseborough, Advances in Physics **49**, 257 (2000).

[147] K. Hagiwara, Y. Ohtsubo, M. Matsunami, S.-I. Ideta, K. Tanaka, H. Miyazaki, J. E. Rault, P. L. Fèvre, F. Bertran, A. Taleb-Ibrahimi, R. Yukawa, M. Kobayashi, K. Horiba, H. Kumigashira, K. Sumida, T. Okuda, F. Iga, and S.-I. Kimura, Nat. comm. **7**, 12690 (2016).

[148] T. Kimura, T. Goto, H. Shintani, K. Ishizaka, T. Arima, and Y. Tokura, Nature **426**, 55 EP (2003).

[149] H. Katsura, N. Nagaosa, and A. V. Balatsky, Phys. Rev. Lett. **95**, 057205 (2005).

[150] M. Mostovoy, Phys. Rev. Lett. **96**, 067601 (2006).

[151] A. Pimenov, A. A. Mukhin, V. Y. Ivanov, V. D. Travkin, A. M. Balbashov, and A. Loidl, Nature Physics **2**, 97 EP (2006).

[152] Y. Tokunaga, Y. Taguchi, T.-h. Arima, and Y. Tokura, Nature Physics **8**, 838 EP (2012), article.

[153] Y. Tokura, S. Seki, and N. Nagaosa, Reports on Progress in Physics **77**, 076501 (2014).

[154] T. Fukui and N. Kawakami, Phys. Rev. B **58**, 16051 (1998).

[155] M. Eckstein, T. Oka, and P. Werner, Phys. Rev. Lett. **105**, 146404 (2010).

[156] K. Ueno, H. Shimotani, H. Yuan, J. Ye, M. Kawasaki, and Y. Iwasa, Journal of the Physical Society of Japan **83**, 032001 (2014).

[157] S. Z. Bisri, S. Shimizu, M. Nakano, and Y. Iwasa, Advanced Materials **29**, 1607054 (2017).

[158] P.-J. Hsu, A. Kubetzka, A. Finco, N. Romming, K. von Bergmann, and R. Wiesendanger, Nature Nanotechnology **12**, 123 EP (2016).

[159] H. Hirori, A. Doi, F. Blanchard, and K. Tanaka, Applied Physics Letters **98**, 091106 (2011).

[160] D. Nicoletti and A. Cavalleri, Adv. Opt. Photon. **8**, 401 (2016).

[161] X. G. Wen, *Quantum Field Theory of Many-body Systems: From the Origin of Sound to an Origin of Light and Electrons* (Oxford University Press, New York, 2007).

[162] F. Haldane, Physics Letters A **93**, 464 (1983).

[163] H. Katsura, M. Sato, T. Furuta, and N. Nagaosa, Phys. Rev. Lett. **103**, 177402 (2009).

[164] M. Takahashi, Journal of Physics C: Solid State Physics **10**, 1289 (1977).

[165] A. H. MacDonald, S. M. Girvin, and D. Yoshioka, Phys. Rev. B **37**, 9753 (1988).

[166] R. Bastardis, N. Guihéry, and C. de Graaf, Phys. Rev. B **76**, 132412 (2007).

[167] M. Eckstein, J. H. Mentink, and P. Werner, arXiv : 1703.03269 (2017).

[168] F. Görg, M. Messer, K. Sandholzer, G. Jotzu, R. Desbuquois, and T. Esslinger, Nature **553**, 481 EP (2018).

[169] M. M. S. Barbeau, M. Eckstein, M. I. Katsnelson, and J. H. Mentink, arXiv : 1803.03796 (2018).

[170] J. Nitta, T. Akazaki, H. Takayanagi, and T. Enoki, Phys. Rev. Lett. **78**, 1335 (1997).

[171] A. D. Caviglia, M. Gabay, S. Gariglio, N. Reyren, C. Cancellieri, and J.-M. Triscone, Phys. Rev. Lett. **104**, 126803 (2010).

[172] A. Soumyanarayanan, N. Reyren, A. Fert, and C. Panagopoulos, Nature **539**, 509 EP (2016).

[173] I. Bloch, J. Dalibard, and W. Zwerger, Rev. Mod. Phys. **80**, 885 (2008).

[174] S. Sachdev, K. Sengupta, and S. M. Girvin, Phys. Rev. B **66**, 075128 (2002).

[175] J. Simon, W. S. Bakr, R. Ma, M. E. Tai, P. M. Preiss, and M. Greiner, Nature **472**, 307 EP (2011).

[176] S. Pielawa, T. Kitagawa, E. Berg, and S. Sachdev, Phys. Rev. B **83**, 205135 (2011).

[177] C. P. Rubbo, S. R. Manmana, B. M. Peden, M. J. Holland, and A. M. Rey, Phys. Rev. A **84**, 033638 (2011).

[178] A. V. Gorshkov, S. R. Manmana, G. Chen, J. Ye, E. Demler, M. D. Lukin, and A. M. Rey, Phys. Rev. Lett. **107**, 115301 (2011).

[179] J. Carrasquilla, S. R. Manmana, and M. Rigol, Phys. Rev. A **87**, 043606 (2013).

[180] M. Snoek, I. Titvinidze, C. Tőke, K. Byczuk, and W. Hofstetter, New Journal of Physics **10**, 093008 (2008).

[181] A. Mazurenko, C. S. Chiu, G. Ji, M. F. Parsons, M. Kanász-Nagy, R. Schmidt, F. Grusdt, E. Demler, D. Greif, and M. Greiner, Nature **545**, 462 EP (2017).

[182] T. Jolicoeur and J. C. Le Guillou, Phys. Rev. B **40**, 2727 (1989).

[183] H. Neuberger and T. Ziman, Phys. Rev. B **39**, 2608 (1989).

[184] B. Bernu, P. Lecheminant, C. Lhuillier, and L. Pierre, Phys. Rev. B **50**, 10048 (1994).

[185] Z. Weihong, R. H. McKenzie, and R. R. P. Singh, Phys. Rev. B **59**, 14367 (1999).

[186] S. Yunoki and S. Sorella, Phys. Rev. B **74**, 014408 (2006).

[187] M. Q. Weng, D. N. Sheng, Z. Y. Weng, and R. J. Bursill, Phys. Rev. B **74**, 012407 (2006).

[188] D. Heidarian, S. Sorella, and F. Becca, Phys. Rev. B **80**, 012404 (2009).

[189] K. Harada, Phys. Rev. B **86**, 184421 (2012).

[190] O. A. Starykh and L. Balents, Phys. Rev. Lett. **98**, 077205 (2007).

[191] A. J. Schultz, M. A. Beno, U. Geiser, H. Wang, A. M. Kini, J. M. Williams, and M.-H. Whangbo, Journal of Solid State Chemistry **94**, 352 (1991).

[192] K. Nakamura, Y. Yoshimoto, T. Kosugi, R. Arita, and M. Imada, Journal of the Physical Society of Japan **78**, 083710 (2009).

[193] Y. Shimizu, K. Miyagawa, K. Kanoda, M. Maesato, and G. Saito, Phys. Rev. Lett. **91**, 107001 (2003).

[194] I. Kézsmárki, Y. Shimizu, G. Mihály, Y. Tokura, K. Kanoda, and G. Saito, Phys. Rev. B **74**, 201101 (2006).

[195] O. A. Starykh and L. Balents, Phys. Rev. Lett. **93**, 127202 (2004).

[196] A. Bombardi, L. C. Chapon, I. Margiolaki, C. Mazzoli, S. Gonthier, F. Duc, and P. G. Radaelli, Phys. Rev. B **71**, 220406 (2005).

[197] R. Nath, A. A. Tsirlin, H. Rosner, and C. Geibel, Phys. Rev. B **78**, 064422 (2008).

[198] A. A. Tsirlin, A. A. Belik, R. V. Shpanchenko, E. V. Antipov, E. Takayama-Muromachi, and H. Rosner, Phys. Rev. B **77**, 092402 (2008).

[199] K. Oka, I. Yamada, M. Azuma, S. Takeshita, K. H. Satoh, A. Koda, R. Kadono, M. Takano, and Y. Shimakawa, Inorganic Chemistry **47**, 7355 (2008).

[200] H.-C. Jiang, H. Yao, and L. Balents, Phys. Rev. B **86**, 024424 (2012).

[201] A. Metavitsiadis, D. Sellmann, and S. Eggert, Phys. Rev. B **89**, 241104 (2014).

[202] O. Mustonen, S. Vasala, K. P. Schmidt, E. Sadrollahi, H. C. Walker, I. Terasaki, F. J. Litterst, E. Baggio-Saitovitch, and M. Karppinen, arXiv : 1804.08630 (2018).

[203] A. O. Gogolin, A. A. Nersesian, and A. M. Tsvelik, *Bosonization and strongly correlated systems* (Cambridge University Press, UK, 2004).

[204] T. Giamarchi, *Quantum Physics in One Dimension*, International Series of Monographs on Physics (Clarendon Press, UK, 2003).

[205] A. M. Tsvelik, *Quantum Field Theory in Condensed Matter Physics* (Cambridge University Press, UK, 2007).

[206] N. D. Mermin and H. Wagner, Phys. Rev. Lett. **17**, 1133 (1966).

[207] D. J. Scalapino, Y. Imry, and P. Pincus, Phys. Rev. B **11**, 2042 (1975).

[208] H. J. Schulz, Phys. Rev. Lett. **77**, 2790 (1996).

[209] M. Bocquet, F. H. L. Essler, A. M. Tsvelik, and A. O. Gogolin, Phys. Rev. B **64**, 094425 (2001).

[210] M. Sato and M. Oshikawa, Phys. Rev. B **69**, 054406 (2004).

[211] K. Okunishi and T. Suzuki, Phys. Rev. B **76**, 224411 (2007).

[212] M. Klanjšek, H. Mayaffre, C. Berthier, M. Horvatić, B. Chiari, O. Piovesana, P. Bouillot, C. Kollath, E. Orignac, R. Citro, and T. Giamarchi, Phys. Rev. Lett. **101**, 137207 (2008).

[213] M. Sato, T. Hikihara, and T. Momoi, Phys. Rev. Lett. **110**, 077206 (2013).

[214] M. Matsumoto, C. Yasuda, S. Todo, and H. Takayama, Phys. Rev. B **65**, 014407 (2001).

[215] C. Yasuda, S. Todo, K. Hukushima, F. Alet, M. Keller, M. Troyer, and H. Takayama, Phys. Rev. Lett. **94**, 217201 (2005).

[216] M. Sato and M. Oshikawa, Phys. Rev. B **75**, 014404 (2007).

[217] J. Schlappa, K. Wohlfeld, K. J. Zhou, M. Mourigal, M. W. Haverkort, V. N. Strocov, L. Hozoi, C. Monney, S. Nishimoto, S. Singh, A. Revcolevschi, J.-S. Caux, L. Patthey, H. M. Rønnow, J. van den Brink, and T. Schmitt, Nature **485**, 82 EP (2012).

[218] M. Kohno, O. A. Starykh, and L. Balents, Nature Physics **3**, 790 EP (2007), article.

[219] R. Coldea, D. A. Tennant, K. Habicht, P. Smeibidl, C. Wolters, and Z. Tylczynski, Phys. Rev. Lett. **88**, 137203 (2002).

[220] M. Mourigal, M. Enderle, A. Klöpperpieper, J.-S. Caux, A. Stunault, and H. M. Rønnow, Nature Physics **9**, 435 EP (2013).

[221] A. Epstein, S. Etemad, A. Garito, and A. Heeger, Solid State Communications **9**, 1803 (1971).

[222] J. P. Renard, M. Verdaguer, L. P. Regnault, W. A. C. Erkelens, J. Rossat-Mignod, and W. G. Stirling, EPL (Europhysics Letters) **3**, 945 (1987).

[223] K. Katsumata, H. Hori, T. Takeuchi, M. Date, A. Yamagishi, and J. P. Renard, Phys. Rev. Lett. **63**, 86 (1989).

[224] V. Gadet, M. Verdaguer, V. Briois, A. Gleizes, J. P. Renard, P. Beauvillain, C. Chappert, T. Goto, K. Le Dang, and P. Veillet, Phys. Rev. B **44**, 705 (1991).

[225] J. Darriet and L. Regnault, Solid State Communications **86**, 409 (1993).

[226] T. Sakaguchi, K. Kakurai, T. Yokoo, and J. Akimitsu, Journal of the Physical Society of Japan **65**, 3025 (1996).

[227] N. Tsuji, T. Oka, and H. Aoki, Phys. Rev. B **78**, 235124 (2008).

[228] T. Oka, N. Konno, R. Arita, and H. Aoki, Phys. Rev. Lett. **94**, 100602 (2005).

[229] F. Heidrich-Meisner, I. González, K. A. Al-Hassanieh, A. E. Feiguin, M. J. Rozenberg, and E. Dagotto, Phys. Rev. B **82**, 205110 (2010).

[230] M. Claassen, C. Jia, B. Moritz, and T. P. Devereaux, Nature Communications **7**, 13074 EP (2016).

[231] S. Lukyanov and A. Zamolodchikov, Nuclear Physics B **493**, 571 (1997).

[232] S. Lukyanov, Phys. Rev. B **59**, 11163 (1999).

[233] S. Lukyanov and V. Terras, Nuclear Physics B **654**, 323 (2003).

[234] T. Hikihara and A. Furusaki, Phys. Rev. B **58**, 583(R) (1998).

[235] T. Hikihara and A. Furusaki, Phys. Rev. B **69**, 064427 (2004).

[236] S. Takayoshi and M. Sato, Phys. Rev. B **82**, 214420 (2010).

Acknowledgement

First of all, I would like to express my sincerest gratitude to Prof. Norio Kawakami for his kind support, encouragement, and fruitful discussions during my graduate course. Whenever I visited his office, he was always willing to spend time for discussions. His insightful suggestions have always inspired me, and I have learned a lot of things from him, which are not limited to physics. I am proud that I have studied quantum many-body physics under his supervision and guidance in this five years.

I would also like to thank my collaborators related to this thesis, Prof. Youichi Yanase, Prof. Masahiro Sato, Dr. Masaya Nakagawa and Mr. Akito Daido. Thorough the collaboration, I have learned a lot from them and what I have learned would be an important basis of my future works. Especially, I would like to express my deep appreciation to Dr. Masaya Nakagawa. From when I entered the graduate school, he has spent a lot of time for discussions with me. My research subject is deeply inspired by discussions with him and I could not work on my research topic, *nonequilibrium phenomena in condensed matter physics*, without him. In addition, I have finished other collaboration works not included in this thesis and I would like to thank the collaborators, Prof. Masahito Ueda, Mr. Yuto Ashida, Mr. Sho Higashikawa, Mr. Zongping Gong, Mr. Kohei Kawabata and Mr. Kaoru Mizuta. They have brought me into the research subjects (e.g. Non-Hermitian quantum systems and time crystal) which was not familiar with before these collaborations. The discussions with them were quite stimulating for me.

Thanks to various financial supports, I have attended many workshops and visited several institutes in my Ph.D course. I have discussed with many researchers there and obtained stimulating and valuable comments. I would like to appreciate all the people who discussed with me. Especially, I would like to express my gratitude to Prof. Takashi Oka (Max Planck Institute for Physics of Complex Systems, Germany), Prof. Manfred Sigrist (ETH, Switzerland), and Prof. Joel Moore (University of California Berkeley, United States of America) for being a host of my visits. In particular, Takashi Oka is a pioneer of the research field, nonequilibrium phenomena in condensed matter physics, and most of my studies are based on his works. When I visited him, I felt his philosophy about research and was inspired by it very much. In addition, he gave very helpful comments at the early stage of my studies included in this thesis. I would like to deeply appreciate him.

The research field where I am working on is crucially supported by rapidly developing experimental techniques. I learned a lot of things about experiments from discussions with many experimentalists. I would like to express my gratitude to all the experimentalists discussed with me. Especially, I would appreciate Prof. Koichiro Tanaka, Prof. Shin-ichi Kimura, Prof. Hiroshi Watanabe and Prof. Shinichiro Iwai for fruitful discussions about optical measurements. The discussions about experimental setups in this thesis is based on what I learned from them.

I would like to express my gratitude to staff members in the Condensed Matter Theory (CMT) group, Prof. Ryusuke Ikeda, Prof. Robert Peters, and Prof. Masaki Tezuka for helpful advises and comments in various opportunities. Also, I would like to thank my current and

former colleagues in CMT group. I am especially grateful to Mr. Kyosuke Adachi, Mr. Yuichiro Dan, Mr. Koudai Iwahori, Mr. Shuntaro Sumita, Mr. Hikaru Watanabe, Mr. Yoshihiro Michishita, Mr. Kazuhiro Kimura, Mr. Riki Toshio, Mr. Kazuki Yamamoto, Dr. Rina Takashima, Dr. Hiroaki Sumiyoshi, Dr. Takuya Nomoto, Dr. Ken Shiozaki, and Dr. Atsuo Shitade for everyday discussions about physics and others. My daily life in the group has been comfortable and enjoyable thanks to the communications with them.

During the Ph.D couse, I also have been encouraged by my friends out of CMT group. I would like to appreciate Mr. Yukihisa Imamura, Mr. Satoshi Kusaba and Mr. Takafumi Tomita. They are my friends belonging to the same graduate school and I have spent much great time with exciting discussion about physics and others. I would also thank to my friends belonging to different institutes, Mr. Hiroyuki Fujita, Mr. Sho Higashikawa, Mr. Yusuke Sugita and Mr. Keita Hamamoto. When I met them at workshops or their institutes, we had enjoyable time.

I would like to acknowledge the financial support from Japan Society for the Promotion of Science (JSPS) KAKENHI (Grant No. 16J05078) and JSPS Research Fellowship for Young Scientists.

At last, I would like to express my deepest gratitude to my parents, Hiroyuki Takasan and Eiko Takasan, and my best partner, Yoshino Enomoto, for their continuous support and encouragement.